Ultrasonic Lamb-Wave Devices Actuated by a Piezoelectric PZT Thin Film

Dissertation submitted to the Faculty of Science of the University of Neuchâtel, in fulfillment of the requirements for the degree of "Docteur ès Sciences"

by

Philippe Luginbuhl

Dipl. Phys. University of Neuchâtel

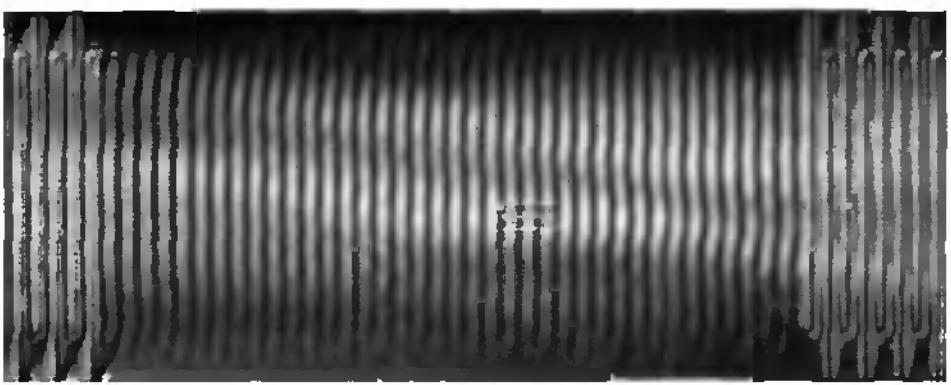

Institute of Microtechnology
University of Neuchâtel
Rue Jaquet-Droz 1, CH-2007 Neuchâtel
Switzerland

1998

IMPRIMATUR POUR LA THÈSE

Ultrasonic Lamb Wave Devices Actuated By a Piezoelectric PZT Thin Film

de M. Philippe Luginbuhl

UNIVERSITÉ DE NEUCHÂTEL

FACULTÉ DES SCIENCES

La Faculté des sciences de l'Université de Neuchâtel sur le rapport des membres du jury,

N. de Rooij (directeur de thèse), D. Twerenbold, S.D. Collins, (Uni. of California, Davis USA)

autorise l'impression de la présente thèse.

Neuchâtel, le 31 août 1998

Le doyen:

F. Stoeckli

To Christine

and our three children

David

Yoël

Na'ama

Contents

List of symbols and abbreviations

Chapter 3

A	area of the electrode. [m^2]
C	capacitance of the piezoelectric film. [F]
d_{31}	mechanical strain induced in the piezoelectric material in direction1 per unit electric field applied in direction 3. [C/N]
d_{31}^{sat}	mechanical strain induced in the piezoelectric material in direction1 corresponding to the saturation value of the electric field applied in direction 3. [C/N]
d_{33}	mechanical strain induced in the piezoelectric material in direction3 per unit electric field applied in direction 3. [C//N]
$\delta(L)$	vertical deflection at the tip of the cantilever beam. [m]
ε_0	permittivity of vacuum. [F/m]
ε_{33}^{T}	relative dielectric constant in direction 3 under the condition of constant stress.[F/m]
h_{si}	thickness of the silicon substrate. [m]
h_p	thickness of the PZT film. [m]
L	beam length. [m]
Q	quality factor. [ ]
S_{11}^{P}	compliance under mechanical stress of the PZT film. [m^2/N]
S_{11}^{si}	compliance under mechanical stress of the silicon substrate. [m^2/N]
V_{bias}	d.c. bias voltage. [V]
V_{ac}	a.c. voltage excitation. [V]
V_{osc}	a.c. voltage excitation. [V]
V_{PP}	peak to peak voltage excitation. [V]
X_i	displacement in the i direction. [m]

Chapter 4

a	antisymmetric mode or flexural motion.
a_0	lowest order antisymmetric mode (flexural)
a_i	antisymmetric i^{th} mode.
c	phase velocity. [m/s]
c_{11}	elastic stiffness constant. [N/m^2]
c_{22}	elastic stiffness constant. [N/m^2]
c_l	longitudinal-wave velocity in the bulk material. [m/s]
c_t	transverse-wave velocity in the bulk material. [m/s]

d	plate thickness. [m]
E	Young's modulus. [N/m^2]
ϕ	scalar potential
h	half-plate thickness. [m]
k	wave number [m^{-1}]
k_n	wave number of the nth mode. [m^{-1}]
k_t	transverse wave number. [m^{-1}]
L	longitudinal component.
λ	wavelength. [m]
λ_R	wavelength of the Rayleigh wave. [m]
n	integer number. [ ]
p	transducer periodicity. [m]
ρ	plate density. [kg/m^3]
s	symmetric mode or dilatational motion.
s_0	lowest order symmetric mode
s_i	symmetric ith mode
SH	shear horizontal surface mode.
T	residual in-plane tension. [N/m]
TV	transversal vertical component.
υ	Poisson ratio. [ ]
$\mathbf{u}$	resultant displacement vector of a material point in the lattice.
$\mathbf{u_L}$	longitudinal displacement vector of a material point in the lattice
$\mathbf{u_T}$	transversal displacement vector of a material point in the lattice
Vga_0	group velocity of the lowest order antisymmetric mode. [m/s]
$Vga_0(n)$	group velocity of the nth harmonic antisymmetric mode. [m/s]
Vgs_0	group velocity of the lowest order symmetric mode. [m/s]
$Vgs_0(n)$	group velocity of the nth harmonic symmetric mode. [m/s]
Vpa_0	phase velocity of the lowest order antisymmetric mode. [m/s]
$Vpa_0(n)$	phase velocity of the nth harmonic antisymmetric mode. [m/s]
Vps_0	phase velocity of the lowest order symmetric mode. [m/s]
$Vps_0(n)$	phase velocity of the nth harmonic symmetric mode. [m/s]
V_R	Rayleigh wave velocity. [m/s]
ω	angular frequency. [rad/s]
ω_n	angular frequency of the nth mode. [rad/s]
ψ	vector potential
X_i	displacement in the i direction. [m]

Chapter 5

a_0	lowest order antisymmetric mode (flexural)
d	distance between the midpoints of the two IDTs. [m]
E	vector of the electric field
E_i	electrical field component in the 1 direction. [V/m]

E_3	electrical field component in the 3 direction. [V/m]
f_1 or f_0	fundamental synchronous frequency of the IDT. [s^{-1}]
f_n	synchronous frequency of the n^{th} harmonic mode. [s^{-1}]
H(f)	overall transfer function
$H_i(f)$	individual frequency response of the i^{th} IDT.
$\varphi(f)$	phase shift. [rad]
K^2	Electromechanical coupling coefficient. [ ]
k_n	wave number of the n^{th} mode. [m^{-1}]
λ	wavelength. [m]
λ_n	wavelength of the n^{th} harmonic mode. [m]
n	integer number. [ ]
N	Number of comb fingers
N_p	number of finger pairs
p	transducer periodicity. [m]
s_0	lowest order symmetric mode (flexural)
V_p	phase velocity. [m/s]
V_{pn}	phase velocity of the n^{th} propagating mode. [m/s]
ΔV_p	change in phase velocity. [m/s]
ω_n	angular frequency of the n^{th} mode. [rad/s]
X_i	displacement in the i direction. [m]

Chapter 6

a	width of a comb finger. [m]
a_0	lowest order antisymmetric mode (flexural)
b	distance between the bulk Si and each finger end. [m]
d	center to center IDT separation. [m]
f_0	fundamental synchronous frequency of the IDT. [s^{-1}]
F	Fresnel parametert. [ ]
$\Delta\varphi$	phase change. [rad]
ΔL	length needed for the slope during the KOH step. [m]
δL	distance from the membrane edge to the middle of the IDT. [m]
λ	wavelength. [m]
N	Number of comb fingers
N_p	number of finger pairs
p	transducer periodicity. [m]
θ	IDT slanting angle. [deg]
V_g	group velocity. [m/s]]
V_p	phase velocity. [m/s]
w	finger overlap length. [m]

Chapter 7

$a_0(n)$	n^{th} harmonic of the lowest order antisymmetric mode
C	capacitance. [F]
d	film thickness. [m]
δ	phase difference between current and potential. [deg]
δ	evanescent decay length. [m]
E	Young's modulus. [N/m^2]
ε_0	permittivity in vacuum. [F/m]
ε_{PZT}	dielectric permittivity of PZT. [F/m]
ε_{pot}	potential electrostatic energy. [J]
ε_r	relative permittivity of PZT. [ ]
f_0	fundamental synchronous frequency of the IDT. [s^{-1}]
f_r	frequencies of periodic ripples. [Hz]
Δf	frequency shift. [Hz]
K^2	electromechanical coupling factor. [ ]
λ	wavelength. [m]
M	mass per unit area. [kg/m^2]
Δm_{fluid}	added mass per unit area. [g/cm^2]
Q	resonance quality factor. [ ]
S	plate area. [m^2]
$(S_m)_{fluid}$	gravimetric sensitivity. [cm^2/g]
$s_0(n)$	n^{th} harmonic of the lowest order symmetric mode
τ	acoustic delay time. [s]]
T	in-plane residual tension. [N/m]
υ	Poisson ratio. [ ]
V	potential. [V]
V_{bias}	d.c. bias voltage. [V]
Vga_0	group velocity of the lowest order antisymmetric mode. [m/s]
$Vga_0(n)$	group velocity of the n^{th} harmonic antisymmetric mode. [m/s]
Vgs_0	group velocity of the lowest order symmetric mode. [m/s]
$Vgs_0(n)$	group velocity of the n^{th} harmonic symmetric mode. [m/s]
V_p	Phase velocity. [m/s]
Vpa_0	phase velocity of the lowest order antisymmetric mode. [m/s]
$Vpa_0(n)$	phase velocity of the n^{th} harmonic antisymmetric mode. [m/s]
V_{pp}	peak to peak voltage excitation. [V]
Vps_0	phase velocity of the lowest order symmetric mode. [m/s]
$Vps_0(n)$	phase velocity of the n^{th} harmonic symmetric mode. [m/s]
ω	angular frequency. [rad/s]
X_c	capacitive reactance. [Ohm]

Abbreviations

ADRIE	Advanced Deep Reactive Ion Etching
AFM	Atomic Force Microscope
AlN	Aluminium Nitride
APM	Acoustic Plate Mode
BHF	Buffered Hydrofluoric Acid
CVD	Chemical Vapor Deposition
DI water	Deionized water
DIL	Dual In Line socket
DUT	Device Under Test
FE	Finite Element
FPW	Flexural-Plate Wave
HCl	Hydrochloric acid
IDT	InterDigital Transducer
IL	Insertion Loss
KOH	Potassium hydroxide
$LiNbO_3$	Lithium Niobate
$LiTaO_3$	Lithium Tantalate
LPCVD	Low Pressure Chemical Vapor Deposition
MEMS	Micro-Electro-Mechanical Systems
PCB	Printed Circuit Board
PECVD	Plasma Enhanced Chemical Vapor Deposition
PZT	Lead Zirconate Titanate $Pb(Zr_xTi_{1-x})O_3$
RIE	Reactive Ion Etching
r.f.	Radio Frequency
SAW	Surface Acoustic Wave
SEM	Scanning Electron Microscope
SH	Shear Horizontal
SiO_2	Silicon dioxide
Si_xN_y	Low stress silicon nitride
Si_3N_4	Silicon nitride
TTI	Triple Transit Interference
ZnO	Zinc oxide

1436

0. Abstract

The fabrication using silicon micromachining and characterization of cantilever beams as well as acoustic Lamb-wave sensors and actuators based on piezoelectric PZT sol-gel thin films are presented. The intended use of the Lamb-wave devices is for sensor and mass transport applications. The devices consist of dual interdigitated transducers patterned on a thin film composite membrane of silicon nitride, tantalum/platinum, and a sol-gel derived piezoelectric ceramic (PZT modified lead zirconate titanate $Pb(Zr_xTi_{1-x})O_3$) thin film. The theory and the acoustic properties of these devices are presented along with applications to sensors, mechanical transport and liquid delivery systems. Improved acoustic signals and improved mass transport are achieved with PZT over present Lamb wave devices utilizing ZnO or AlN as the piezoelectric transducer.

1. Introduction

In past years considerable attention has focused on the use of acoustic devices for chemical sensors [1.1], [1.2], [1.3], [1.4], [1.5]. Most of these acoustic sensors have employed surface acoustic waves (SAW) as their primary transduction mechanism. These sensors use acoustic waves usually composed of either Rayleigh or various other known plate modes [1.6], [1.7], propagating along the surface of thick elastic substrates. Chemical transduction is accomplished by "mass loading" or "viscoelastic damping" effects which alter the resonance frequency or phase of closed feedback oscillators. However, recently acoustic signals propagating on thin membranes, so called Lamb waves or Flexural-Plate-Waves (FPW), have also been explored as chemical sensors [1.8], [1.9], [1.10], [1.11], vehicles for mechanical transport [1.12], and fluid delivery systems [1.13], [1.14].

These Lamb wave devices possess several advantages over their "thick plate" SAW counterparts, including: (1) lower phase velocity for the lowest antisymmetric mode a_0 which can be made less than the sound velocity in liquids (typically 1500 m/s for water). For operation in liquids, the radiation loss of the a_0 mode can thus be minimized, (2) lower operational frequencies (typically 2-4 MHz in our case) for the lowest a_0 mode which simplifies amplification and detection electronics, (3) access to the back side of the membrane. For fluid loading, this simplifies the transducers isolation from conducting liquid, and (4) higher mechanical amplitudes than normal plate or Rayleigh surface acoustic waves which provides better mechanical coupling in mass transportation applications.

However, to date the only piezoelectric thin film materials which have been successfully employed in the fabrication of Lamb wave devices have been zinc oxide and aluminium nitride [1.15]. Although zinc oxide is a relatively good piezoelectric material, there are a number of other ceramics which possess higher piezoelectric coupling efficiencies, most notably PZT [1.16], [1.17], and significant improvements in Lamb wave performance are expected employing PZT [1.18], [1.19], [1.20], [1.21], [1.22], [1.23], as an acoustic transducer. Modified lead zirconate titanate (PZT, $Pb(Zr_x,Ti_{1-x})O_3$)-based ceramics are currently the leading materials for piezoelectric thin film applications.

Recently, a number of improved techniques for the deposition of thin films of PZT with superior piezoelectric properties have been reported [1.24], [1.25], [1.26], [1.27], [1.28], including sputtering, and sol-gel methods. Of these, sol-gel deposition shows considerable promise both from an application and commercial standpoint.

The principal objective of this Ph. D. Thesis is to demonstrate the fabrication, the characterization and the potential use of micromachined PZT based Lamb-wave devices for sensor and actuator applications, especially for mass transport and fluid delivery systems such as a FPW micropump. In order to study the behavoir of micro devices actuated by a piezoelectric PZT sol-gel thin film, it was necessary to include in these research the fabrication and the characterization of a variety of so-called test structures. Among these, cantilever beams are ideal canditates allowing many experimental investigations. The information obtained with these structures was very useful in the understanding of interdigital transducers having a piezoelectric layer subject to strong hysteresis.

In chapter 2, a short summary of the deposition process for PZT thin films is given. This brief resumé gives only the flow chart of the process involved for the deposition of PZT films, the processing of these films being done in the Ceramic Laboratory, at the Swiss Federal Institute of Technology, EPFL, in Lausanne.

Chapter 3 deals with the fabrication and the characterization of piezoelectric cantilever beams.

Chapter 4 presents an overview of the most important acoustic guided waves, as well as a few mathematical results that are necessary to understand the physical properties of such waves. These results allow a comparison of the measured data with the theory, and only analytical developments are considered (i.e. numerical solutions are not used). A new method for the calculation of the residual in-plane tension and the Young's modulus E of the composite thin plate is presented. This method is based on the ratio of harmonic mode frequencies.

In chapter 5, the transduction mechanism for the generation of acoustic waves is given.

Chapter 6 highlights the Lamb wave design and the fabrication technology using PZT thin films.

Finally, experimental results of micromachined Lamb-wave devices are presented in chapter 7.

1.1 References:

[1.1] J. W. Grate, S. J. Martin, and R. M. White, "Acoustic wave microsensors", *Anal. Chem.* **65**, 940A-58A (1993); **65**, 987A-96A (1993).

[1.2] H. Wohltjen and R. Dessy, "Surface acoustic wave probe for chemical analysis", *Anal. Chem.* **51**, 1458-75 (1979).

[1.3] J. Hlavay and G. G. Guilbault, "Applications of the piezoelectric crystal detector in analytical chemistry", *Anal. Chem.* **49**, 1890-8 (1977).

[1.4] F. G. Joshi, "Flow sensors based on surface acoustic waves", *Sensors and Actuators* **A 44**, 191-7 (1994).

[1.5] M. J. Vellekoop, "Microfabrication of acoustic-wave devices", *Proceedings of SPIE, Micromachined Devices and Components III*, 29 September 1997, Austin, Texas, USA, pp.90-9.

[1.6] S. J. Martin, A. J. Ricco, T. M. Niemczyk, and G. C. Frye, "Characterization of SH acoustic plate mode liquid sensors", *Sensors and Actuators* 20, 253-68 (1989).

[1.7] J. C. Andle, J. F. Vetelino, and R. Lec, "An acoustic plate mode immunosensor", Proc. IEEE Ultrasonics Symposium 1989, pp. 579-584.

[1.8] K. Uozumi, K. Ohsone, and R. M. White, "Generation and detection of ultrasonic Lamb waves in a thin deposited film by using interdigital transducers", *Appl. Phys. Lett.* **43** (10), 917-9 (1983).

[1.9] R. M. White, P. J. Wicher, S. W. Wenzel, and E. T. Zellers, "Plate-mode ultrasonic oscillator sensors", IEEE Transactions on Ultrasonics, Ferroelectrics, and Frequency Control, **34**, **2**, 162-71 (1987).

[1.10] A. W. Wang, B. J. Costello, and R. M. White, "An ultrasonic flexural-plate-wave sensor for measurement of diffusion in Gels", *Anal. Chem.* **65**, 1639-42 (1993).

[1.11] M. J. Vellekoop, G. W. Lubking, P. M. Sarro, and A. Venema, "Evaluation of liquid properties using a silicon Lamb wave sensor", *Sensors and Actuators* **A** 43, 175-80 (1994).

[1.12] R. M. Moroney, R. M. White, and R. T. Howe, "Ultrasonically induced microtransport", *Appl. Phys. Lett.* 59, 774-6 (1991).

[1.13] S. W. Wenzel, B. J. Costello, and R. M. White, "Flexural-Plate Waves for Sensors and Micropumps", *Sensors Magazine*, 47-49, December (1994).

[1.14] R. M. White, "Silicon-based ultrasonic microsensors and micropumps", *Integrated Ferroelectrics* 7, 353-58 (1995).

[1.15] A. Choujaa, N. Tirole, C. Bonjour, G. Martin, D. Hauden, P. Blind, A. Cachard, and C. Pommier, " AlN/silicon Lamb-wave microsensors for pressure and gravimetric measurements", *Sensors and Actuators* **A 46-47**, 179-82 (1995).

[1.16] Y. Xu, "Ferroelectric materials and their applications", *North-Holland* 1991, pp.101-159, chap.3.

[1.17] N. Setter, and E. L. Colla, "Ferroelectric ceramics, tutorial reviews, theory processing, and applications", *Birkhäuser Verlag Basel*, 1993, pp.1-87, chap.1.

[1.18] K. Sreenivas, and M. Sayer, "Characterization of $Pb(Zr,Ti)O_3$ thin films deposited from multi-element metal targets", *J. Appl. Phys.* **64 (3)**, 1484-93 (1988).

[1.19] K. Sameshima, T. Nakamura, K. Hoshiba, Y. Nakao, A. Kamisawa, T. Atsuki, N. Soyama, and K. Ogi, "Preparation of $Pb(Zr,Ti)O_3$ films on Pt/Ti/Ta electrodes by sol-gel process", *Jpn. J. Appl. Phys.* **32**, 4144-46 (1993).

[1.20] Ph. Luginbuhl, G.-A. Racine, Ph. Lerch, B. Romanowicz, K.G. Brooks, N. F. de Rooij, Ph. Renaud, and N. Setter, "Piezoelectric cantilever beams actuated by PZT sol-gel thin film", *Sensors and Actuators* **A 1-3**, 530-35 (1996).

[1.21] G.-A. Racine, R. Luthier, Ph. Luginbuhl, K. G. Brooks, N. Setter, and N. F. de Rooij, "Hybrid ultrasonic elastic force motor micromachined in silicon", *Integrated Ferroelectrics* **8**, 25-34 (1995).

[1.22] P. Muralt, M. Kohli, T. Maeder, A. Kholkin, K. Brooks, N. Setter, and R. Luthier, "Fabrication and characterizarion of PZT thin-film vibrators for micromotors", *Sensors and Actuators* **A 48**, 157-65 (1995).

[1.23] D. L. Polla, "Microelectromechanical Systems Based on Ferroelectric Thin Films", *Microelectronic Engineering* **29**, 51-58 (1995).

[1.24] K. G. Brooks, D. Damjanovic, N. Setter, Ph. Luginbuhl, G.-A. Racine, and N. F. de Rooij, "Piezoelectric response of PZT thin film actuated micromachined silicon cantilever beams", Proc. IEEE ISAF'94, pp. 520-22.

[1.25] K. G. Brooks, J. M. Reaney, T. Maeder, and N. Setter, "Processing sol-gel PZT films for microactuators", Proc. Electroceramics IV Conference on electronic ceramics and applications, Aachen, Germany, september 1994, pp.407-10.

[1.26] K. Brooks, D. Damjanovic, A. Kholkin, J. Reaney, N. Setter, Ph. Luginbuhl, G.-A. Racine, N. F. de Rooij, and A. Saaman, "PZT films for micro-pumps", *Integrated Ferroelectrics* **8**, 13-23 (1995).

[1.27] M. Sakata, S. Wakabayashi, H. Goto, H. Totani, M. Takeuchi, and T. Yada, "Sputtered high d31 coefficient PZT thin film for microactuators", Proc. IEEE Micro Electro Mechanical Systems, San Diego, California, february 1996, pp. 263-66.

[1.28] T. Maeder, P. Muralt, M. Kohli, A. Kholkin, and N. Setter, "$Pb(Zr,Ti)O_3$ Thin Films by *In-situ* Reactive Sputtering on Micromachined Membranes for Micromechanical Applications", Ceramic Films and Coatings, Sheffield (GB) 1994, British Ceramics Proceedings vol. 54, pp. 206-13 (1995).

1436

2. Ferroelectric PZT sol-gel thin film

2.1 Introduction

Over the past decade, the fabrication of ferroelectric PZT thin films has been investigated by many researchers. At present there exist a few thousand books and papers dealing with the properties, fabrication and applications of ferroelectric ceramics, first discovered by Wainer and Salomon in the United States (1942) [2.1], Wul and Goldman in Russia (1945) [2.2], and Ogawa in Japan (1947) [2.3].

During this work, research about PZT thin films, their properties, the method and techniques of deposition on tantalum/platinum electrode have been carried out in the Ceramic Laboratory, EPFL, Lausanne, Switzerland, under the direction of Professor Nava Setter [2.4]. The PZT thin films used for this work, were processed by K. G. Brooks [2.5], [2.6], [2.7].

In the following, only a brief outline of the deposition process is presented.

2.2 Sol-gel PZT thin film deposition

Ferroelectric layers exhibit a spontaneous polarization, in the absence of an external electric field. They can be defined as pyroelectric crystals whose polarization can be reversed by applying a strong electric field [2.8]. A hysteresis cycle is thus obtained by varying the electric field. Polycrystalline ferroelectric thin films, such as PZT films, consist of randomly oriented microdomains and their spontaneous polarization vanishes above a certain temperature, known as the Curie temperature.

The sol-gel method of deposition involved here is based on the spinning of a chemical solution on a platinum electrode, which as been previously evaporated on a silicon wafer. High quality, uniform PZT film of composition Pb $(Zr_{0.53}Ti_{0.47})O_3$ are achieved. However, localized microscopic cracks can be formed during the processing, which will then significantly lower the device performance. Figure 2.1 illustrates the main processing steps for the deposition of PZT thin films [2.4].

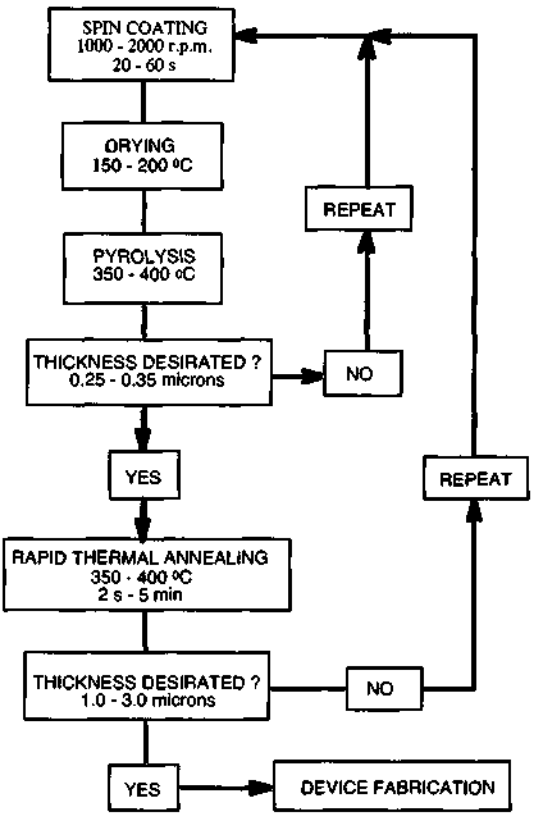

Figure 2.1: Flow chart of PZT processing.

Many research activities in this field highlight the huge potential of such thin films, e.g. the microstructure and processing of PZT [2.9], [2.10], [2.11], [2.12], rapid thermal processing [2.13], [2.14], characterization, fatigue, degradation mechanisms, losses and polarization decay [2.15], [2.16], [2.17], [2.18], [2.19], [2.20], etching [2.21], [2.22], [2.23], epitaxial growth [2.24], realization of micromotors [2.25], [2.26], [2.27], [2.28], and microelectromechanical systems and applications [2.29], [2.30], [2.31], [2.32].

2.3 References:

[2.1] E. Wainer, and A. N. Salomon, *Titanium Alloy Mfg. Co. Elect. Rep.* 8, 1942.

[2.2] B. M. Wul, and I. M. Goldmann, *C.R. Acad. Sci.* USSR 46, 1945, 139.

[2.3] T. Ogawa, Presented at the Meeting of the Research Institute of High-Dielectric-Constant Materials, cited in Busseiron Kenkyu N0. 6, 1947,1.

[2.4] N. Setter, and E. L. Colla, *Ferroelectric Ceramics, Tutorial reviews, theory, processing, and applications*, Birkhäuser Verlag, Basel, 1993.

[2.5] K. Brooks, D. Damjanovic, A. Kholkin, I. Reaney, N. Setter, P. Luginbuhl, G.-A. Racine, N. F. de Rooij, and A. Saaman, "PZT films for micro-pumps", *Integrated Ferroelectrics*, 1995, Vol. 8, pp. 13-23.

[2.6] K. Brooks, I. M. Reaney, T. Maeder, and N. Setter, "Processing sol-gel PZT films for microactuators", in *Proc. Electroceramics IV Conf. Electronic Ceramics and Applications*, Aachen, Germany, Sept. 1994, pp. 407-410.

[2.7] K. G. Brooks, R. D. Klissurska, P. Moeckli, and N. Setter, "Influence of Texture on the switching Behavior of $Pb(Zr_{0.70}Ti_{0.30})O_3$ Sol-Gel derived Thin Films", *J. Mat. Res.*, 12, N0. 2, Feb. 1997.

[2.8] N. W. Ashcroft, and N. D. Mermin, *Solid State Physics*, HRW International Editions, 1976, ch. 27.

[2.9] R. D. Klissurska, T. Maeder, K. G. Brooks, and N. Setter, "Microstructure of PZT sol-gel films on Pt substrates with different adhesion layers", *Microelectronic Engineering* 29, 1995, pp. 297-300.

[2.10] K. Brooks, R. Klissurska, P. Moeckli, and N. Setter, "Investigation of $Pb(Zr_{0.70}Ti_{0.30})D_3$ thin films of different textures on Ti/Pt electrodes", *Microelectronic Engineering* 29, 1995, pp. 293-296.

[2.11] T. G. Cooney, and L. F. Francis, "Processing of sol-gel derived PZT coatings on non-planar substrates", *J. Micromech. Microeng.* 6, 1996, pp. 291-300.

[2.12] S. P. Faure, J. Hector, P. Gaucher, and J. P Ganne, " Microstructure et propriétés électriques des couches minces de PZT par procédé sol-gel", *J. Phys. III France* 4, 1994, pp. 1929-1937.

[2.13] J. Chen, K. R. Udayakumar, K. G. Brooks, and L. E. Cross, "Rapid thermal annealing of sol-gel derived lead zirconate titanate thin films", *J. Appl. Phys*, 71 (9), 1 May 1992, pp. 4465-4469.

[2.14] Y. Huang, I. M. Reaney, and A. J. Bell, "Rapid thermal processing of PZT thin films", *Ferroelectrics*, 1992, Vol. 134, pp. 285-290.

[2.15] M. Toyama, R. Kubo, E. Takata, K. Tanaka, and K. Ohwada, "Characterization of piezoelectric properties of PZT thin films deposited on Si by ECR sputtering", *Sensors and Actuators* A 45, 1994, pp. 125-129.

[2.16] G. Teowee, C. D. Baertlein, E. A. Kneer, J. M. Boulton, and D. R. Uhlmann, "Effect of top metallization on the fatigue and retention properties of sol-gel PZT thin films", *Integrated Ferroelectrics*, 1995, Vol. 7, pp. 149-160.

[2.17] W. L. Warren, D. Dimos, and R. M. Waser, "Degradation Mechanisms in Ferroelectric and High-Permittivity Perovskites", *Material Research Society Bulletin*, July 1996, Vol. 21, N0 7, pp. 40-45.

[2.18] G. Arlt, "Ferroelectrics - Domains and Losses", *British Ceramics Proceedings Electroceramics*, N0 41, Feb. 1989, pp. 109-117.

[2.19] J. M. Benedetto, R. A. Moore, and F. B. McLean, "Effect of operating conditions on the fast decay component of the retained polarization in lead zirconate titanate thin films", *J. Appl. Phys.* 75, (1), 1 January 1994, pp. 460-466.

[2.20] H. Cao, and A. G. Evans, "Electric-Field-Induced Fatigue Crack Growth in Piezoelectrics", *J. Am. Ceram. Soc.* 77, (7), 1994, pp. 1783-1786.

[2.21] D. P. Vijay, S. B. Desu, and W. Pan, "Reactive Ion Etching of Lead Zirconate Titanate (PZT) Thin Film Capacitors", *J. Electrochem. Soc.*, Vol. 140, N0. 9, September 1993, pp. 2635-2639.

[2.22] S. Mancha, "Chemical Etching of Thin Film PLZT", *Ferroelctrics*, 1992, Vol. 135, pp.131-137.

[2.23] A. S. Nickles, R. Ramesh, R. M. White, and E. E. Haller, "Laser ablation-deposited PZT thin films for piezoelectric microsensors and microactuators", *Integrated Ferroelcetrics*, 1995, Vol. 10, pp. 89-98.

[2.24] J. M. Triscone, L. Fauchiger, M. Decroux, L. Miéville, O. Fischer, C. Beeli, P. Stadelmann, and G.-A. Racine, "Growth and structural properties of epitaxial $Pb(Zr_xTi_{1-x})O_3$ films and $Pb(Zr_xTi_{1-x})O_3$-cuprates heterostructures", *J. Appl. Phys.* 79 (8), 15 April 1996, pp. 4298-4305.

[2.25] K. R. Udayakumar, J. Chen, K. G. Brooks, L. E. Cross, A. M. Flynn, and D. J. Ehrlich, "Piezoelectric thin film ultrasonic micromotors", *Mat. Res. Soc. Symp. Proc.* Vol. 243, 1992.

[2.26] G.-A. Racine, R. Luthier, Ph. Luginbuhl, K. G. Brooks, N. Setter, and N. F. de Rooij, "Hybrid ultrasonic elastic force motor micromachined in silicon", *Integrated Ferroelectrics*, Vol. 8, 1995, pp. 25-34.

[2.27] P. Muralt, A. Kholkin, M. Kohli, T. Maeder, K. G. Brooks, R. Luthier, and N. Setter, "Fabrication and characterization of PZT thin films for micromotors", Transducers'95, Eurosensors IX, Stockholm, Sweden, June 25-29, 1995, pp.397-400.

[2.28] P. Muralt, M. Kohli, T. Maeder, A. Kholkin, K. Brooks, N. Setter, and R. Luthier, "Fabrication and characterization of PZT thin-film vibrators for micromotors", *Sensors and Actuators* A 48, 1995, pp. 157-165.

[2.29] D. L. Polla, "Microelectromechanical Systems Based on Ferroelectric Thin Films", *Microelectronic Engineering* 29, 1995, pp. 51-58.

[2.30] T. Maeder, P. Muralt, M. Kohli, A. Kholkin, and N. Setter, "$Pb(Zr,Ti)O_3$ Thin Films by *In-Situ* Reactive Sputtering on Micromachined Membranes for Micromechanical Applications", *British Ceramics Proceedings*, Vol. 54, 1994, pp. 206-213.

[2.31] D. L. Polla, and L. F. Francis, "Ferroelectric Thin Films in Microelectromechanical Systems Applications", *Material Research society Bulletin*, Vol. 21, (7) July 1996, pp. 59-65.

[2.32] T. Fujii, and S. Watanabe, "Feedback positioning cantilevers using lead zirconate titanate thin film for force microscopy observation of micropattern", *Appl. Phys. Lett.* 68 (4), 22 January 1996, pp. 467-468.

3. Piezoelectric cantilever beams

3.1 Introduction

Micromachined silicon cantilever beams actuated by the inverse piezoelectric effect are of great interest for actuator applications [3.1], [3.2], [3.3], [3.4], [3.5], [3.6], and for the characterization of piezoelectric thin films [3.7], [3.8], [3.9], [3.10], [3.11], [3.12], [3.13], [3.14]. This chapter deals with the microfabrication and the characterization of cantilever beams based on PZT thin films. Small multilayered beams are processed and used to analyse the inverse piezoelectric effect and to measure their mechanical deflection. The mechanical response of piezoelectrically operated heterogeneous bimorph structures is then compared with finite element simulations. Determination of the piezoelectric coefficient d_{31} using interferometric displacement measurements, electrical impedance measurements, and finite element calculation will be discussed.

3.2 Microfabrication

Each cantilever beam consists of a lead zirconium titanate (PZT) film (0.44 μm thick) sandwiched between two platinum electrodes on a silicon nitride/silicon substrate (0.7/14.3 μm thick) with a 0.9 μm SiO_2 passivation layer. Figure 3.1 illustrates the main processing steps.

(1) A 0.7 μm thick low stress silicon nitride Si_xN_y layer is deposited on both sides of a 3 inch diameter, 380 μm thick silicon wafer. Next, a Ta/Pt (0.01/0.07 μm thick) metallization is deposited. The PZT layer (0.44 μm thick)

is then deposited by spin coating over the former ground electrode, and etched in a solution of BHF&HCl&Deionized water [3.15].

Three different concentrations of BHF, HCl and DI water have been tested in order to minimize both the PZT under etch and the etching time. The results are summarized in Table 3.1, for a 0.3 μm thick PZT film.

Wafer N°	**BHF:HCl:DI concentration**	**Etching time**	**Under etch**
1	1:2:3	19 s	1.5 μm
2	1:2:9	34 s	1.0 μm
3	1:2:10	58 s	2.0 μm

Table 3.1: Parameters of three PZT chemical etch tests for a 0.3 μm thick PZT film.

The best results are obtained with the 1:2:9 concentration. During this chemical etch, a photoresist layer (PR+ 1400-27) of 1.5 μm thickness protects the PZT test structures. In each case some small areas with residual Pb-rich film are observed and can easily be removed by rinsing the wafer for a few minutes in flowing deionized water. Electrical contact on platinum is possible after the PZT structuration. Then, the silicon nitride layer on the wafer backside is patterned (plasma etching) to create the KOH apertures.

(2) Patterning of the top Ta/Pt electrode level by a standard lift-off technique.

(3) Deposition and patterning of a 0.45 μm thick CVD SiO_2 passivation layer. This layer is necessary to protect the PZT film during the platinum structuring.

(4) Ta/Pt dry etch and second level passivation. The necessity to etch the platinum bottom electrode after having etched the PZT film, requires a further passivation to insulate the two electrode levels, in order to avoid a short circuit.

(5) Opening of the contact areas through the passivation, and metallization of contact lines.

(6) Wet etching of the silicon backside in KOH. The PZT areas on the top side are protected by inserting the wafer in a mechanical chuck (c.f. chapter 6 for more details). Definition of the cantilever shape by a photolithography step.

(7) Structuring of the cantilever beams by plasma etching.

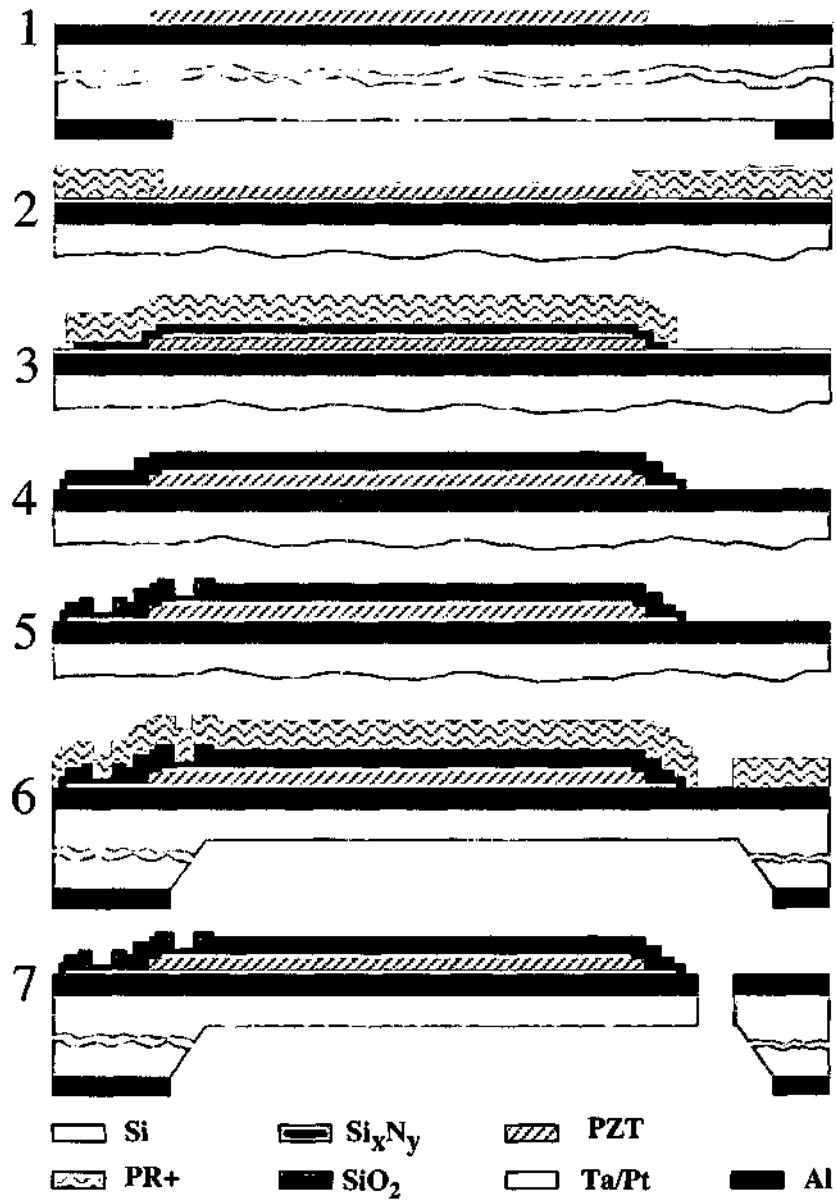

Figure 3.1: Fabrication sequence of the piezoelectric cantilever beams. See text for details.

The superposition of the different layers used for the fabrication of cantilever beams is presented in Figure 3.2.

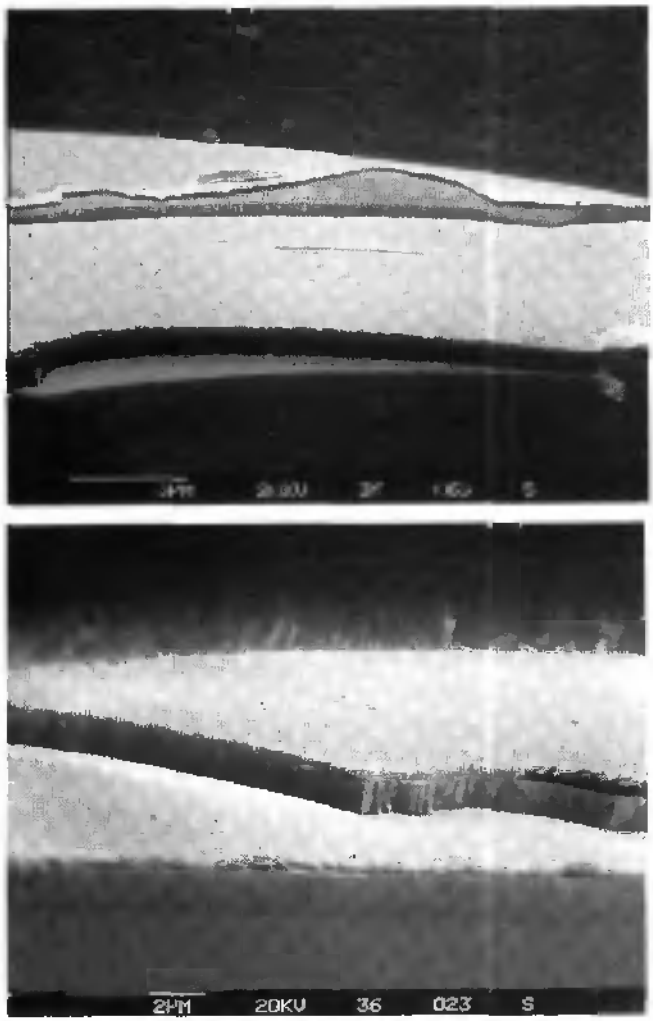

Figure 3.2: SEM pictures of the six superposed layers. (Top) From top to bottom respectively: SiO_2 passivation, Pt top electrode, PZT film, Pt bottom electrode, low stress silicon nitride, silicon. (Bottom) Enlarged view.

As shown in Figures 3.3-6, different types of rectangular and triangular cantilevers with various aspect ratios were fabricated. The maximal beam length is 1mm. For rectangular beams, the width is 100 μm or 200 μm.

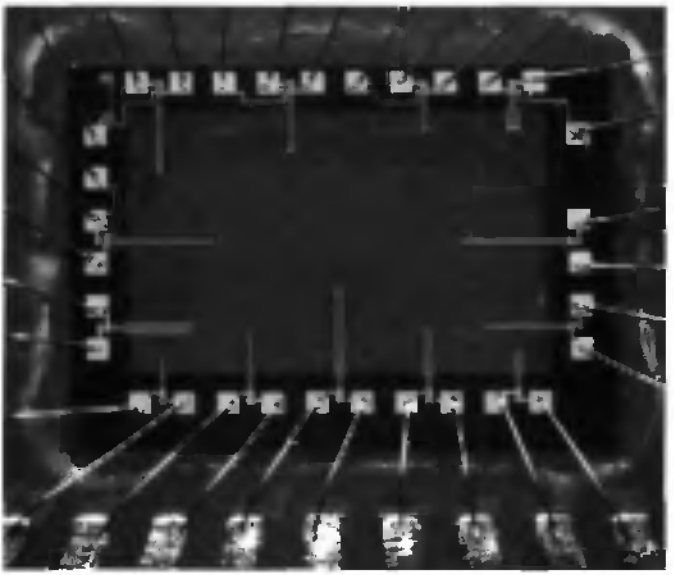

Figure 3.3: Optical view of micromachined piezoelectric bimorph cantilevers.

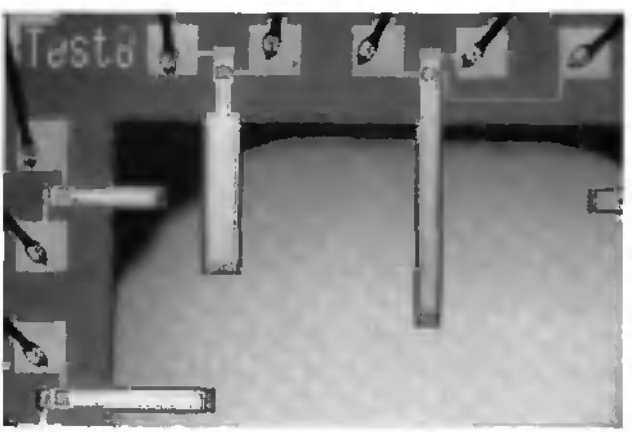

Figure 3.4: Detail of the piezoelectric cantilever beams.

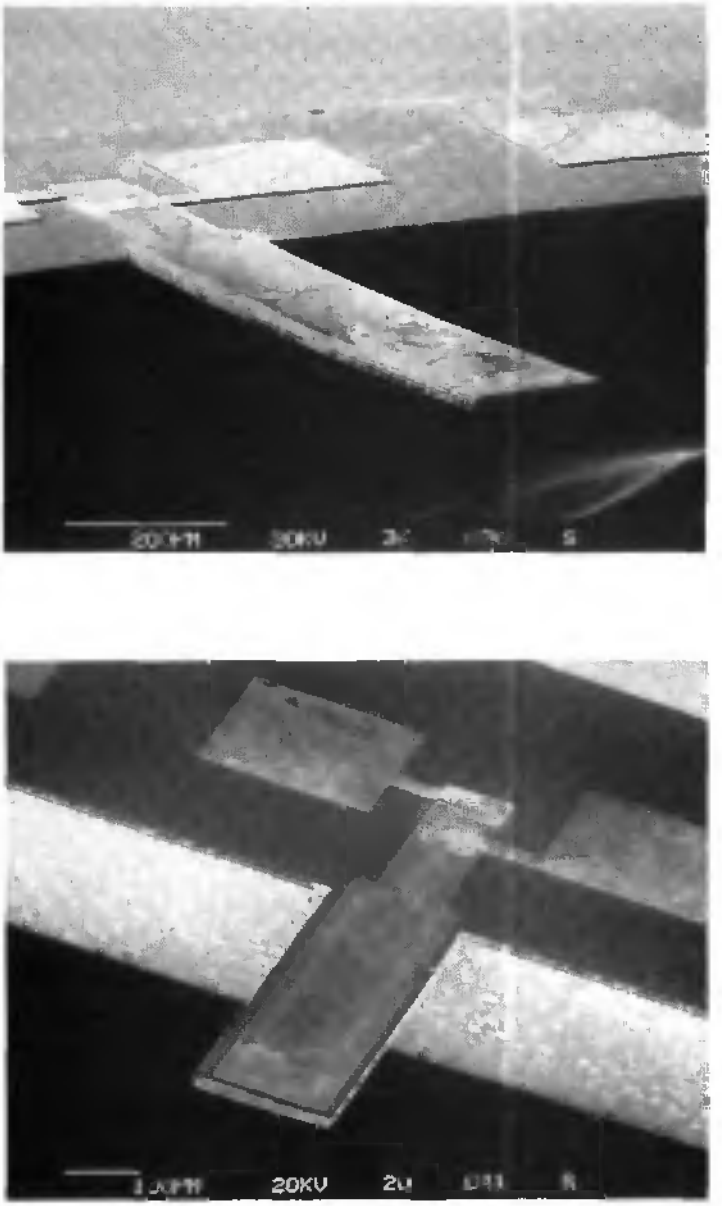

Figure 3.5: SEM pictures of cantilever beams.

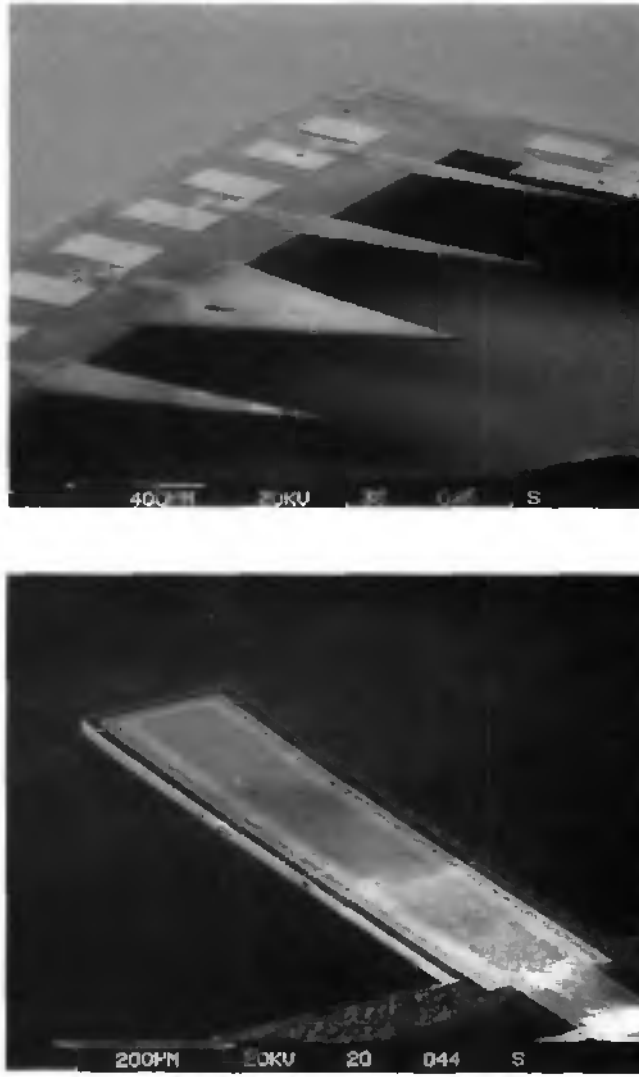

Figure 3.6: SEM view of micromachined beams.

In Figure 3.7, both sides of entire processed silicon wafers are presented. It is to be noted, that the former process was also used for the fabrication of Lamb-wave devices, referred to in the following chapters as Lamb-wave

devices of the first generation. In the picture, the largest rectangular areas correspond to these Lamb-wave devices.

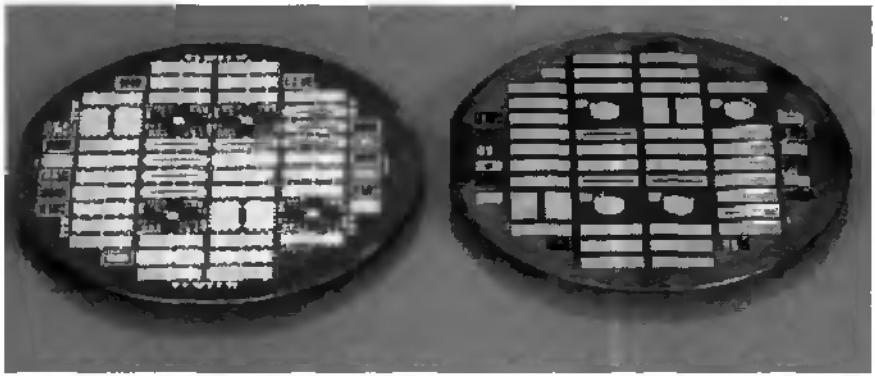

Figure 3.7: Optical view of processed wafers. Left picture: wafer top side; the cantilevers are not yet structured. Right picture: wafer backside; each cantilever is completely processed and the membrane areas for the Lamb-wave devices are etched.

3.3 Experimental results

3.3.1 Measurement techniques

A commercial Mach-Zehnder interferometer combined with a phase-sensitive amplifier, enables to measure very small vertical displacements of the cantilevers (resolution below 10^{-10} m). Measurements are done coherently with the voltage excitation applied to the bottom and top platinum electrodes.

If the spot of the laser-beam is positioned at a fixed point on the cantilever, a so called mechanical response spectrum of the beam is obtained, by simply varying the excitation frequency. If, on the other hand, the

excitation frequency is fixed, the spot of the laser-beam can be monitored along the cantilever in the x and y directions, allowing thus to obtain a two or three dimensional mode profile. In the following, quasistatic and dynamic behaviors are reported. For the electrical response, an HP impedance/gain-phase network analyzer is used.

Figure 3.8 illustrates the cantilever vibration due to the applied voltage. Schematically, when a voltage is applied to the platinum electrodes, the PZT film elongates (or contracts) while the other underlying layers contract (or elongate), resulting in a bending of the beam. It has been reported, that the deflection curve of the beam is affected by both the piezoelectric charge constants d_{31} and d_{33} [3.12], where d_{3i} (i=*1* or *3*) is the mechanical strain induced in the PZT material in direction i per unit electric field applied in direction *3*. (c.f. Figure 3.8). In this study, the d_{33} contribution is neglected.

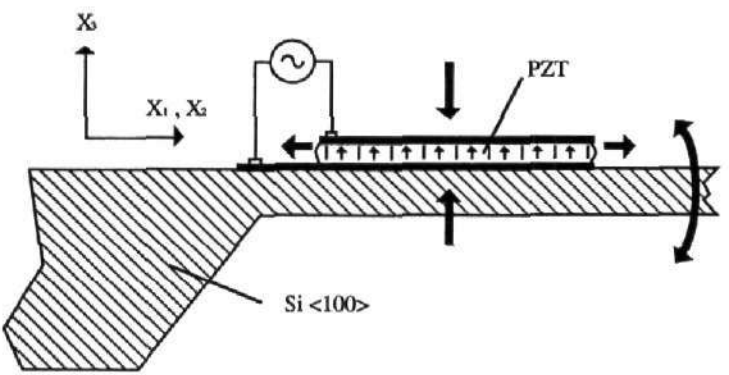

Figure 3.8: The mechanical strain induced in the PZT film in direction X_1 induces a flexural out-of-plane vibration of the silicon/PZT bimorph.

3.3.2 Quasistatic measurements

The measurements have been performed for beams with a length of 800 μm and 1000 μm and a width of 200 μm. At a fixed frequency of 537 Hz and with a 50 mV a.c. excitation, the quasi-static deflection along the length of the beam for different bias voltages V_{bias} was measured (see Figure. 3.9).

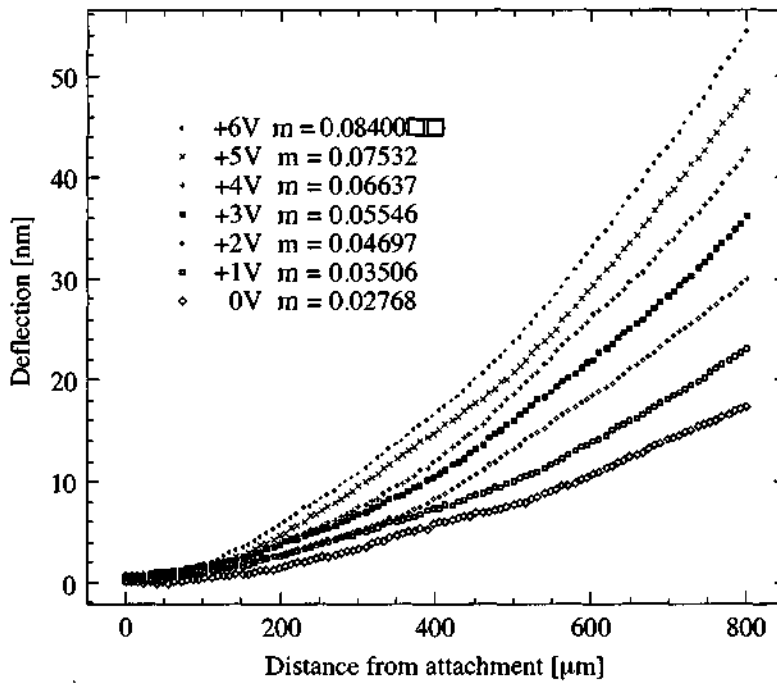

Figure 3.9: Quasi-static deflection of a beam along its length under various applied voltages V_{bias}. The slope values m correspond to the linear fits as a function of the squared distance (not on the picture).

For the piezoelectric heterogeneous bimorph of the form considered here, the vertical deflection $\delta(L)$ at the tip of the beam (see Figure 3.10) can be expressed as a function of the applied bias voltage V_{bias} according to [3.16]:

$$\delta(L) = \frac{-3d_{31}s_{11}^{si}s_{11}^{p}h_{si}(h_{si}+h_p)L^2}{K} V \qquad (3.1)$$

where s_{11}^{si} and s_{11}^{p} are the compliance under mechanical stress of the substrate and the PZT film respectively, L the beam length, h_{Si} being the thickness of the substrate, h_p that of the PZT film, and

$$K = 4S_{11}^{p}S_{11}^{si}h_{si}(h_p)^3 + 4S_{11}^{p}S_{11}^{si}(h_{si})^3h_p + (S_{11}^{p})^2(h_{si})^4 + (S_{11}^{si})^2(h_p)^4 + 6S_{11}^{p}S_{11}^{si}(h_{si})^2(h_p)^2 \qquad (3.2)$$

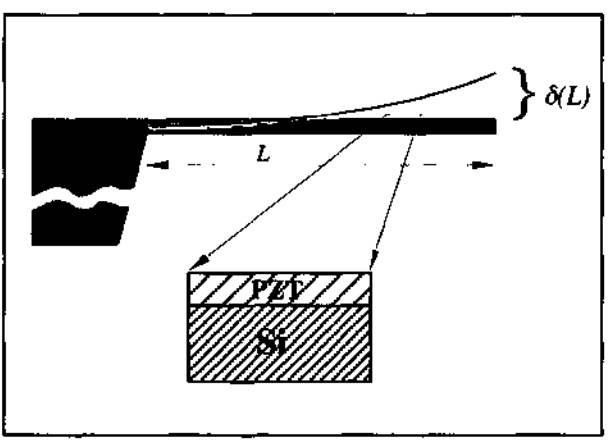

Figure 3.10: Schematic representation of a heterogeneous bimorph structure.

Measurement data according to equations (3.1) and (3.2) show a good linear behaviour when plotted as a function of the squared distance L^2. The deflection of the free end of the beam as a function of the applied bias voltage is shown in Figure 3.11. In the linear domain (up to 6 V), the deflection amplitude for a normalized a.c excitation was calculated. From the slope of the linear fit, a transverse piezoelectric coefficient d_{31} = -24.72 $\cdot 10^{-12}$ C/N was obtained corresponding to the linear piezoelectric behavior of the PZT thin film. In this calculation the following elastic constants were used: Si substrate s_{11}^{Si} = 0.77 $\cdot 10^{-11}$ m^2/N, PZT film, s_{11}^{p} = 13.8 $\cdot$ 10^{-12} m^2/N (value for bulk ceramic PZT of morphotropic boundary composition).

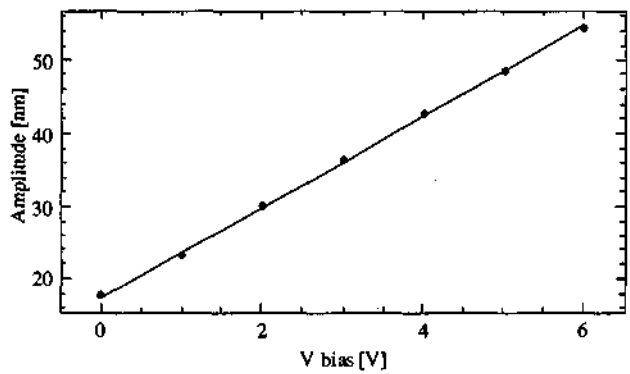

Figure 3.11: Quasi-static deflection at the free end of the beam (800 μm length) under various applied voltages V_{bias}.

From Figure 3.11, the deflection at V_{bias} = 0 V is observed to be equivalent to a bias of 2.8 V. This shift is believed to result from initial bending of the beam due to residual stress and/or from some partial poling of the PZT layer which occurs during the final plasma etching of the structures.

At higher applied voltages, the mechanical hysteresis loops of the beam as a function of d.c. bias for different a.c. excitations (500 Hz) show the same behavior (see Figure 3.12). The data are asymmetric and centred about a negative bias of 2.8 V. Calculation of the piezoelectric coefficient d_{31}^{sat} corresponding to the 12 V (saturation value) of the applied bias voltage, yields a value of d_{31}^{sat} = -32.4 $\cdot 10^{-12}$ C/N which is about 35% of the bulk ceramic value of -93 $\cdot 10^{-12}$ C/N [3.17].

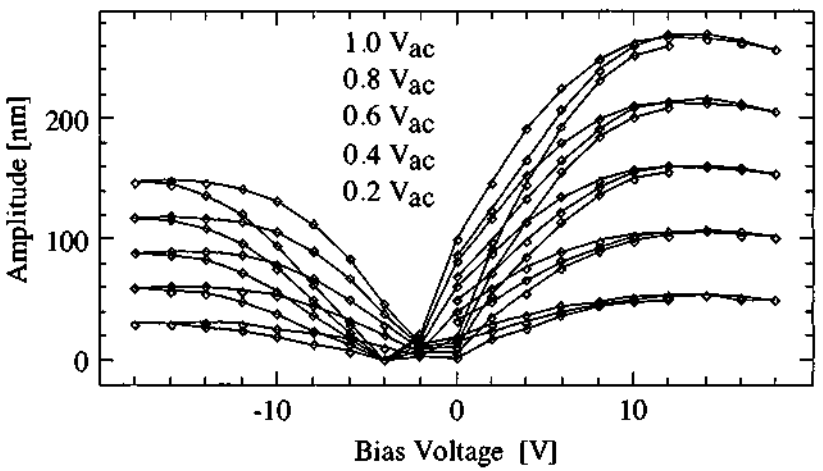

Figure 3.12: Mechanical hysteresis loops of a beam at quasistatic frequency (f = 500 Hz) under various a.c. excitations.

3.3.3 Dynamic measurements

The amplitude vibration of a cantilever beam is an important tool to study the behavior of a PZT film, pertaining to the ability of the piezo-film to react under the application of various bias voltages. Figure 3.13 points out these results. Frequency sweeps near the fundamental resonance of a 1 mm length beam, emphasizes the amplitude increase as a function of the bias voltage. The

small decrease of the resonance frequency due to the increase of the bias is probably related to thermal heating of the film. Nevertheless, this frequency shift is much smaller than that of a Lamb-wave sensor (c.f. chapter 7, section 7.4.3).

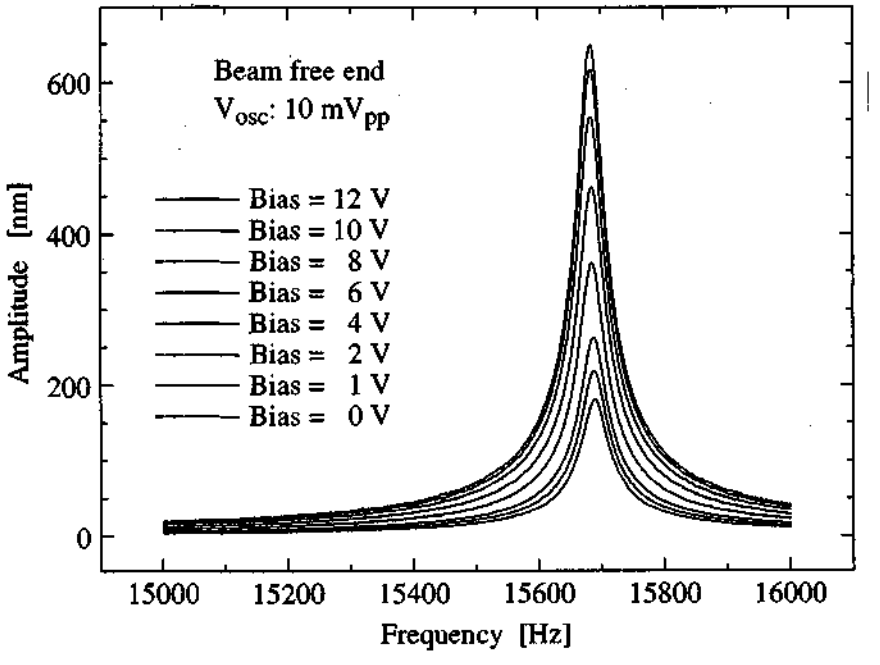

Figure 3.13: Mechanical response of a beam under different bias voltages..

Mode profiles of a beam are obtained by moving the laser beam along the cantilever for the resonance frequency and its harmonics. Figure 3.14 illustrates four mode profiles of a an 800 μm beam.

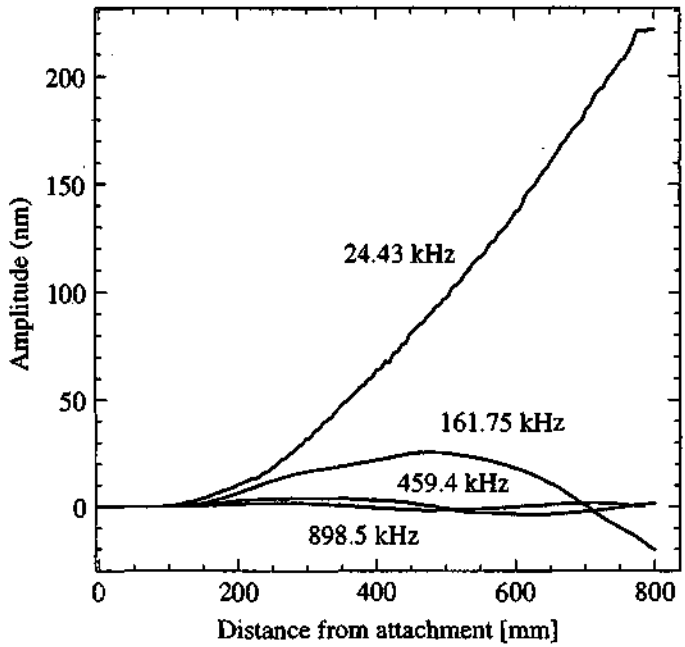

Figure 3.14: Some mode profiles of a piezoelectric cantilever beam.

3.3.4 Electrical measurements

The capacitance of the piezoelectric film with the constraints due to the rigid bond to the beam is expressed, according to [3.16]:

$$C = \frac{A}{h_P}\left(\varepsilon_{33}^{T} - \frac{d_{31}^{2} h_{si}\left[s_{11}^{si}(h_p)^3 + s_{11}^{p}(h_{si})^3\right]}{K}\right) \qquad (3.3)$$

where A is the area of the entire electrode of the considered beam, and ε_{33}^{T} the relative dielectric constant under condition of constant stress ($\varepsilon_{33}^{T} = 640\,\varepsilon_0$ was

obtained, ε_0 being the permittivity of vacuum. See chapter 7. section 7.2.1 for the description of the measurement).

From impedance measurement, a capacitance $C=1.1744 \cdot 10^{-9}$ F was determined. According to the relation (3.3) and a poling voltage of 2.8 V induced by the initial stress of the beam, a value of $-22.34 \cdot 10^{-12}$ C/N for d_{31} was obtained, which compares well with the value of $-24.72 \cdot 10^{-12}$ C/N obtained from the interferometric measurements.

3.3.5 Finite-element simulations

Finite element (FE) calculations (ANSYS) for the piezoelectric beam are presented here. The model consists of anisotropic solid elements for the Si substrate, isotropic solid elements for the nitride and SiO_2 layers, coupled-field solid elements for the PZT layer, and shell (membrane) elements for the electrodes layers.

Experimentally, an initial bending of the beam, which represents a displacement of about 16 μm (beam length of 1000 μm) was observed. This initial distortion is due to stress induced during the fabrication process. In our calculations, we reproduced the induced stress with a thermal effect by introducing different expansion coefficients for the layers. A small temperature shift has been imposed so as to have an initial stress producing the observed deflection. The FE coupled field results show that this initial stress also induces a potential difference of 5.6 V between the electrodes. However these free charges disappear in the capacitor's discharge time. Figure 3.15 shows the deflection profile of the beam owing to the process induced stress.

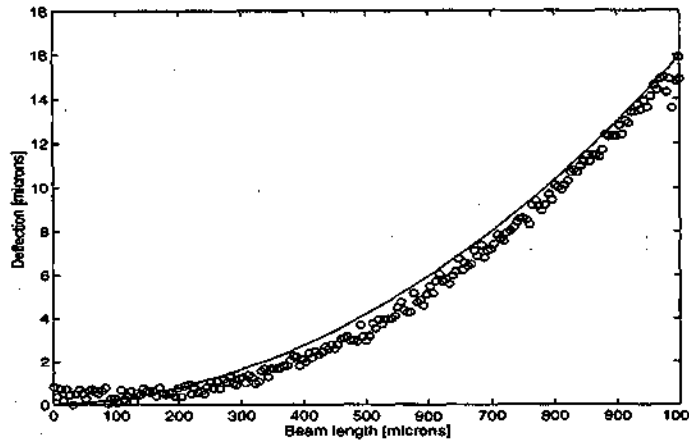

Figure 3.15: Experimental beam deflections (circles) determined by a confocal microscope, and FE calculations (line) due to stress.

The piezo coupling was also investigated by performing a static analysis in which a voltage is imposed on the electrodes, with no pre-stress effects. The maximum deflection of the beam tip was 2.1 μm for a bias of 7 V. These calculations have been done using the bulk value $d_{31} = -93 \cdot 10^{-12}$ C/N [3.17].

Modal analysis has also been performed for a beam of 800 μm length. In order to obtain the correct sequence of observed modes, it is important to model only half of the beam, imposing symmetric boundary conditions in the middle. Besides sparing computing time, it directly selects the symmetrical modes which can be excited. In Figure 3.16 a comparison between measurement and FE modal analysis for mode 5 is shown. The different modes can be unambiguously identified on the basis of their shapes. No symmetrical mode was found which corresponded to experimental mode 3, which lies at 191.6 kHz. This mode is characterized by a small amplitude as compared to the other excited modes. The measured and calculated frequencies for the different modes are shown in Table 3.2.

The largest difference (7 %), is found for the fundamental mode. We studied the effect of small variations of both geometry and material properties, in order to see how they affect the mode frequencies. However, the calculated frequency of the fundamental mode remains typically 5-8% too high compared to experiment, whereas the difference is of the order of 1 % for the higher modes. The reason could lie in the incorrect modelling of what happens at the clamped edge of the beam.

Modes	Experimental [kHz]	Si anisotropic [kHz]	Si isotropic [kHz]	Fitted [kHz]	Difference (%)
M1	24.4	28.1	27.4	26.3	7
M2	162	174	170	164	1.2
M3	191				
M4	459	488	475	457	0.4
M5	899	956	931	895	0.4

Table 3.2. Frequencies of experimental and calculated modes. The second last column (fitted) corresponds to an isotropic calculation using a Si Young's modulus of 10.8 $\cdot 10^{10}$ N/m^2 (tabulated value is 12.0 $\cdot 10^{10}$ N/m^2). The last column shows the relative difference between the best isotropic FE results and experiment.

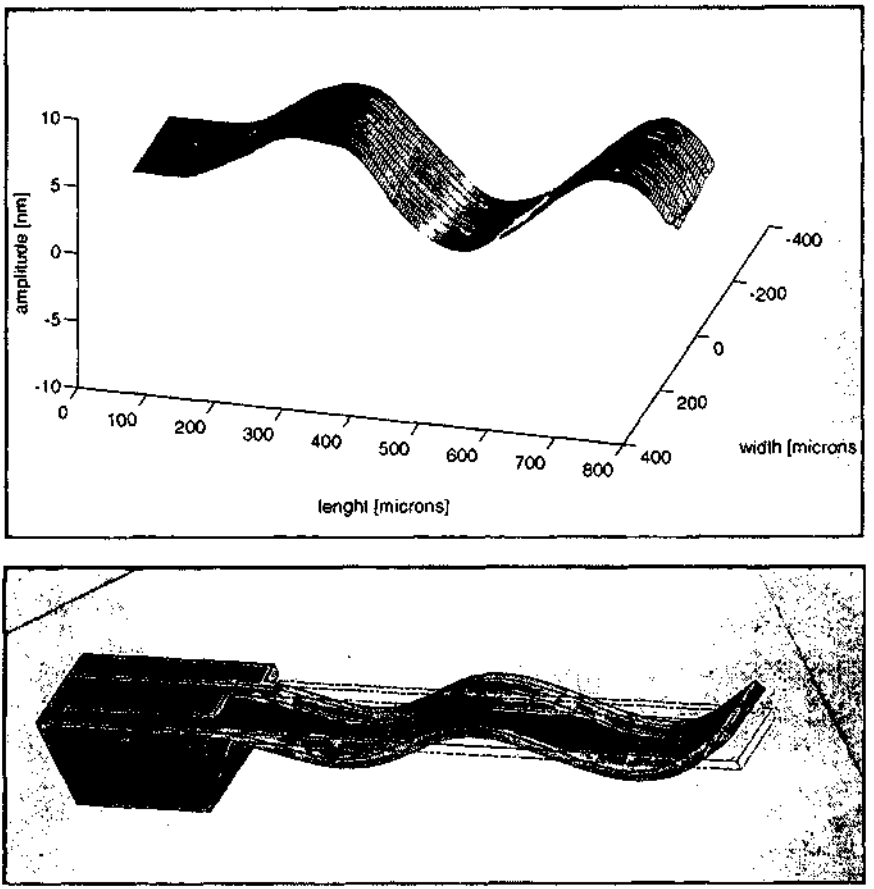

Figure 3.16: FE calculations (bottom, arbitrary units) and experimental (top) shapes for mode 5.

Finally, a harmonic analysis of the cantilever beam was performed. The measurements have been performed for a beam with a length of 1 mm. In the FE model the fundamental frequency was calculated to be 17.147 kHz whereas experimentally it is found to lie around 15.685 kHz. The measured quality factor (Q=380) was used for the FE calculations. In Table 3.3 the resonance amplitudes for bias voltages ranging from 0 to 12 V and an excitation signal of 10 mV are presented.

Bias voltage [V]	**Electric field [kV cm^{-1}]**	**Measured amplitude [nm]**	**d_{31} coefficient [C N^{-1}]**
0	0.0	181	$-9.00 \cdot 10^{-12}$
1	22.7	219	$-10.0 \cdot 10^{-12}$
2	45.4	262	$-12.0 \cdot 10^{-12}$
4	90.1	361	$-16.0 \cdot 10^{-12}$
6	136	462	$-21.4 \cdot 10^{-12}$
8	182	554	$-25.6 \cdot 10^{-12}$
10	227	617	$-28.5 \cdot 10^{-12}$
12	273	6648	$-30.0 \cdot 10^{-12}$

Table 3.3. Experimental amplitudes as a function of bias voltage. The last column shows the values of the d_{31} coefficients for which the calculations match experiment.

The large change in amplitude reflects the d_{31} dependence upon the bias potential, which gradually increases the polarization of the PZT layer. The FE harmonic results for the amplitudes are much higher (by a factor 3) than experiment if a bulk value of $-93 \cdot 10^{-12}$ C/N is assumed for the d_{31} coefficient. In the last column of Table 3.3 the values for which calculated amplitudes agree with measured ones are shown. One notices that for the highest bias of 12 V about one third of the bulk value for d_{31} is obtained. It is well known that in thin PZT layers, the polarization can be lower than half of the bulk value [3.7]. Here our 33 % of the bulk value is a worst case value because mechanisms which lower the amplitude are not taken into account here. However, we conclude that depolarizing effects, mainly due to the film geometry, are very important here.

3.4 References:

[3.1] T. Itoh and T. Suga, "Development of a Force Sensor for Atomic Force Microscopy Using Piezoelectric Thin Films", *Nanotechnology* **4** (1993) 218-224.

[3.2] T. Itoh, T. Ohashi, and T. Suga, "Scanning Force Microscope Using Piezoelectric Excitation and Detection", *IEICE Trans. Electron.*, Vol. E78-C. N0. 2 February 1995, pp.146-151.

[3.3] T. Fujii, S. Watanabe, M. Suzuki, and T. Fujiu, "Application of lead zirconate titanate thin film displacement sensors for the atomic force microscope", *J. Vac. Sci. Technol.* B 13(3), May/Jun 1995, pp. 1119-1122.

[3.4] T. Fujii, and S. Watanabe, "Feedback positioning cantilever using lead zirconate titanate thin film for force microscopy observation of micropattern", *Appl. Phys. Lett.* 68 (4), 22 January 1996, pp. 467-468.

[3.5] C. Lee, T. Itoh, R. Maeda, and T. Suga, "Micromachined Piezoelectric Force Sensors Based on PZT and PNNZT Thin Films", *Proc. of the 5th International Conference on Micro Electro, Opto, Mechanical Systems and Components*, Postdam, September 17-19, 1996, pp. 357-362.

[3.6] T. Itoh, C. Lee, and T. Suga, "Deflection detection and feedback actuation using a self-excited piezoelectric $Pb(Zr,Ti)O_3$ microcantilever for dynamic scanning force microscopy", *Appl. Phys. Lett.* 69 (14), 30 September 1996, pp. 2036-2038.

[3.7] K. Brooks, D. Damjanovic, N. Setter, Ph. Luginbuhl, G.-A. Racine and N. F. de Rooij, "Piezoelectric Response of PZT Thin Film Actuated Micromachined Silicon Cantilever Beams", *Proc. of the 9th IEEE International Symposium on the Applications of Ferroelectrics (ISAF'94)*, Pennsylvania, 1994, pp. 520-522.

[3.8] Ph. Luginbuhl, G.-A. Racine, Ph. Lerch, B. Romanowicz, K.G. Brooks, N. F. de Rooij, Ph. Renaud, and N. Setter, "Piezoelectric cantilever beams actuated by PZT sol-gel thin film", *Sensors and actuators*, vol. A-1-A-3, 1996, pp. 530-535.

[3.9] W.-S. Choi, and J. G. Smits, "Dynamic Behavior of ZnO on Si_3N_4 Bimorphs", 1992 *Ultrasonics Symposium*, pp. 319-322.

[3.10] J. G. Smits and W.-S. Choi, "Equations of state including the thermal domain of piezoelectric and pyroelectric heterogeneous bimorphs", 1992 *Ultrasonics Symposium*, pp. 1035-1038.

[3.11] J. L. Deschanvres, P. Rey, G. Delabouglise, M. Labeau, J. C. Joubert, and J. C. Peuzin, "Characterization of piezoelectric properties of zinc oxide thin films deposited on silicon for sensors applications", *Sensors and Actuators* A, 33 (1992), pp. 43-45.

[3.12] Q. Meng, M. Mehregany, and K. Deng, "Modeling of the electromechanical performance of piezoelectric laminated microactuators", *J. Micromech. Microeng.* 3 (1993), pp. 18-23.

[3.13] K. Lefki, and J. M. Dormans, "Measurement of piezoelectric coefficients of ferroelectric thin films", *J. Appl. Phys.* 76 (3), 1 August 1994, pp. 1764-1767.

[3.14] K. W. Kwok, H. L. Wah Chan, and C. L. Choy, "Evaluation of the Material Parameters of Piezoelectric Materials by Various Methods", *IEEE Transactions on Ultrasonics, Ferroelectrics, and Frequency control*, Vol. 44, N0. 4, July 1997, pp. 733-742.

[3.15] S. Mancha, "Chemical etching of thin film PLZT", *Ferroelctrics*, 1992, Vol. 135, pp. 131-137.

[3.16] J.G. Smits and W.-S. Choi, The Constituent Equations of Piezoelectric Heterogeneous Bimorphs, *IEEE Transactions on Ultrasonics, Ferroelectrics, and Frequency Control*, 38.(1991) 256-270.

[3.17] B. Jaffe, W.R. Cook and H. Jaffe, *Piezoelectric Ceramics* Academic Press, New York, 1971, pp.29, 146.

1436

4. Fundamentals of acoustic guided waves

4.1 Introduction

Classically, a wave is a disturbance of a medium, that medium being either a field (e.g. the gravitational and electromagnetic fields) or a material substance. In the case of material media, waves are known as mechanical waves, and depending on their amplitudes, are sometimes "splitred" in two families: elastic waves and acoustic waves. Initially, acoustic was the "physics of sound", but is now extended to all elastic waves at frequencies well below and above the audible range, propagating in a great variety of solid, liquid and gaseous media.

There are two basic forms of waves in solids: longitudinal (also called compressional or dilatational) and transverse (i.e. shear or distortional), but transverse waves do not exist in gases or liquids, because these media do not resist shear motion due to the lack of restoring forces. The unique exception is for Surface Acoustic Waves (SAW) that propagate along the free surface of a semi infinite substrate, first reported by Lord Rayleigh in 1885. Water waves, or more exactly propagating ripples generated by throwing a stone into calm water, are the most popular example of such surface waves, which are a combination of longitudinal and tranversal motions along the boundary between air and liquid.

Formally, any pertubation which propagates on the surface of a medium and disturbs only a small thickness of the surface layer (skin depth) is called an acoustic surface wave.

Mathematically, two sets of equations related first to the wave motion in the medium, and secondly to the boundary conditions (mechanical and

electrical if the substrate is piezoelectric) must be simultaneously satisfied to determine the propagating modes that will exist in the structure, which in fact represents a wave guide. If the substrate is not piezoelectric, the unique solution of the former equations are surface waves, also called Rayleigh waves.

Diverging in two dimensions only, part of the energy of guided waves decays in accordance to $1/r$ instead of $1/r^2$ and allow thus a propagation far from the source.

Since Rayleigh's mathematical demonstration, a tremendous research activity in the so called field of acoustic guided waves began and have found considerable application. Today, many applications of SAWs for signal processing (TV, mobile phone, video, radar, etc.) and other acoustic wave devices in chemical, biochemical and physical measurements, highlight their huge potential.

4.2 Basic types of acoustic guided waves in solids

In this section, a brief description of the most important acoustic wave guide types is presented.

4.2.1 Rayleigh waves

Rayleigh waves are surface waves propagating along the boundary of a homogeneous isotropic elastic half-space [4.1], [4.2], [4.3], and polarized in the sagittal plane (the plane formed by the normal vector to the substrate and the wave vector, cf. Figure 4.1). Surface particle motion is predominantly in the x_1-x_3 sagittal plane with amplitudes u_1, u_3 respectively, and pure modes occur when the energy flow and the wave vector have the same direction.

In order to have a wave guided by the free surface and staying in its neighborhood, the amplitude displacement u_3 must decay rapidly with depth. The two displacement components being coupled by the mechanical boundary conditions, a time-dependent retrograde elliptical surface displacement is therefore associated mechanically with the propagating wave. One particle motion is parallel to the wave direction and the other, 90° out of phase with the former in the time domain, is normal to the substrate. Both motions have their amplitude decaying exponentially, but differently, with the substrate depth [4.4].

Figure 4.2 depicts a calculated amplitude undulation on the free boundary of an isotropic elastic substrate. The resulting oscillation is a combination of both longitudinal and transverse (shear) motions which travel along the surface with identical velocities [4.5]. In classical elastic bodies, the Rayleigh wave velocity v_R is dispersionless, i.e. independent of frequency [4.6], and for example, has a value $v_R = 3410$ m/s for silica.

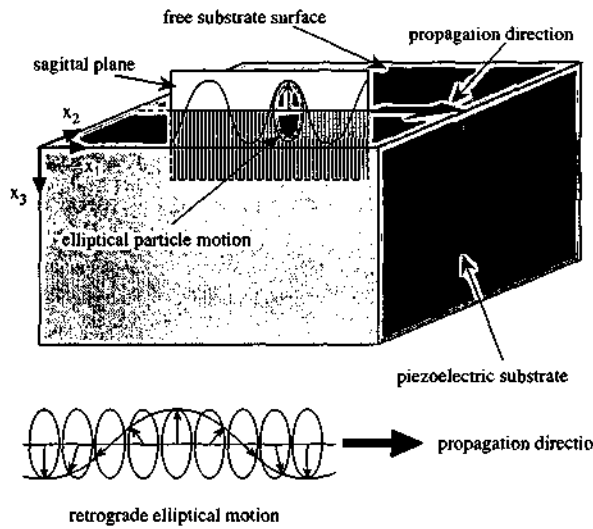

Figure 4.1: Schematic representation of elliptical Rayleigh wave motion in the sagittal plane on the surface of an elastic solid.

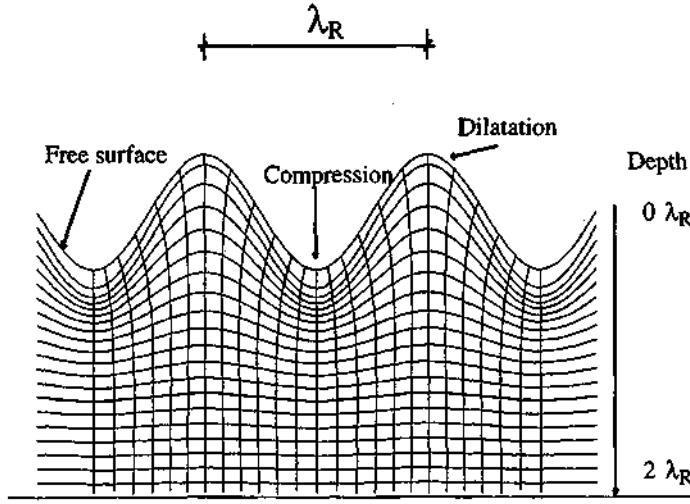

Figure 4.2: Computed amplitude displacements of Rayleigh waves (not to scale). Here, the represented substrate thickness is two wavelengths. The amplitude vanishes at a depth of approximately $2\lambda_R$. (In this example, $v_R=0.9c_t=0.315c_l$; v_R is the Rayleigh velocity, c_l and c_t are the longitudinal and transverse velocities in the bulk material).

Historically, Rayleigh waves have played an important role in the understanding of earthquakes, because they have the form of acoustic waves that propagate along the earth's crust (surface) after an earthquake, at a velocity below that of every other wave type, and are therefore always the last to be recorded on the seismograph.

When the substrate is piezoelectric, the wave pattern is more complex and the surface waves are called piezoelectric Rayleigh-waves [4.7].

At the present time, SAW devices (e.g. delay lines and bandpass filters) based on piezoelectric Rayleigh-waves propagating on quartz, lithium niobate ($LiNbO_3$) and lithium tantalate ($LiTaO_3$) substrates, are mass produced using

semiconductor microfabrication techniques, and allow to obtain on a single chip the same complex signal processing that would necessitate several hundred conventional inductors and capacitors in standard LC filters.

4.2.2 Lamb waves

Initially described by H. Lamb in 1917 [4.8], Lamb waves propagate in a free isotropic homogeneous elastic plate of finite thickness. The plate acts as a waveguide and Lamb waves have their two components lying in the sagittal plane, one normal to the plate and the other parallel to the wave direction. Figure 4.3 illustrates this situation.

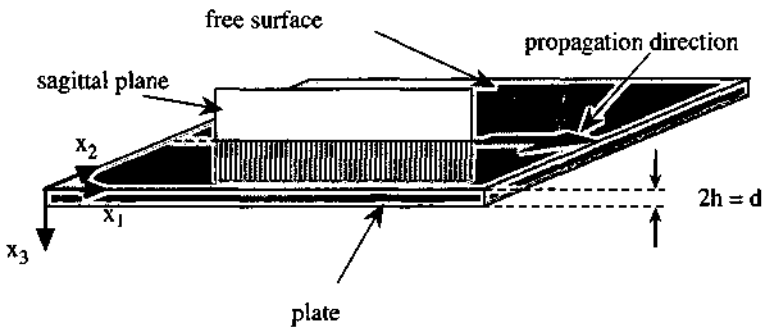

Figure 4.3: Schematic representation of the sagittal plane and the plate orientation for Lamb wave propagation.

An easy way to understand the existence of Lamb waves in a plate can be explained according to the following. When the plate thickness is greater than a few wavelengths λ, Rayleigh waves can propagate on each side of the plate and are considered as being not coupled with each other. As the plate thickness reduces to the order of the Rayleigh's penetration depth λ, both longitudinal and transverse components on each side interact and produce Lamb waves.

Thus, Lamb modes in a plate can be considered as a set of coupled longitudinal and transverse waves. Moreover, both transverse and longitudinal components are reflected on the plate free boundaries and partially transform into each other [4.4]. Since they are at the same frequency, they interfere and produce a great number of cyclic variations [4.9]. Figure 4.4 depicts this behavior.

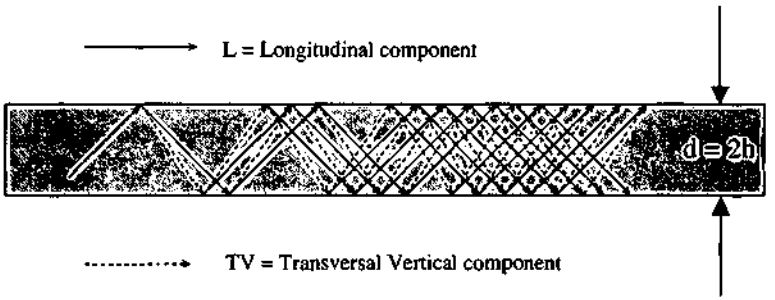

Figure 4.4: Schematic view of the reflection phenomena of longitudinal (L) and transverse vertical (T) waves, which characterizes the propagation of Lamb modes in a plate. Formally, the components L and T propagate with identical velocities and are reflected on the plate's free surfaces. During reflections, the (L) wave creates a (T) wave and vice versa. Interferences between both components also occur.

There are two types of Lamb waves: symmetrical and antisymmetrical modes which can propagate through the plate independently [4.5]. In Figure 4.5, the displacement pattern of both modes is shown.

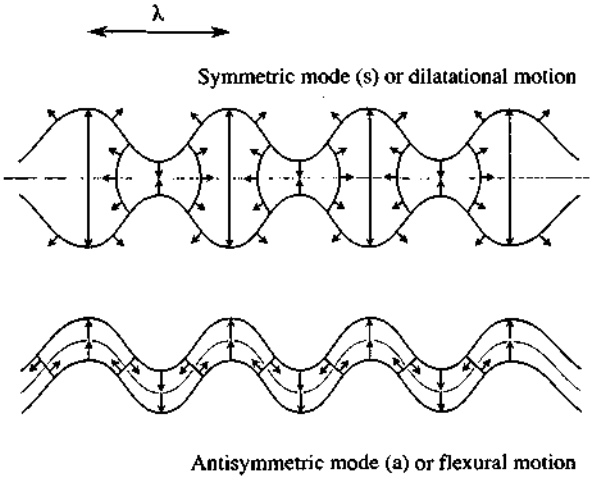

Figure 4.5: Pictorial cross sectional representation of the plate deformations related to symmetric and antisymmetric propagating Lamb modes. The symmetric (s) mode involves a dilatational motion: particle displacements are symmetric about the neutral plane. The antisymmetric (a) mode involves flexure: particle displacements are antisymmetric with respect to the neutral plane.

4.2.3 Acoustic plate modes (APM)

Like Lamb waves, plate modes propagate in a free isotropic plate, but with a pure shear horizontal polarization, i.e. the displacement is parallel to the plate surfaces and perpendicular to the direction of propagation [4.10], [4.11]. Figure 4.6 shows the propagation of such waves. It is interesting that they are successively reflected from the surfaces of the plate without being transformed, and with a reflection coefficient equal to one [4.6]. The acoustic energy is confined between the two upper and lower plate boundaries. When contacting a liquid, no energy is radiated into the liquid, due to the absence of surface-normal displacement.

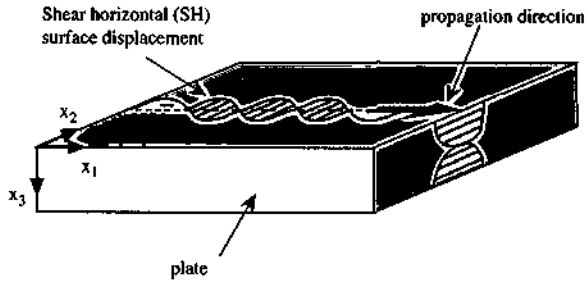

Figure 4.6: Schematic design of acoustic plate modes (APM) propagating in a free isotropic plate.

4.2.4 Bleustein-Gulyaev wave

On a free surface of a certain piezoelectric half-space, a shear horizontal piezoelectric wave can propagate [4.6], [4.12], [4.13]. Its penetration depth in the medium decreases exponentially but is of the order of about 100 λ for most piezoelectric media, and less than λ in case of strong piezoelectricity. Figure 4.7 represents a such typical wave.

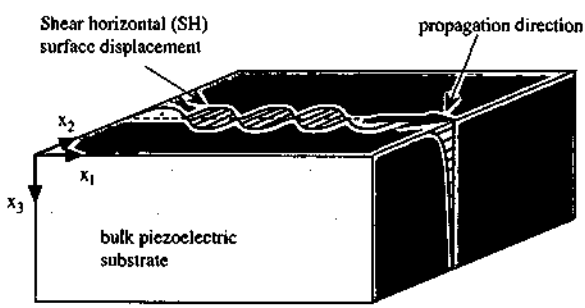

Figure 4.7: Propagation of a Bleustein-Gulyaev wave on the free boundary of a piezoelectric half-space.

4.2.5 Love waves

When a semi-infinite medium is covered by a thin layer, a so called Love wave (shear horizontally polarized) may propagate if the velocity in the guiding layer is lower than in the substrate [4.14], [4.4], [4.15]. In Figure 4.8, an example of this wave is depicted.

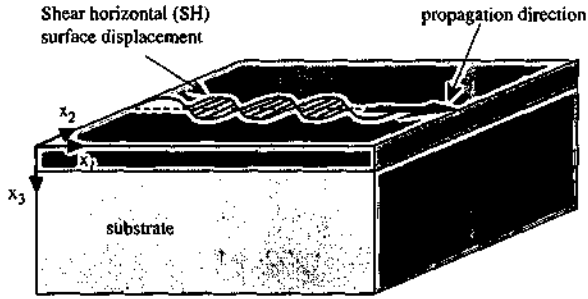

Figure 4.8: Love wave propagation. The thin film plays the role of an acoustic wave guide.

4.2.6 Stoneley waves

They represent a kind of wave which propagates at the surface of separation of two semi-infinite media in contact [4.16].

4.3 Behavior of Lamb waves in a free isotropic homogeneous thin plate

4.3.1 Rayleigh-Lamb frequency equations

As previously mentioned, longitudinal and transverse waves in a solid medium are the two basic wave-types. A longitudinal disturbance (L) generates a change in volume locally, while a transverse perturbation (T) does not.

Specific displacement vectors $\mathbf{u}_L$ and $\mathbf{u}_T$ are respectively associated with the former waves. The resultant displacement of a material point in the lattice is given by: $\mathbf{u} = \mathbf{u}_L + \mathbf{u}_T$.

A longitudinal wave involves dilatation (div $\mathbf{u}_L \neq 0$) and is thus associated with a scalar potential ϕ with the condition **rot** $\mathbf{u}_L = \mathbf{0}$. Transverse wave involves no dilatation (div $\mathbf{u}_T = 0$) and is therefore associated with a vector potential Ψ satisfying the condition **rot** $\mathbf{u}_T \neq \mathbf{0}$.

According to the Helmholtz theorem [4.17], the vector displacement $\mathbf{u}$ for material points in a free isotropic solid is written in the form:

$$\mathbf{u} = \mathbf{grad}\ \phi + \mathbf{rot}\ \Psi \qquad (4.1)$$

with the two potentials satisfying the equation of wave propagation:

$$c_l^2 \Delta\phi - \frac{\partial^2 \phi}{\partial t^2} = 0 \qquad (4.2)$$

$$c_t^2 \Delta\Psi - \frac{\partial^2 \Psi}{\partial t^2} = 0 \qquad (4.3)$$

where Δ is the Laplace operator, and c_l and c_t the longitudinal and transverse bulk wave velocities respectively. Hence, the vector displacement **u** derives from a scalar and a vector potential.

By considering the case of a plate having traction-free boundaries and the governing equations, for displacements, potential fields and stresses, a Rayleigh-Lamb frequency equation can be derived [4.5], [4.6], [4.18]. It appears that two types of uncoupled Lamb modes propagate in the plate: the symmetric and the antisymmetric (cf. Fig. 4.5). In the following, we consider waves propagating in a plate of thickness d = 2h along the positive x direction (c.f. Figure 4.9).

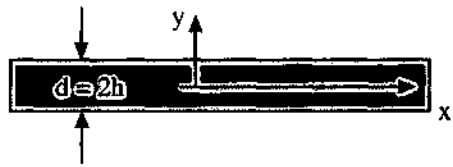

Figure 4.9: Cross section of the plate.

For symmetric waves, the frequency equation is given by:

$$\frac{\tan \beta h}{\tan \alpha h} = -\frac{4\alpha\beta k^2}{\left(k^2 - \beta^2\right)} \qquad (4.4)$$

For antisymmetric modes, the frequency equation is:

$$\frac{\tan \beta h}{\tan \alpha h} = -\frac{\left(k^2 - \beta^2\right)}{4\alpha\beta k^2} \qquad (4.5)$$

where

$$\alpha = \sqrt{\frac{\omega^2}{c_l^2} - k^2} \qquad (4.6)$$

$$\beta = \sqrt{\frac{\omega^2}{c_t^2} - k^2} \qquad (4.7)$$

c_l and c_t are the velocities of longitudinal and transverse acoustic waves in the bulk material, k is the wave number $2\pi/l$ related to the wave phase factor $(kx - \omega t)$, and ω is the angular frequency.

Equations (4.4) and (4.5) are the Rayleigh-Lamb dispersion equations (i.e. ω-k relations). Once the frequency ω is given, the wave numbers k satisfying these equations are determined using numerical solutions. Then the phase velocity (ω/k) and the group velocity (dω/dk) can be calculated.

Figure 4.10 exhibits the phase velocity curves for a plate having a Poisson ratio υ=0.34, after Viktorov [4.5]. On the vertical axis, the Lamb wave phase velocity c is normalized to the transverse velocity c_t . On the horizontal axis, the product $k_t h$ is the transverse wave number times the half-plate thickness h (i.e. d = 2h). Since $k_t = \omega/c_t$, figure 4.10 represents Lamb wave phase velocities of the first three symmetric (s_i) and antisymmetric (a_i) modes, as a function of the frequency-plate thickness product.

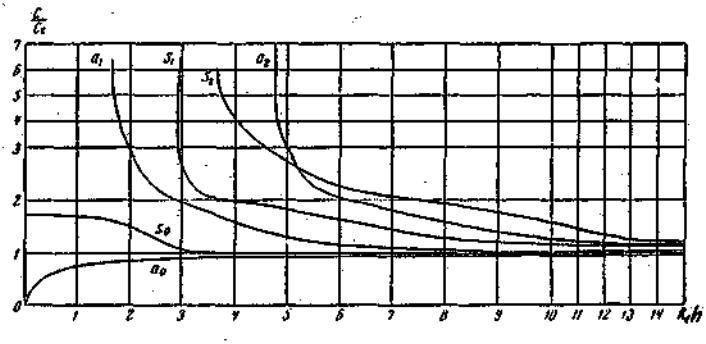

Figure 4.10: Rayleigh-Lamb frequency spectrum for a plate of thickness d=2h. The phase velocity c is normalized to the transverse bulk velocity c_t and plotted as a function of $k_t h = \omega h / c_t$.

The analysis of the Rayleigh-Lamb equations for a plate is more complicated than for SAWs over a semi infinite substrate, and analytical solutions are only possible in some cases by considering various regions for which we may have α and (or) β, real, zero, or imaginary.

In the following, a few of the most important Lamb wave properties are presented. Some of them can be directly interpreted by considering Figure 4.10.

(1) The number of Lamb modes increases with the plate thickness d. (2) Each mode is dispersive. (3) For a sufficiently thick plate, the phase velocity of nonzero modes converges to the bulk transverse velocity c_t, while the velocities of the two zero modes converge to the Rayleigh velocity v_R. (4) Only nonzero modes exhibit cut-off frequencies (i.e. critical values of $k_t h > 0$ for which they appear). (5) For a plate having its thickness d smaller than half of the acoustic wavelength (precisely $k_t h \leq 1.6$ i.e. $d = 2h \leq 0.51\ \lambda$), only two modes can propagate in the plate: the lowest-order antisymmetric mode a_0 (flexural) and the lowest-order symmetric mode s_0 (longitudinal). (6) As the plate thickness reduces, the phase velocity of the lowest-order antisymmetric

mode a_0 decreases to zero, while the phase velocity of the s_0 mode slowly reaches its maximal value. (7) For a very thin plate (i.e. $d << \lambda$) the a_0 mode is strongly dispersive, whereas the s_0 mode exhibits negligible dispersion.

4.3.2 Phase velocities of zero order Lamb modes

In this work, the thickness $d = 2h$ of the considered micromachined plate is about fifty times smaller than the wavelength λ. Hence, with $k_t h \cong 0.06$, only the lowest-order modes a_0 and s_0 with some harmonics will be investigated. Their phase velocities are respectively, Vpa_0 and Vps_0 , and can be appoximated using the first order Taylor's approximation for $\tan\beta h$ and $\tan\alpha h$ in the Rayleigh-Lamb dispersion relations (reduction to thin plates). These velocities are given by the following expressions [4.5]:

$$V_{pa_0} = \sqrt{\omega d}\ \sqrt[4]{\frac{E}{12\rho\left(1-\upsilon^2\right)}} \qquad (4.8)$$

$$V_{ps_0} = \sqrt{\frac{E}{\rho\left(1-\upsilon^2\right)}} \qquad (4.9)$$

where E is the Young's modulus, ρ the plate density, d the plate thickness, ω the angular frequency, and υ the Poisson ratio.

Knowing that $\omega = V_{pa0} \cdot k$, the phase velocity of the antisymmetric mode a_0 can be rewritten in the new form:

$$V_{pa_0} = kd\sqrt{\frac{E}{12\rho(1-\upsilon^2)}} \qquad (4.10)$$

With the two former equations (4.9) and (4.10), a simple relation between antisymmetric and symmetric phase velocities is thus obtained:

$$V_{pa_0} = \frac{kd}{2\sqrt{3}} V_{ps_0} \qquad (4.11)$$

It is also possible, for an isotropic plate, to express the lowest order Lamb wave phase velocities Vpa_0 and Vps_0 using the bulk transverse velocity c_t and the bulk longitudinal velocity c_l, or the plate density ρ with the elastic stiffness constants c_{11} and c_{12} [4.4]:

$$V_{pa_0} = \frac{kd}{\sqrt{3}} c_t \sqrt{1-\frac{c_t^2}{c_l^2}} = \frac{kd}{2\sqrt{3}} \sqrt{\frac{c_{11}-c_{22}}{\rho}} \sqrt{1+\frac{c_{12}}{c_{11}}} \qquad (4.12)$$

$$V_{ps_0} = 2c_t \sqrt{1-\frac{c_t^2}{c_l^2}} = \sqrt{\frac{c_{11}-c_{22}}{\rho}} \sqrt{1+\frac{c_{12}}{c_{11}}} \qquad (4.13)$$

the relations between bulk velocities and elastic stiffness constants in a isotropic media being:

$$c_t = \sqrt{\frac{c_{11}-c_{12}}{2\rho}} \qquad (4.14)$$

$$c_l = \sqrt{\frac{c_{11}}{\rho}} \qquad (4.15)$$

As an example, the former velocities Vpa_0 and Vps_0 are calculated in the cases of a 2 μm thick plate, the media being silicon and PZT-4.

For the silicon plate, which for simplicity is supposed to be isotropic instead of anisotropic, we obtain $Vps_0 \cong 7780$ m/s and $Vpa_0 \cong 282$ m/s (calculated with $c_{11} = 16.56 \cdot 10^{10}$ N/m^2, $c_{12} = 6.39 \cdot 10^{10}$ N/m^2, $\lambda = 100$ μm, and $\rho = 2329$ kg/m^3).

For the PZT-4 plate, the velocities are: $Vps_0 \cong 3563$ m/s and $Vpa_0 \cong 129$ m/s (calculated with $c_{11} = 13.9 \cdot 10^{10}$ N/m^2, $c_{12} = 7.8 \cdot 10^{10}$ N/m^2, $\lambda = 100$ μm, and $\rho = 7500$ kg/m^3).

A particular feature of Lamb waves in thin plates ($k_l h \cong 0.06$), is that the phase velocity of the flexural a_0 mode is much smaller than the sound velocity in water (1480 m/s at 20 ^{0}C) and generally, that of all other types of acoustic waves. Typically, the phase velocity of piezoelectric SAWs, bulk transversal or longitudinal waves is of the order of a few km/s. In soft materials (e.g. lead, indium), bulk longitudinal waves propagate at a velocity around 1 km/s. For Rayleigh waves in most piezoelectric substrates, the velocity is about 3-4 km/s, while a longitudinal wave can propagate in beryllium at a velocity up to 13.5 km/s [4.4].

Because of the low phase velocity of compressional waves in the majority of liquids, most SAWs acoustic devices are not suitable for operation in liquids. A coupling between the transverse vertical component of the acoustic field and the aqueous media occurs, and energy is thus radiated into the liquid. Depending on the application, this can be used for liquid atomizer purposes [4.19], but not for liquid sensing or pumping, due to the excessive loss.

Horizontally polarized SAW modes (e.g. Love waves and acoustic plate modes) can be used in sensor applications only, while the lowest order a_0 Lamb mode in a thin plate ($d << \lambda$) is particularly suitable for sensor and also mass transport (liquid and solid) applications, because almost no energy radiates into the liquid. Furthermore, a comparison of gravimetric sensitivities (i.e. the velocity change due to mass loading) of various acoustic sensors, indicates that the lowest order flexural plate wave devices are the most sensitive [4.20]. Finally, for liquid sensing, the sensitivity of the a_0 mode is much greater than that of the s_0 mode [4.21].

4.3.3 Group velocities of zero order Lamb modes

When the plate thickness is much smaller than the acoustic wavelength (i.e. $d << 0.51\ \lambda$), the group velocities Vga_0 and Vgs_0 of these lowest order modes are respectively:

$$V_{ga_0} = 2\sqrt{\omega d}\ \sqrt[4]{\frac{E}{12\rho(1-\upsilon^2)}} = 2V_{pa_0} \qquad (4.16)$$

$$V_{gs_0} = \sqrt{\frac{E}{\rho(1-\upsilon^2)}} = V_{ps_0} \qquad (4.17)$$

We see that the longitudinal propagating mode s_0 is nondispersive (i.e. is independent of the plate thickness) and that the group velocity of the flexural wave is two times its phase velocity.

4.4 Phase and group velocities for an isotropic, two layered thin plate

In most practical cases, micromachined Lamb wave devices require a thin piezoelectric film deposited on a supporting layer. The plate or membrane is therefore a composite structure. Here again, we consider the plate under the absence of traction boundaries, but composed of two different layers and having an overall thickness d much smaller than the acoustic wavelength λ. Under these assumptions, the lowest order Lamb wave phase velocities Vpa_0 and Vps_0 are respectively [4.22]:

$$V_{pa_0} = \sqrt{\omega}\sqrt[4]{\frac{E_1^*\left[(d_1-e)^3+e^3\right]+E_2^*\left[(d_2+e)^3-e^3\right]}{3(\rho_1 d_1+\rho_2 d_2)}} \qquad (4.18)$$

$$V_{ps_0} = \sqrt{\frac{E_1^* d_1 + E_2^* d_2}{d_1\rho_1 + d_2\rho_2}} \qquad (4.19)$$

where

$$E_i^* = \frac{E_i}{1-\upsilon^2} \qquad i = 1;2 \qquad (4.20)$$

and

$$e = \frac{E_1^* d_1^2 - E_2^* d_2^2}{2\left(E_1^* d_1 + E_2^* d_2\right)} \qquad (4.21)$$

The suffix i refers to the layer i = 1; 2. E_i is the Young's modulus, ρ_i the plate density, d_i the layer thickness, ω the angular frequency, and υ_i the Poisson ratio.

The group velocity Vg is calculated using the definition Vg = dω/dk. Hence we obtain respectively for the former modes:

$$V_{ga_0} = 2k\sqrt{\frac{E_1^*\left[(d_1-e)^3+e^3\right]+E_2^*\left[(d_2+e)^3-e^3\right]}{3(\rho_1 d_1+\rho_2 d_2)}} = 2V_{pa_0} \qquad (4.22)$$

$$V_{gs_0} = \sqrt{\frac{E_1^* d_1 + E_2^* d_2}{d_1\rho_1 + d_2\rho_2}} = V_{ps_0} \qquad (4.23)$$

As for a homogeneous plate, the symmetric mode is nondispersive and the flexural mode has a group velocity twice its phase velocity.

When the composite plate involves more than two different layers, phase and group velocities are obtained using numerical resolutions [4.23].

4.5 Propagation of flexural waves in a homogeneous thin plate with in-plane tension

Until now, the plate or membrane was always considered as being not subjected to internal tension. Practically this is not the case, since the plate's materials generally possess an intrinsic tensile stress, especially silicon nitride, platinum and PZT thin films. The membrane is therefore characterized by a residual tension T which effects the propagation velocity of Lamb modes. The

residual tension T along the direction of propagation in the membrane is expressed as a force per unit length: [T] = N/m.

Consider an isotropic, homogeneous thin plate ($d << \lambda$). The phase and group velocities of a lowest order a_0 propagating mode are respectively given by the following formulas [4.24]:

$$V_{pa_0} = \sqrt{\frac{T}{\rho d} + k^2 d^2 \frac{E}{12\rho(1-\upsilon^2)}} \qquad (4.24)$$

$$V_{ga_0} = V_{pa_0}\left(1 + \frac{V_{pa_0}^2(T=0)}{V_{pa_0}^2}\right) \qquad (4.25)$$

where

$$V_{pa_0}(T=0) = kd\sqrt{\frac{E}{12\rho(1-\upsilon^2)}} \qquad (4.26)$$

is the phase velocity of a traction-free plate (T=0), and Vpa_0 the phase velocity of a plate having a residual in-plane tension T.

Equations (4.24) and (4.25) indicate that the presence of a tension in the plate increase the phase velocity, while it decreases the group velocity, since $Vpa_0(T=0) < Vpa_0(T\neq 0)$.

4.6 Harmonic Lamb wave modes

The preceding phase and group velocity formulas apply to the lowest order symmetric and antisymmetric propagating modes (a_0 and s_0), at the fundamental frequency ω. Technically, the generation of Lamb waves is

performed with InterDigital Transducers (IDT's) which generally excite only *odd* harmonics at odd multiples (n = 1, 3, 5, ...) of the fundamental frequency ω(n=1). (For more detail, see section 4.10 and chapter 5).

Hence, with the relations:

$$V_{pa_0}(n) = \frac{\omega_n}{k_n} \; ; \quad k_n = \frac{2\pi n}{p} \; ; \quad n = 1,\ 3,\ 5,\ \ldots \tag{4.27}$$

(where p is the transducer periodicity) applied to equation (4.24) for example, we obtain the phase velocity $Vpa_0(n)$ of the n^{th} harmonic mode:

$$V_{pa_0}(n) = \sqrt{\frac{T}{\rho d} + \left(\frac{2\pi n}{p}\right)^2 d^2 \frac{E}{12\rho\left(1-\upsilon^2\right)}} \tag{4.28}$$

or the frequency ω_n at which the same n^{th} mode will occur:

$$\omega_n = \frac{2\pi n}{p} \sqrt{\frac{T}{\rho d} + \left(\frac{2\pi n}{p}\right)^2 d^2 \frac{E}{12\rho\left(1-\upsilon^2\right)}} \tag{4.29}$$

This reasoning is applicable to antisymmetric and symmetric modes, and their group velocities. Therefore, equation (4.25) can be extended to calculate the group velocities of the n^{th} harmonic components of the fundamental mode a_0:

$$V_{ga_0}(n) = V_{pa_0}(n)\left(1 + \frac{V_{pa_0}^2(n)(T=0)}{V_{pa_0}^2(n)}\right) \tag{4.30}$$

4.7 Harmonic Lamb modes ratio

In the following, only the lowest order (i.e. flexural) a_0 mode is investigated. First we consider the case of a stress free plate, then the plate having a residual in plane tension T.

4.7.1 Stress free plate

With the equations (4.10) and (4.27), we obtain the operating frequencies at which fundamental and harmonic modes appear in the plate.

$$\omega_n = k_n^2 d \sqrt{\frac{E}{12\rho(1-\upsilon^2)}} \qquad (4.31)$$

where

$$k_n = \frac{2\pi n}{p} \; ; \quad n = 1,\ 3,\ 5,\ \ldots$$

and p is the transducer period.

The ratios $\omega(n=3)/\omega(n=1)$ and $\omega(n=5)/\omega(n=1)$, calculated with formula (4.31) are respectively:

$$\frac{\omega_3}{\omega_1} = 9 \quad \textit{and} \quad \frac{\omega_5}{\omega_1} = 25 \qquad (4.32)$$

Hence, in a stress free plate, the harmonic ratios are integer multiples of the fundamental frequency ω_1. Additionally, because a_0 is a dispersive mode,

the operating frequency of its first harmonic (n=3) is 9 times the fundamental frequency instead of only 3 times. A similar frequency shift occurs for higher harmonics.

4.7.2 Plate with in-plane tension

In this case, the ratios ω(n=3)/ω(n=1) and ω(n=5)/ω(n=1), calculated with formula (4.29) are respectively:

$$\frac{\omega_3}{\omega_1} = 3\sqrt{\frac{A+9B}{A+B}} \quad and \quad \frac{\omega_5}{\omega_1} = 5\sqrt{\frac{A+25B}{A+B}} \tag{4.33}$$

where A and B are two constants defined by:

$$A = \frac{T}{\rho d} \quad and \quad B = k^2 d^2 \frac{E}{12\rho\left(1-\upsilon^2\right)} \tag{4.34}$$

With equations (4.33) we see that the operating frequencies of harmonic modes in a stressed plate are not integer multiples of the fundamental frequency ω_1. Furthermore, the ratios in (4.33) are smaller than those in a stress free plate, because:

$$\sqrt{\frac{A+9B}{A+B}} < 3 \quad and \quad \sqrt{\frac{A+25B}{A+B}} < 5 \tag{4.35}$$

4.8 Calculation of the residual in-plane tension T and the Young's modulus E of a composite thin plate

Both equations in (4.33) can be solved to find a set of two expressions for each unknown, A and B, respectively.

For the first set we use:

$$\omega_1 = k\sqrt{A+B} \quad ; \quad k = \frac{2\pi}{p} \tag{4.36}$$

$$\frac{\omega_3}{\omega_1} = 3\sqrt{\frac{A+9B}{A+B}} \tag{4.37}$$

and find:

$$A = \frac{9}{8}\left(\frac{\omega_1}{k}\right)^2 - \frac{1}{72}\left(\frac{\omega_3}{k}\right)^2 \tag{4.38}$$

$$B = \frac{1}{72}\left(\frac{\omega_3}{k}\right)^2 - \frac{1}{8}\left(\frac{\omega_1}{k}\right)^2 \tag{4.39}$$

For the second set we use expressions in (4.36) again and:

$$\frac{\omega_5}{\omega_1} = 5\sqrt{\frac{A+25B}{A+B}} \tag{4.40}$$

We obtain:

$$A = \frac{25}{24}\left(\frac{\omega_1}{k}\right)^2 - \frac{1}{600}\left(\frac{\omega_5}{k}\right)^2 \tag{4.41}$$

$$B = \frac{1}{600}\left(\frac{\omega_5}{k}\right)^2 - \frac{1}{24}\left(\frac{\omega_1}{k}\right)^2 \qquad (4.42)$$

The two sets are not mathematically independent, that is each set will give the same values for A and B. Practically, the frequencies ω_1, ω_3, and ω_5 are determined experimentally, and a choice between the first or the second set is sometimes necessary. This is especially the case when some harmonics are difficult to generate. Here we restrict our attention to the first set.

Using the definitions of A and B in (4.34), we can rewrite equations (4.38) and (4.39) in a new form:

$$T = \rho d\left\{\frac{9}{8}\left(\frac{\omega_1}{k}\right)^2 - \frac{1}{72}\left(\frac{\omega_3}{k}\right)^2\right\} \qquad (4.43)$$

$$E = \frac{12\rho(1-\upsilon^2)}{k^2 d^2}\left\{\frac{1}{72}\left(\frac{\omega_3}{k}\right)^2 - \frac{1}{8}\left(\frac{\omega_1}{k}\right)^2\right\} \qquad (4.44)$$

Hence, it is now possible to calculate the residual in-plane tension T and the Young's modulus E separately, once the frequencies ω_1 and ω_3 have been measured, and if the density ρ, the Poisson ratio υ and the thickness d are known. (The wave number k is fixed by the IDT geometry).

It is to be noted that experimental results (ω_1 and ω_3) allow only to calculate the ratios $T/\rho d$ and $E/\{12\rho(1-\upsilon^2)k^{-2}d^{-2}\}$.

In practice, the thickness d is known from the process or can be measured on test structures, while the density ρ is approximated by summing the densities of each layer which compose the plate. The same procedure is required for the Poisson ratio.

4.9 Calculation of the group velocity for the lowest order flexural mode a_0 propagating in a plate having a residual in-plane tension

Group velocity is a very important parameter, since it represents the velocity at which acoustic energy propagates along the plate. Here, a simple relation is derived, which allows an accurate calculation of the group velocity. From equation (4.44) we have:

$$\frac{E}{12\rho\left(1-\upsilon^2\right)} = \frac{1}{k^2 d^2}\left\{\frac{1}{72}\left(\frac{\omega_3}{k}\right)^2 - \frac{1}{8}\left(\frac{\omega_1}{k}\right)^2\right\} \qquad (4.45)$$

which can be substituted in equation (4.26), giving thus:

$$V_{pa_0}^2(T=0) = \frac{1}{72}\left(\frac{\omega_3}{k}\right)^2 - \frac{1}{8}\left(\frac{\omega_1}{k}\right)^2 \qquad (4.46)$$

Now, with equation (4.25) it follows:

$$V_{ga_0}(n=1) = V_{pa_0}(n=1)\left[1 + \frac{\frac{1}{72}\left(\frac{\omega_3}{k}\right)^2 - \frac{1}{8}\left(\frac{\omega_1}{k}\right)^2}{V_{pa_0}^2(n=1)}\right] \qquad (4.47)$$

Equation (4.47) is interesting, because it permits the group velocity to be calculated very accurately. It requires only the frequency values of the fundamental mode ω_1 , the first harmonic ω_3 and the phase velocity Vpa_0 , which can be obtained by measuring the frequency response of the device. (See chapter 7 for comparison with experimental results).

4.10 Generation of even harmonic Lamb modes

When the piezoelectric material exhibits strong piezoelectric properties (e.g. PZT), even harmonic Lamb modes can appear (see chapter 5). In the following, the same procedure as in sections 4.8 and 4.9 is applied to determine the set of coefficients A and B, and the group velocity, for the case of an even harmonic mode n=2. We obtain:

$$A = \frac{4}{3}\left(\frac{\omega_1}{k}\right)^2 - \frac{1}{12}\left(\frac{\omega_2}{k}\right)^2 \qquad (4.48)$$

$$B = \frac{1}{12}\left(\frac{\omega_2}{k}\right)^2 - \frac{1}{3}\left(\frac{\omega_1}{k}\right)^2 \qquad (4.49)$$

The group velocity is given by:

$$V_{ga_0}(n=2) = V_{pa_0}(n=2)\left[1 + \frac{\frac{1}{12}\left(\frac{\omega_2}{k}\right)^2 - \frac{1}{3}\left(\frac{\omega_1}{k}\right)^2}{V_{pa_0}^2(n=2)}\right] \qquad (4.50)$$

Hence, with equation (4.50) it is possible to calculate the group velocity of the first even harmonic mode. The operating frequency ω_2 corresponding to a measured even harmonic mode n=2, and the fundamental frequency ω_1 are determined experimentally. (See chapter 7 for comparison with experimental results).

4.11 References:

[4.1] Lord Rayleigh, "On waves propagating along the plane surface of an elastic solid", *Proc.London Math. Soc.*, Vol. 7, pp. 4-11, November 1885.

[4.2] R. M. White, "Surface Elastic Waves", Proceedings of the IEEE, Vol.58, N°. 8, August 1970, pp. 1238-1277.

[4.3] S. Datta, "Surface Acoustic Waves Devices", Englewood Cliffs. NJ. Prentice-Hall, 1986.

[4.4] D. Royer, E. Dieulesaint, "Ondes élastiques dans les solides", Tome 1 Propagation libre et guidée, pp.1-5, Masson, Paris 1996.

[4.5] I. A. Viktorov, "Rayleigh and Lamb Waves, Physical Theory and Applications", Plenum Press, New York, 1967.

[4.6] S. V. Biryukov, Yu. V. Gulyaev, V. V. Krylov, and V. P. Plessky, "Surface Acoustic Waves in Inhomogeneous Media", Springer-Verlag, Berlin, 1995, ch.1.

[4.7] W. Buff, "SAW Devices for Frequency Control, Signal Processing and Sensor Application", *Proceedings of the 8th European Frequency and Time Forum, EFTF 94*, Technical University Munich, Weihenstephan, Germany, March 9-11, 1994, pp. 573-589.

[4.8] H. Lamb, "On waves in an elastic plate", *Proc. Roy. Soc.* (London), Ser. A, 93:114, 1917.

[4.9] M. Redwood, "Mechanical Waveguides", Pergamon Press, New York (1960).

[4.10] S. J. Martin, A. J. Ricco, and R. C. Hughes, "Acoustic wave devices for sensing in liquids", *4th Int. Conf. on Solid-State Sensors and Actuators, 1987, Transducers '87*, pp. 478-481.

[4.11] J. C. Andle, J. F. Vetelino, and R. Lec, "An acoustic plate mode immunosensor", in *Proc. IEEE Ultrasonics Symp.* 1989, pp. 579-584.

[4.12] J. L. Bleustein, *Appl. Phys. Lett.*, 13, 412 (1968).

[4.13] Yu. V. Gulyaev, *Soviet Phys. JETP Lett.*, 9, 63 (1969).

[4.14] A. E. H. Love, "Some problems of geodynamics", Cambridge University Press, (1911 and 1926).

[4.15] J. Du, G. L. Harding, J. A. Ogilvy, P. R. Dencher, and M. Lake, "A study of Love-wave acoustic sensors", *Sensors and Actuators* A 56 (1996) pp. 211-219.

[4.16] R. Stoneley, "Elastic waves at the surface of separation of two solids", Proc. Roy. Soc. A 106, pp.416-428 (1924).

[4.17] P. Morse, and H. Feshbach, "Methods of theoretical physics", Vols. I and II. McGraw-Hill, New York (1953).

[4.18] K. F. Graff, "Wave motion in elastic solids", Dover Publications, New York (1975).

[4.19] M. Kurosawa, T. Watanabe, and T. Higuchi, "Surface Acoustic Wave Atomizer with Pumping Effect", *Proceedings IEEE 1995 Micro Electro Mechanical Systems (MEMS)* Amsterdam, The Netherlands, January 29- February 2, 1995, pp. 24-30.

[4.20] S. M. Sze, "Semiconductor sensors", New York, John Wiley & Sons, 1994, ch. 3.

[4.21] J. Wu, and Z. Zhu, "Sensitivity of Lamb Wave Sensors in Liquid Sensing", *IEEE Transaction on Ultrasonics, Ferroelectrics, and Frequency Control*, Vol. 43, N0. 1, January 1996.

[4.22] R. M. White, P. J. Wicher, S. W. Wenzel, and E. T. Zellers, "Plate-Mode Ultrasonic Oscillator Sensors", *IEEE Transaction on Ultrasonics, Ferroelectrics, and Frequency Control*, Vol. UFFC-34, N0. 2, March 1987.

[4.23] A. A. Nassar, and E. L. Adler, "Propagation and electromechanical coupling to plate modes in piezoelectric composite membranes", *Proc. IEEE Ultrason. Symp.*, 1983, pp. 369-372.

[4.24] S. W. Wenzel, and R. M. White, "A Multisensor Employing an Ultrasonic Lamb-Wave Oscillator", *IEEE Trans. Electron Devices*, Vol. 35, N0. 6, June 1988, pp.735-743.

1436

5. Piezoelectric transduction

5.1 Introduction

Until 1965, the generation of guided acoustic waves on piezoelectric or nonpiezoelectric substrates was done using several methods, like magnetoacoustic effect based on eddy currents created in a metal sample placed in a constant magnetic field [5.1], prismatic coupling block (wedge method) [5.2], or comb-like structures fabricated in a bulk metal plate associated with a quartz plate [5.3].

In 1965, White and Voltmer invented a piezoelectric transducer in the form of an interdigital comb, the so called InterDigital Transducer (IDT), which consists of a thin metallic electrode deposited on a substrate by a photolithographic method [5.4]. The IDT provides a direct and efficient piezoelectric coupling to surface waves, (i.e. allows the generation and the detection of SAW waves on a piezoelectric substrate due to elasto-electric conversion phenomena [5.5], [5.6]). Since this major invention, many applications based on various types of transducers (delay lines, filters, convolvers, resonators,...) especially for signal processing in telecommunications, have been realized.

Excitation of Lamb waves in a relatively thick piezoelectric plate [5.7], [5.8], [5.9], [5.10], [5.11], [5.12], or in a thin layered piezoelectric membrane [5.13], were achieved using the same IDT's technique.

Other methods for the generation of Lamb waves in non piezoelectric substrates are also possible, for instance using electrostatic excitation and

capacitive detection [5.14], stimulated thermal scattering [5.15], piezoelectric transducers bonded to a fused quartz rod [5.16], Lorentz force [5.17], and air coupled transducers [5.18].

The performance and reliability of piezoelectric thin film materials, coupled with their ability to generate Lamb modes in a very thin plate, make these materials important. At the present time, only two different types of piezo films have been widely used to excite Lamb waves in thin membrane: zinc oxide (ZnO) [5.19], [5.20], [5.21], [5.22], and aluminium nitride (AlN) [5.23].

This chapter deals with the basic operating principles of IDT's used for the generation and the detection of acoustic signals, and is based on standard models related to piezoelectric surface acoustic waves. Due to the fact that SAW signal processing represents a very wide domain, operating principles are restricted to general results only, which are supposed to be applicable to Lamb waves generated in thin piezoelectric composite membranes.

5.2 The interdigital transducer (IDT): operating principles

The interdigital transducer patterned on a piezoelectric substrate allows the transformation of a voltage signal into a mechanical deformation (converse piezoelectric effect) and vice versa (direct piezoelectric effect). As sketched in Figure 5.1, an IDT is formed by two interpenetrating comb-like electrodes, and each finger pair consists of two adjacent electrodes having opposite voltages.

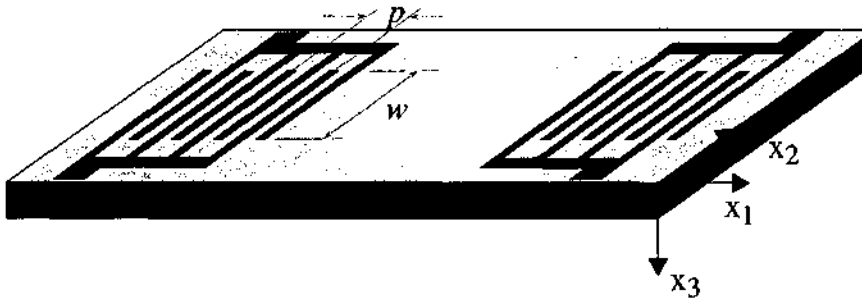

Figure 5.1: Schematic view of two identical IDTs on a piezoelectric substrate. Both transducers are characterized by a number N_p of finger pairs, an acoustic aperture w, and a transducer periodicity p. In this example, each finger electrode has a width of p/4 and the distance between the centers of two adjacent fingers is p/2.

In this work, only the elementary finger configuration is used, (i.e. each transducer has an uniform finger spacing and a constant finger overlap w (apodization)). Moreover, the separation between two adjacent electrode fingers is equal to their width (metallization ratio = 0.5).

One IDT is used as an input emitter while the other IDT plays the role of the output receiver. In fact, only the region under each IDT needs to be piezoelectric for energy conversion, while the area outside the transducers need only be elastic.

Propagating waves are created by an alternating voltage applied to the IDT (see section 5.3 for details about the generation of Lamb modes). The piezoelectric film reacts to the electric field by emitting two depolarization waves, a forward one and a backward one, which reduce the potential difference between the electrodes [5.24]. Formally, the interdigital transducer can be considered as an array of discrete ultrasonic sources which interfere coherently at specific frequencies only. The phase velocity of a given propagating n^{th} mode *n* in the substrate is:

$$V_{pn} = \frac{\omega_n}{k_n} \qquad n \in \mathbb{N}^* \qquad (5.1)$$

where ω_n is the angular operating frequency and k_n the wave number associated with the periodicity p of the transducer:

$$k_n = \frac{2\pi n}{p} \qquad n \in \mathbb{N}^* \qquad (5.2)$$

Hence, the IDT will excite acoustic waves at frequencies satisfying the condition:

$$\omega_n = V_{pn} \frac{2\pi n}{p} \qquad n \in \mathbb{N}^* \qquad (5.3)$$

The determination of the integers n which satisfy equation (5.3) is dependent on several factors, such as the piezoelectric material, the acoustic wave dispersion and the IDT geometry. In the simplest case (apodized transducers with a metallization ratio of 0.5), when the piezoelectric substrate is weakly piezoelectric (e.g. quartz or zinc oxide) and when the waves are not dispersive, the IDT emits only odd harmonics, and at odd integer multiples n =3, 5,... of the fundamental frequency [5.25]. An easy way to understand this result is given through Figure 5.2.

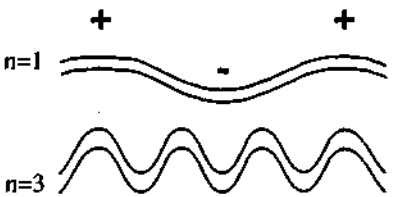

Figure 5.2: Schematic representation of odd harmonics generation.

When the acoustic waves are dispersive (e.g. Lamb waves), and under the same conditions as before, the IDT emits odd harmonics but not at integer multiples of the fundamental frequency (see chapter 4, section 4.7.2). Furthermore, if the piezo substrate is strongly piezoelectric (e.g. PZT), some even harmonics can be generated [5.26]. (c.f. chapt. 7 for experimental results).

For the fundamental mode n=1, when the excitation voltage is sinusoidal, each vibration adds constructively with the others only if the distance p/2 between two adjacent finger electrodes is equal to half the elastic wavelength λ of the acoustic perturbation. Therefore, the IDT coupling to piezoelectric acoustic waves is most efficient when the periodicity p of the transducer corresponds to the acoustic wavelength λ.

The operating frequency f_1 of the IDT, also called the *synchronous frequency*, is thus determined by its space periodicity λ through the relation:

$$f_1 = \frac{V_p}{\lambda} \qquad (5.4)$$

where V_p is the phase velocity of the acoustic wave.
For harmonic modes (n > 1), we substitute

$$\lambda_n = \frac{p}{n} \qquad n>1 \qquad (5.5)$$

in equation (5.3), and obtain:

$$f_n = \frac{V_{pn}}{\lambda_n} \qquad n>1 \qquad (5.6)$$

where f_n is the synchronous frequency of the n^{th} harmonic mode.

If the driving frequency of the IDT emitter does not exactly correspond to the synchronous frequency, the resulting signal will have a smaller amplitude, due to the fact that interferences between acoustic waves are not totally constructive.

After having crossed the membrane length, the electric potential associated with the piezoelectric acoustic perturbation induces a current flow in each comb of the IDT receiver. Both currents are then superimposed and detected in an external circuit.

5.3 Generation of the lowest order a_0 and s_0 Lamb modes

When an alternating voltage is applied to an IDT, two spacial periodic electrical field components E_1 and E_3 are present and can couple with acoustic modes in the sagittal plane. Depending on the piezoelectric substrate's thickness and its orientation, many modes may appear. In our case, the plate is much thinner than the acoustic wavelength (plate thickness << 0.51λ), satisfying thus the condition for having only the lowest propagating modes a_0 and s_0 with some harmonics.

The PZT film is about 0.7 μm thick while the IDTs finger's width is 25 μm. Hence, the electric field under each finger is essentially perpendicular and uniform (see Figure 5.3), and only the electric fields that are normal to the piezoelectric surface can play the primary role in flexural-plate wave transduction.

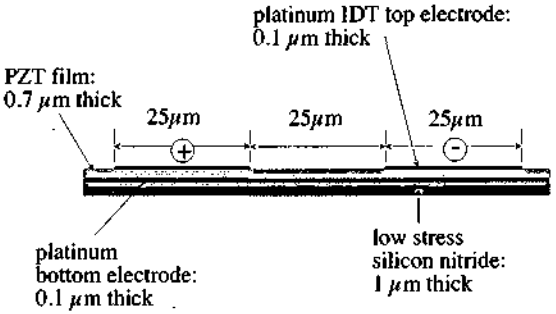

Figure 5.3: Cross section of the composite membrane showing the relative thickness of each layer (not at scale). The horizontal electric field between two adjacent electrode fingers can be neglected in comparison with that being produced normally to the plate. The bottom electrode is connected to a fixed potential.

Due to the polycrystalline aspect of the PZT thin film, having its grains randomly oriented, the ferroelectric layer, without remanent polarization, is similar to an isotropic material. However, if the randomly oriented domain polar vectors are switched under a constant external electric field, an anisotropy is created in the film. This anisotropy is essential to destroy the macroscopic center of symmetry which forbids piezoelectricity.

Practically, an anisotropy is locally performed in the material between the IDT top electrode and the botrom plane, by fixing the botrom electrode at a constant potential. The potential sign allows the direction of anisotropy in the PZT film to be fixed, and a poling axis under each comb to be created. Then, an alternating electric field, normally induced under each comb finger for the IDT excitation, is superimposed on the d.c. bias and acts as a source of variable stress and strain.

The propagation characteristics of acoustic waves under these conditions closely resemble to those of an anisotropic, inhomogeneous membrane.

Once the poling axis is fixed, or more exactly the direction of anisotropy, the transducers are driven differentially with respect to the ground plane, in order to have voltage and displacements of adjacent fingers 180^0 out of phase. The excited IDT can generate Lamb waves but not shear horizontal waves. The coupling of the normal electric field to transverse horizontal strain in the PZT film is principally due to the $d_{31}=d_{32}$ piezoelectric constants, which produces a local elongation or contraction of the piezo material under every finger electrode. Moreover, the superposition of the different layers in the plate must be asymmetric, in order to transform the former elongation and contraction into a bending motion. Figure 5.4 shows how each IDT's finger pair bends the plate in opposite phase.

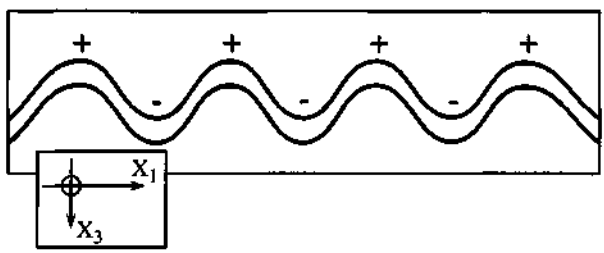

Figure 5.4: Cross sectional schematic representation of the membrane flexural motion. Each finger pair (+,-) of the transducer has its electrodes bending vertically (i.e. parallel to x_3) and in opposite directions (180^0 out of phase).

In a simple view, and by analogy with chapter 3, a driven IDT can be seen as an array of interpenetrating piezoelectric cantilever beams, patterned on a thin membrane and excited at their "fundamental resonance frequency". The alternating voltage, superimposed on the d.c. bias, bends two adjacent structures in opposite vertical directions, and constructive superposition of each periodic flexural motion occurs, when all of the structures are driven at the synchronous frequency.

For the generation of the symmetric s_0 mode, a combination of the d_{31} and the d_{33} piezoelectric constants is involved.

5.4 The transfer function response

A Lamb wave device having input and output IDTs represents a piezoelectric transmission line structure. In this work, most characterization of the Lamb wave devices have been done by measuring their frequency response, which gives basic information relative to the insertion loss as a function of the frequency. The frequency response is a powerful tool to perform a rapid diagnosis of the device's performance, and its ability to generate and detect acoustic waves.

Energy transfer between input and output IDTs can be modeled using the delta function model [5.27]. This model approximates the electric field under each comb finger as being normal to the piezoelectric surface, and the electric field distribution along the IDT as a discrete number of delta function sources. Figure 5.5 illustrates this electric field approximation.

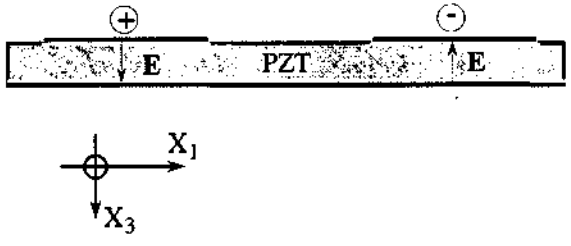

Figure 5.5: Approximation of the electric field under each comb finger, used in the delta function model. The electric field is normal to the piezo surface and components along the directions x_1 and x_2 are ignored.

The interdigital transducer is similar to an array of N discrete ultrasonic antennas, and the electric field amplitude is normalized to a value $|\mathbf{E}_3| = 1$. Summation over this array allows to transform the N progressive waves into an unique propagating wave (the bidirectionality of the emitter is not considered), issued from a middle position in the IDT. In our case, this position coincides with the transducer center and is also called the IDT phase center. Under these assumptions, the former summation applied to one IDT, yields its individual frequency response.

Hence, the total amplitude response of the device will depend on both IDT frequency responses, associated with an overall phase delay. The phase delay is essentially due to the propagating time of the signal along the acoustic path. In our case we consider only nondispersive waves. Under this condition, every frequency component of the input signal will be detected without distorsion, (i.e. they are attenuated and delayed in the same amount). Acoustic devices satisfying this condition are called delay lines. Figure 5.6 depicts this dependence.

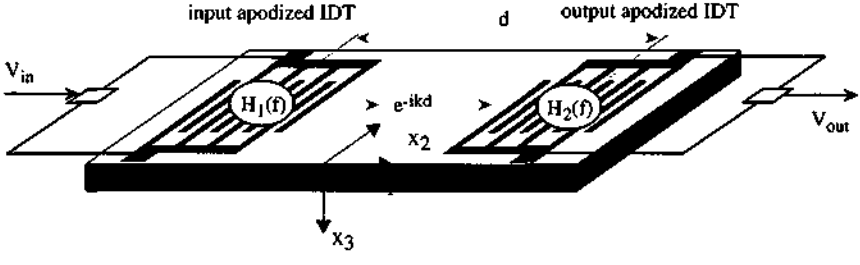

Figure 5.6: The three components of the overall transfer function in case of a linear delay line. $H_1(f)$ and $H_2(f)$ are the IDT individual frequency responses and e^{-ikd} the phase delay.

For a structure having identical input and output uniform IDTs, with symmetric apodization pattern, the overall transfer function H(f) is:

$$H(f) = \frac{V_{out}}{V_{in}} = H_1(f)H_2^*(f)e^{-ikd} \qquad (5.7)$$

where $|H_1(f)| = |H_2^*(f)|$, k is the wave number and d the distance between the midpoints of the two IDTs. With this simplest model, the phase shift is given by:

$$\varphi(f) = -kd = -\frac{2\pi fd}{V_p} \qquad (5.8)$$

where V_p is the phase velocity. Equation (5.8) shows that the phase delay varies linearly with the frequency f and is proportional to the IDTs separation d.

Using the delta function model, equation (5.7) gives [5.28]:

$$|H(f)| = |H_1(f)||H_2^*(f)| \cong N^2 \left\{ \left| \frac{\sin \frac{N_p\pi(f-f_0)}{f_0}}{\frac{N_p\pi(f-f_0)}{f_0}} \right| \right\}^2 \qquad (5.9)$$

where N is the number of comb fingers, $N_p=N/2$ the number of finger pairs, and f_0 the IDT synchronous frequency. Equation (5.9) shows that the frequency response is canceled when $N_p\pi(f-f_0)/f_0$ is a multiple of π. In that case, the superposition of each finger contribution is totally destructive. This condition defines the transducer bandwidth B:

$$B = \frac{2}{N_p} \qquad (5.9)$$

Thus, the transducer bandwidth between first zeros on either side of the synchronous frequency f_0 , is inversely proportional to the number of finger pairs. Figure 5.7 shows a calculated magnitute response |H(f) |for a device having two uniform apodized IDTs with 20 finger pairs. It is represented on a linear scale referring to the standard definition of the insertion loss:

$$IL = 10\log_{10}\frac{power\ at\ load\ without\ DUT}{power\ at\ load\ with\ DUT}dB = 20\log_{10}\frac{V_{out}}{V_{in}}dB \qquad (5.10)$$

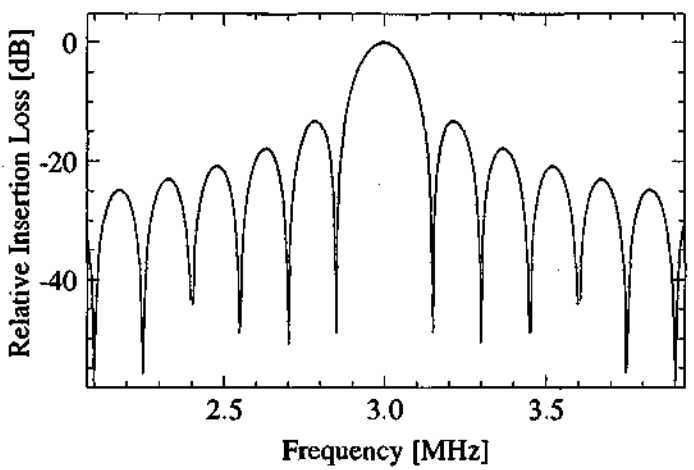

Figure 5.7: Calculated frequency response of a device having two uniform apodized IDTs, using the delta function model. Each transducer possess 20 finger pairs and the synchronous frequency is 3 MHz.

5.5 Frequency response degradation

The former results concern an ideal nondispersive device which is far removed from a real structure. In practice, many factors will perturb the frequency response. Consequently, the shape of an insertion loss measure is much more complicated than that of an ideal case. The following list is not complete but indicates the most common sources of degradation.

1) Edge reflection. This is the strongest cause of distortion for Lamb waves.

2) Electromagnetic feedthrough (cross talk) that arise due to mutual capacitive coupling betweeen the two transducers [5.29]. This r.f. (radio frequency) leakage is a very important source of perturbation . It propagates at the velocity of light and is superimposed on the detected signal at the output IDT. This coupling generates periodic ripples across the passband of the transducer at a frequency $f_r=1/\tau$, where τ is the acoustic delay time along the path between the IDTs.

3) Triple-transit-interferences (TTI) due to reflections of the acoustic waves between the two IDTs. In this case, periodic ripples are also produced across the output IDT passband, but at a frequency $f_r=1/2\tau$, because the wave is two times reflected before its interaction with the output signal.

4) Impedance mismatch between the generator resistance and the mechanical characteristic impedance of the device associated with acoustic power radiation.

5) Diffraction of the acoustic beam

6) Attenuation along the path in the piezoelectric material

7) Spreading of the wave packet due to dispersion

5.6 Electromechanical coupling coefficient K^2

This coefficient is a measure of how strongly the piezoelectric layer converts an applied electrical signal into acoustic depolarization waves. Experimentally, K^2 is measured using the relation:

$$K^2 = -2\frac{\Delta V_p}{V_p} \qquad (5.11)$$

Here, ΔV_p is the phase velocity change that occurs when the acoustic path length is covered by a thin metallic film, and V_p is the phase velocity of the unperturbated wave. As examples, for quartz (X axis), $K^2 = 0.001$, for $LiNbO_3$ (X axis) $K^2 = 0.045$, and for ZnO, $K^2 = 0.072$.

For harmonic modes, the coefficient K^2 may differ from the value for the fundamental mode [5.28].

5.7 References:

[5.1] K. N. Vinogradov and G. K. Ul'yanov, "Measurements of the velocity and attenuation of ultrasonic surface waves in hard materials", *Akust. Zh.*, 5(3) 1959, pp. 290-293.

[5.2] E. G. Cook, and H. E. Valkenburg, "Surface waves at ultrasonic frequencies", *Am. Soc. Testing. Mat. Bull.*, 198: 1954, pp. 81-84.

[5.3] A. G. Sokolinskii, "Technique for the Excitation and Reception of Surface Waves", Author's Certificate N0. 19297 (1958).

[5.4] R. M. White, and F. W. Voltmer, "Direct Piezoelectric Coupling to Surface Elastic Waves", *Appl. Phys. Lett.*, Vol. 17, 1965, pp. 314-316.

[5.5] B. A. Auld, "Acoustic Fields and Waves in Solids", Volumes 1 and 2, John Wiley and Sons, New York 1973.

[5.6] D. P. Morgan, "Surface-Wave Devices For Signal Processing", Elsevier, Amsterdam, 1985.

[5.7] K. Toda, "Lamb-wave delay lines with interdigital electrodes", *J. Appl. Phys.*, Vol. 44, N0 1, January 1973, pp. 56-62.

[5.8] K. Toda, "Frequency characteristics of an interdigital transducer for Lamb wave excitation", *J. Appl. Phys.*, Vol. 45, N0 12, December 1974, pp. 5136-5140.

[5.9] S. G. Joshi, and Y. Jin, "Excitation of ultrasonic Lamb waves in piezoelectric plates", *J. Appl. Phys.* 69 (12) 15 june 1991, pp. 8018-8025.

[5.10] A. Sawaguchi, and K. Toda, "Lamb Wave Propagation Characteristics on Water-Loaded $LiNbO_3$ Thin Plates", *Jpn. J. Appl. Phys.* Vol. 32 (1993) pp. 2388-2391.

[5.11] T. Laurent, and F. Bastien, " Lamb and shear-horizontal wave production by interdigital transducers deposited on both sides of a piezoelectric plate", *J. Acoust. Soc. Am.* 99 (5), May 1996, pp. 2876-2882.

[5.12] N. Kaewkamnerd, T. Takenaka, K. Sakata, and K. Toda, "Material Characterization of $(Bi_{1/2}Na_{1/2})_{0.94}Ba_{0.06}TiO_3$ Ceramic as a Lamb Wave Device Substrate", Sensors and Materials, Vol. 9, N0.1, 1997, pp. 47-55.

[5.13] K. Uozumi, K. Ohsone, and R. M. White, "Generation and detection of ultrasonic Lamb waves in a thin deposited film by using interdigital transducers", *Appl. Phys. Lett.*, 43 (10), 15 Novembre 1983, pp. 917-919.

[5.14] T. Giesler, and J.- U. Meyer, "Electrostatic excitation and capacitive detection of flexural plate-waves", *Sensors and Actuators* A, 36 (1993) pp. 113-119.

[5.15] J. A. Rogers, and K. A. Nelson, "Study of Lamb acoustic waveguide modes in unsupported polyimide thin films using real-time impulsive stimulated thermal scattering", *J. Appl. Phys.* 75 (3), 1 February 1994, pp. 1534-1556.

[5.16] J. Pei, F. L. Degertekin, B. T. Khuri-Yakub, and K. C. Saraswat, "In *situ* thin film thickness measurement with acoustic Lamb waves", *Appl. Phys. Lett.* 66 (17), 24 April 1995, pp. 2177-2179.

[5.17] M. A. Butler, S. J. Martin, J. J. Spates, and M.- A. Mitchell, "Magnetically-Excited Flexural Plate Wave Devices", *Transducers '97, 1997 International Conference on Solid-State Sensors and Actuators*, Chicago, June 16-19, 1997, pp. 1031-1034.

[5.18] W. Wright, D. Hutchins, and D. Schindel, "Air-Coupled Lamb Wave Tomography", *IEEE Transaction on Ultrasonics, Ferroelectrics, and Frequency Control*, Vol. 44, N0. 1, January 1997, pp. 53-59.

[5.19] S. W. Wenzel, B. A. Martin, and R. M. White, " Generalized Lamb-Wave Multisensors", *Ultrasonics Symposium Chicago* (USA), 1988, Proceedings, pp. 563-567.

[5.20] V. Rajendran, M, Koike, K. Hashimoto, and M Yamaguchi, "Lamb Wave Devices Employing ZnD-Film/Al-Foil Composite Structure", *Jpn. J. Appl. Physics*, Vol. 31 (1992) Supplement 31-1, pp. 216-218.

[5.21] M. Sato, T. Yamamoto, M. Takeuchi, and K. Yamanouchi, "Humidity Sensivity of Lamb Waves on composite Polyimide/ ZnO/ Si_3N_4 Structure", *Jpn. J. Appl. Physics*, Vol. 32 (1993) pp. 2380-2383.

[5.22] M. J. Vellekoop, G. W. Lubking, P. M. Sarro, and A. Venema, "Integrated-circuit-compatible design and technology of acoustic-wave-based microsensors", Sensors and Actuators A 44 (1994) pp. 249-263.

[5.23] N. Tirole, "Ondes de Lamb dans des membranes bimorphes AlN sur silicium: application aux microcapteurs de pression", Dissertation thesis submitted at the "Université de Franche-Comté", France, 1993, N0. d'ordre 352.

[5.24] M. Feldmann, and Jeannine Hénaff, "Surface acoustic waves for signal processing", Artech House, Norwood, 1989, chapt. 3.

[5.25] W. R. Smith, and W. F. Pedler, "Fundamental and harmonic-frequency circuit-model analysis of interdigital transducers with arbitrary metallization ratios and polarity sequences", *IEEE Trans. Microwave Theory and Techniques*, Vol. MTT-23, 1975, pp. 853-864.

[5.26] E. Dieulesaint and D.Royer, "Ondes élastiques dans les solides", Masson, Paris 1974, chapt. 7, pp. 282.

[5.27] R. Tancrell, and M. Holland, "Acoustic surface wave filters", *Proceedings of IEEE*, Vol. 59, pp. 393, 1971.

[5.28] C. Campbell, "Surface Acoustic Wave Devides and Their Signal Processing Applications", Academic Press, Boston 1989.

[5.29] S. G. Joshi, and N. M. Dube, "Radio frequency leakage in surface acoustic wave devices", *Ultrasonics Symposium Proceedings, IEEE*, Bengalore, India, 1975, pp. 418-421.

6. Lamb wave design and microfabrication technology

6.1 Introduction

With the emergence of bulk silicon micromachining [6.1], [6.2], by anisotropic etching [6.3], [6.4], and surface micromachining by sacrificial layer techniques [6.5], a broad range of diverse applications has been developed in the two last decades [6.6]. Although the standard IC technology known from microelectronics involves the sequential deposition of many different thin layers over a flat silicon wafer, it can be seen, strictly speaking, as a two dimensional or a planar process, the final devices being thin compared with the thickness of the wafer, without any gaps or free standing structures. Silicon micromachining offers the unique opportunity to increase the complexity of the former process by allowing the realization of complete real three dimensional devices [6.7]. In this way, thin composite membrane based devices occupy a small place but not negligible, and promise to significantly increase their field of potential applications in the next few years. One reason for this is that many improvements in thin film deposition processes, including piezoelectric thin films, have been achieved. This enables the superposition of several different layers having different elastic properties, for the fabrication of a final composite suspended thin membrane. A second reason comes from the rapid development in the area of complex microfabricated devices which utilize a membrane or a thin plate as a part of the active area for a sensing and for actuating purpose [6.8], [6.9], [6.10].

In the following, the conception and the technologies used for the realization of piezoelectric flexural plate-wave devices are described.

6.2 Design parameters and geometries

6.2.1 Membrane and IDT sizes specifications

Unlike other acoustic wave based components, micromachined flexural plate-wave devices require a very thin composite membrane having a thickness of only a few μm, and simply supported by a solid frame, generally made in bulk silicon, which provide good stiffness, stability and easy handling. Furthermore, each membrane area should be large enough to allow the generation and the detection of propagating flexural waves between two transducers separated by a distance of a few mm.

With these requirements, the microfabrication of FPW elements is considerably more complicated than other acoustic wave devices, which do not involve a fragile acoustically thin membrane as the physical support of the propagating signal.

In the field of SAW filters and delay-line applications, special computational programs enable a precise design of the IDT's geometry, referring to standard piezoelectric material constants and electromechanical coupling coefficient K^2 [6.11]. In our case, the different PZT layers which have been synthesized, exhibited various piezoelectric properties and tensile stresses over each wafer, depending on the process involved during the sol-gel deposition. It was therefore not possible to take into account some important parameters (e.g. the relative permittivity ϵ_r of the substrate, the in plane-tension) prior to the fabrication.

Moreover, as already encountered during the fabrication of the cantilever beams, the probability of metal diffusion through the PZT layer during the top electrode metallization, increases with the IDT area.

Such pinholes which dramatically create short-circuits with the ground electrode, strongly affect the fabrication reliability of ferroelectric thin film capacitor devices and necessitated for this project the use of IDT having a minimal area.

The question as to which dimensions and shapes should be used for the final membrane and the transducers, depends on several important factors, such as the wave phase velocity v_p, the separation distance d between the two transducer phase centers, the periodicity $p = \lambda$ of the IDT pattern which will determine the operating center frequency $f_0 = v_p/\lambda$ (i.e. the synchronous frequency), the acoustic aperture w (i.e. the overlapping finger length), the number N_p of finger pairs (affecting the wave amplitude as well as the IDT impedance and the bandwidth BW of the transducer), the wave reflection coefficient at the membrane edges and the acoustic attenuation α. Other aspects concern the angular spreading of the acoustic beam, the membrane rigidity, the resulting in-plane tension and resistance ability to external perturbations (pressure, stress and strain). Figure 6.1 exhibits some of this parameters.

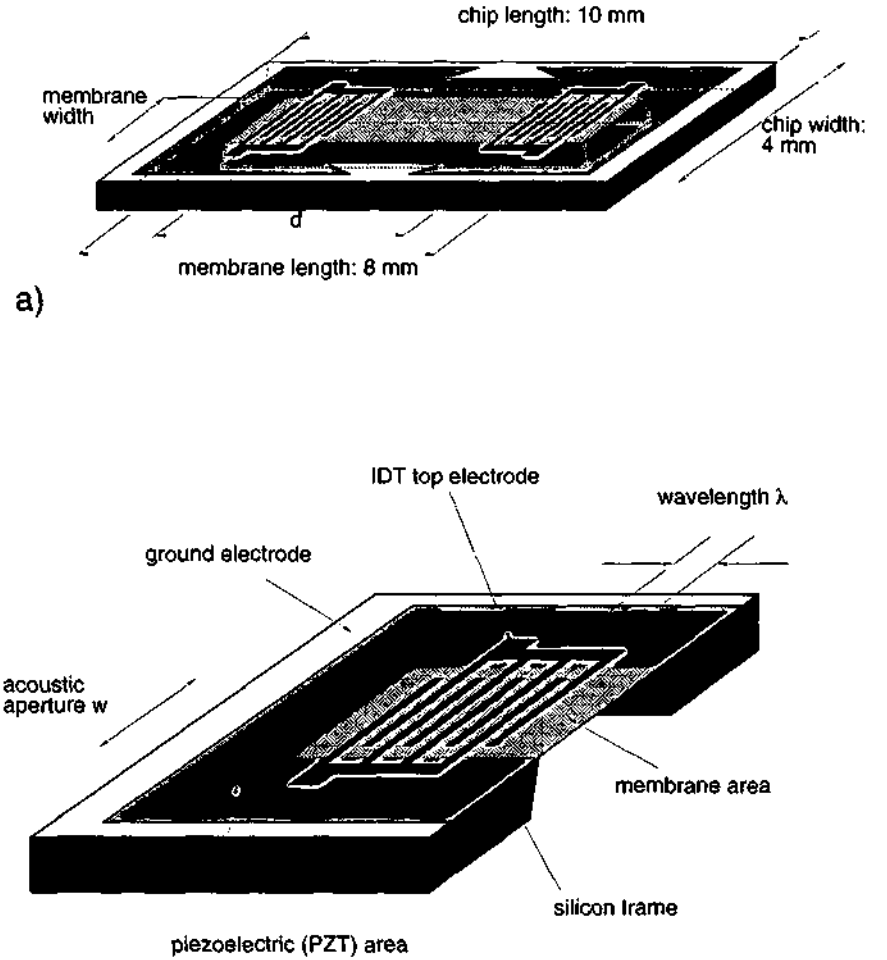

Figure 6.1:Schematic views of a silicon based micromachined Lamb wave delay line. (a) Each final device has 10 mm length and 4 mm width and is processed over a 3 inches, 380 μm thick silicon wafer. (b) Cross sectional view of the same device.

For acoustic Lamb wave propagation in a very thin membrane, the phase velocity $v_p = \lambda f_0$ of the a_0 mode can be of only a few hundred meters per second. Consequently, the group velocity v_g, that is the velocity of a given acoustic wavetrain or burst signal, will also be low. Selection of the membrane length depends thus on the desired time delay between the emission and the reception of pulses. A long propagation distance will allow the generation of bursts having up to 20 shots, and thus more accurate measurement of many parameters (group velocity, amplitude attenuation, ...) due to the relative good time separation between each detected signal. However, this will also greatly increase the fabrication difficulty.

The former velocities are determined by the physical parameters of each layer which compose the membrane (mass per unit area, thickness, in plane-stress) and remains constant as long as the plate is not perturbed. It is interesting that we can lower the driving frequency by increasing the wavelength which is in relation with the finger spacing (period p) of the IDT transducer. A low operating frequency in the MHz range is also convenient and thus allows the use of relatively simple and affordable electronic apparatus commonly employed in the generation and the detection of acoustic signals. However, the IDT period cannot be too large due to practical membrane size restrictions. Furthermore, the number N_p of finger pairs composing each transducer should be large enough, the wave amplitude being proportional to $(N_p)^2$, but not too large, the operating bandwidth of an IDT being inversely related to the number of finger pairs.

Having that in mind, a practical compromise in the IDT geometry and the membrane dimensions has been chosen.

Two generations of mask designs were conceived. In the first layout (also employed for the fabrication of piezoelectric cantilevers), many different configurations were selected to study the generation and the detection of Lamb

waves, including their mutual interactions when launched under various angles of incidence. Unfortunately, due to the quality of the piezoelectric layer (pinholes) and the passivation over the PZT areas, only a small percentage of the devices have shown the ability to produce Lamb waves. Therefore, instead of presenting a complete description of those structures, we restrict our discussion to only one or two, referring to them as structures belonging to the first generation.

The second layout concerns all devices presented in the following. For our applications, the dimensions of the final suspended membranes are 8 mm x 2 mm or 8 mm x 1 mm. Each interdigital transducer consists of 20 electrode pairs having a period of 100 μm, with uniform finger spacing (25 μm) and constant finger overlap length w (apodization) of 1.39 mm or 0.79 mm. The center-to-center IDT separation was 5.45 mm or 3.95 mm. Figure 6.2 shows a membrane length cross section, while Figure 6.3 points out the geometrical parameters used in the realization of an interdigital transducer.

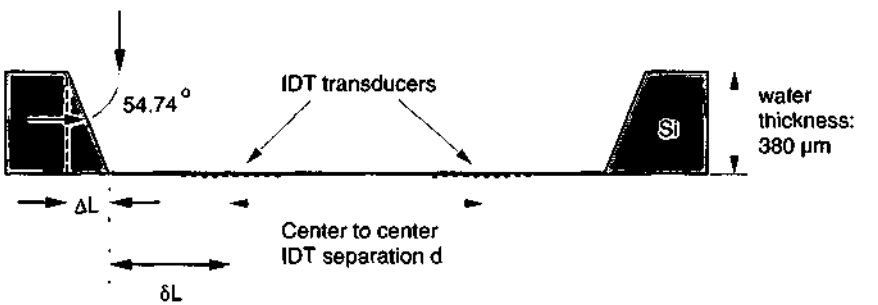

Figure 6.2: Cross sectional view of the FPW device. Compared to the mask design, for a 380 μm thick wafer, the final suspended membrane will have the dimensions reduced by an amount of ΔL = 269 μm. δL represents the distance from the membrane edge to the middle of the transducer.

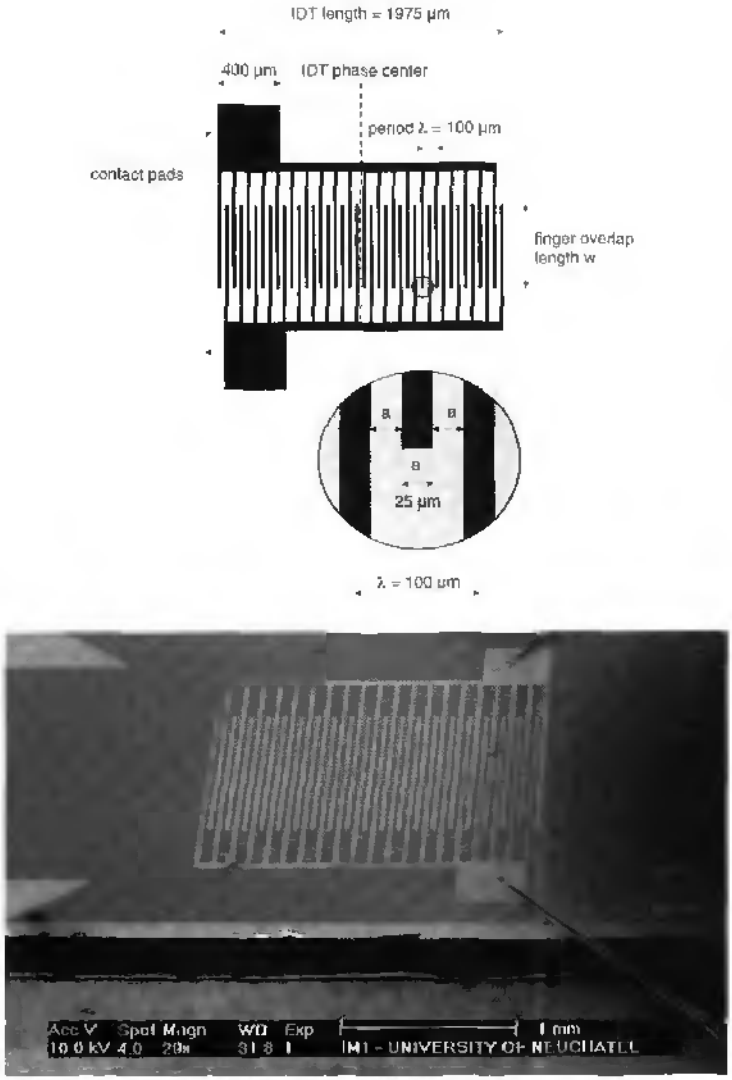

Figure 6.3 (Top) Basic geometry and dimensions of an IDT. The phase center is exactly located in the middle of the transducer, between two fingers. Each finger has a constant width of 25 µm. The distance between two adjacent finger centers is λ/2 = 50 µm. Maximal acoustic energy is concentrated in a region having the same width as the finger overlap length w. (Bottom) SEM picture of a IDT connected with Al wires bonds. The entire IDT area, including the two contact pads, is deposited over the PZT layer.

Due to the finite width of the transducer aperture, the FPW beam radiated by the emitter will be subject to angular spreading. According to classical optics, the Fresnel parameter F for a radiating IDT is given by [6.12]:

$$F = \frac{\lambda d}{w^2} \qquad (6.1)$$

where λ is the wavelength, d the acoustic path between the transducers, and w the finger overlap length. In our case we obtain F = 0.87 (calculated with λ=100 μm, d = 5.45 mm and w = 0.79 mm).

Low values (F< 1) correspond to a FPW radiation pattern roughly in the form of a parallel beam (i.e. in the *near-field* region approximation). This condition enables minimal distortion and maximal amplitude of the detected signal.

Finally, to summarize some important parameters involved in the generation and the detection of Lamb waves, let us consider the following example.

Realistically, with a FPW device having an acoustic path length of 5 mm and a group velocity of 400 m/s, the time delay for a single Dirac pulse is 12 μs. Generally we use a sine carrier waveform to produce bursts of several shots. If the IDT driving frequency is 3 MHz, a 20 shot burst has a length of 6.67 μs and is extended over a distance of 2.67 mm along the acoustic path. Under these assumptions, the acoustic wave-front reaches the IDT receiver 5.33 μs before the last shot in the burst signal has been activated.

In relation to our former choice of dimensions, for an aperture w = 1390 μm, a wavelength λ = 100 μm and the same acoustic path length d = 5 mm, we obtain F = 0.26.

6.2.2 IDT emitter and receiver configurations

In a bidirectional IDT emitter, half of the acoustic energy is generated in the backward direction and represents a possible strong distortion of the transfer characteristics if no precaution has been taken. Multiple interferences of reflected waves with the main signal can severely affect the IDT performance.

Because the intended use of the FPW devices is mechanical and fluid translation, the devices are designed to make maximal use of acoustic energy. Therefore, rather than damp or dissipate spurious reflections from the edges, for instance, with absorbers at the membrane ends, and/or split IDTs, the majority of the FPW structures are designed to take constructive advantage of the reflections at the membrane clamps. Only a few FPW devices were designed with their IDTs split in order to study the waves reflection.

Generally, in SAW applications, unidirectionality of an IDT is achieved by the use of split-electrode geometries [6.13], [6.14]. Unidirectional transduction can also be achieved by using two identical transducers separated by a distance $(n+1)\lambda/4$ ($n \in N$), [6.15]. In this case, two separate generators drive the IDTs 90^0 out of phase. Figure 6.4 shows an optical view of a unidirectional Lamb wave actuator with two similar IDTs deposited on a 0.3µm thick PZT film. Each IDT has 20 finger pairs with a period of 100 µm. The distance between both phase centers is 2075 µm, that is n = 82. This device belongs to the first FPW generation.

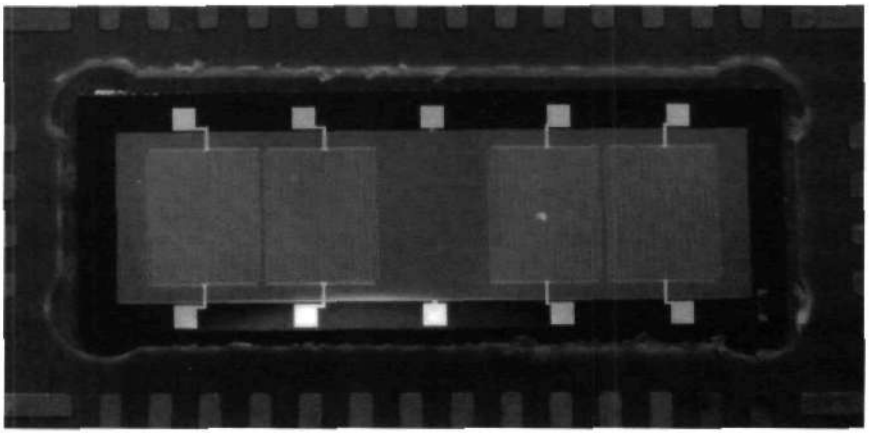

Figure 6.4 Optical view of a unidirectional FPW transducer. The two identical IDTs are separated by a distance of 2075 μm (n = 82).

For FPWs, such unidirectionality can also be simply obtained by placing the midpoint of the transducer relative to the membrane edge, at a distance for which the reflected waves will constructively interfere with the main signal.

In Figure 6.5 the back emission (2) is reflected (3) and superimposed on the main signal (1). Strictly speaking, the actuation of the IDT generates a progressive wave (1) superimposed on a standing wave (not represented in the picture) due to the membrane boundaries. A part of the emission (2) is absorbed at the edge while the other part is reflected, and a phase change occurs, depending on the transmission coefficient. The superposition of the two beams (1) and (3), having different amplitudes, therefore depends strongly on their interferences, that is on their phase difference. Relative to beam (1), beam (3) is affected by a first phase change $\Delta\varphi_1$ due to the edge reflection and by a second phase change $\Delta\varphi_2$ due to the delay distance $2\delta L$. In this case, a complete real physical description of the reflection, the absorption and subsequent superposition mechanisms for flexural wave beams in a piezo-composite thin plate is a complex task.

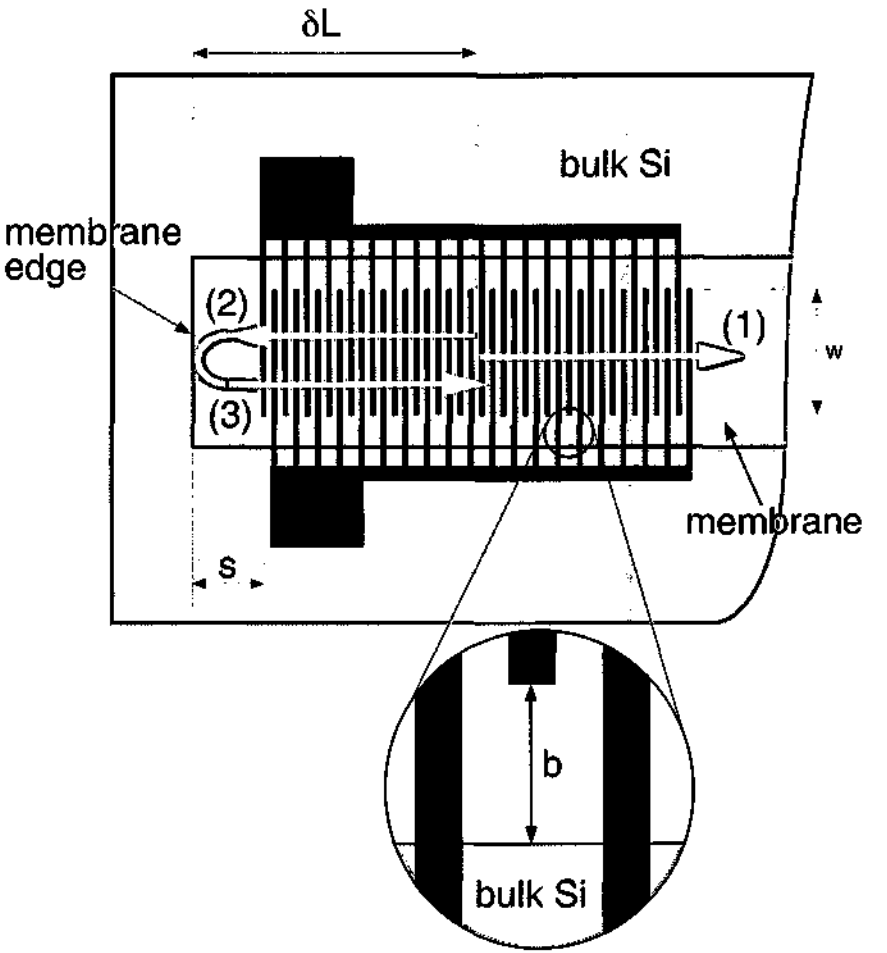

Figure 6.5: Schematic view of the wave edge reflection and superposition at the IDT emitter. Maximal constructive interferences between reflected beam (3) and main signal (1) occurs when they are in phase. Owing to a 180° phase shift by the reflection, the midpoint of the transducer is located at a distance δL from the edge which cancel the former phase shift. In the bottom zoom view, the distance b (125 μm or 325 μm) between the bulk Si and each finger end, ensure destructive lateral interferences.

For simplicity, and without experimental results a priori, the amplitude of the reflected wave (3) is supposed to be equal to that of the incident wave (2), and out of phase by $\Delta\varphi_1=180^0$ relative to the incident wave, the angles of incidence and reflection being equal. Maximal constructive interference with beam (1) is then possible when the second phase change cancels the first, i.e. only if $\Delta\varphi_1 + \Delta\varphi_2 = n2\pi$ $(n \in Z)$. Under this condition, the delay distance $2\delta L$ must be an odd multiple of $\lambda/2$.

Possible lateral interferences between the bulk trench and the extremities of each finger ends are suppressed by choosing a distance b corresponding to an odd multiple of $\lambda/2$. Lateral reflections are neglected in this case.

Figure 6.6 shows two IDT's configurations. Design (a) is symmetric with an acoustic path length d = 5450 μm. Both have their midpoint located at a distance δL = 1275 μm from the border. The resulting odd multiple of $\lambda/2$ condition is given by n = 51. Design (b) is asymmetric, the right IDT midpoint being positioned at a distance $\delta L'$ = 2773 μm. In that case, the odd multiple of $\lambda/2$ is n = 110.92 ≅ 111. For both designs, each transducer can be used as a transmitter-receiver.

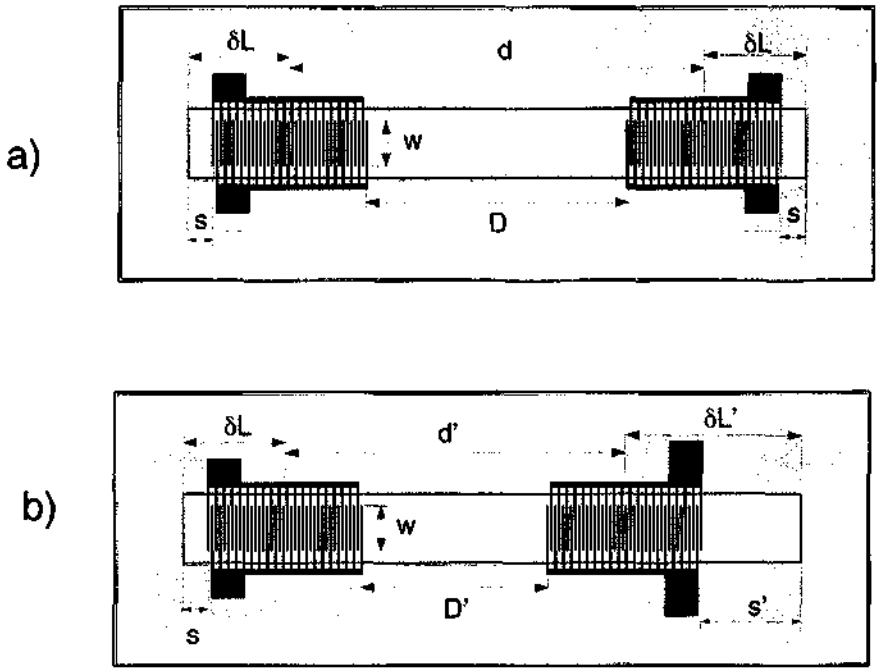

Figure 6.6: Two IDT's configurations with some design parameters. (a) δL = 1275 μm, s = 300 μm, w = 790 μm, d = 5450 μm, D = 3500 μm. (b) δL' = 2773 μm, s' = 1800 μm, d' = 3953 μm, and D' = 2000 μm.

A simple method to reduce edge reflections is to use slanted IDTs. Some FPW devices were designed with their IDTs inclined relative to the membrane clamps. In Figure 6.7, the slanting IDT provides an oblique reflection (3) of the incident beam (2). As the plane wavefront (width w) reaches the membrane edge, part of the wave is refracted (not on the picture) and part is reflected. Each border point between A and B acts as a partial emitter of a reconstructed wavefront AC. Phase matching along AB requires that the angle of incidence and reflection be equal (Snell's law). Therefore, beam (3) has the direction for which maximal reflected intensity occurs. If the angle $\theta \neq 0$ is correctly selected, the result will be a minimal perturbation of the main signal (1).

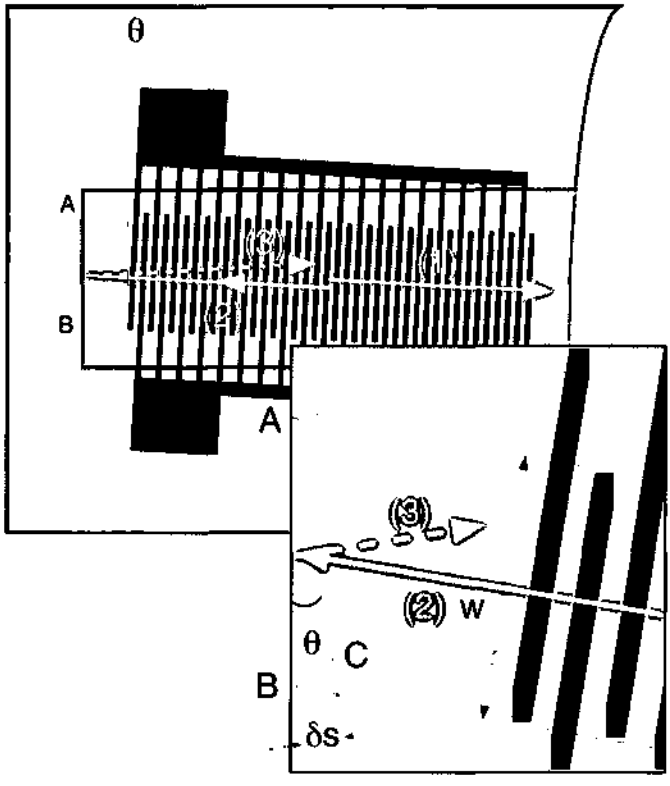

Figure 6.7: Wavefront geometry for reflection. The reflected wavefront AC is formed of waves scattered by the border AB. Just as the first wavelet arrives at C from B, the source A emits, and the wavefront along AC is completed. For some values of θ, destructive interferences occur and beam (1) suffers less perturbation.

With the condition of destructive interferences applied to wavelets emitted from A and B :

$$\delta s = (2n+1)\frac{\lambda}{2} \quad (n \in N) \qquad (6.2)$$

and with the relation

$$\delta s = w \tan\theta \qquad (6.3)$$

we find:

$$\tan\theta = (2n+1)\frac{\lambda}{2w} \quad (n \in N) \qquad (6.4)$$

As example, for our values λ = 100 μm and w = 790 μm, the first and second angles of destructive interferences are θ (n = 0) = 3.62°, and θ (n = 1) = 10.75°, respectively. Of course, the cancellation will be somewhat more accurate at larger n values, but will necessitate a larger membrane.

In our case, due to practical membrane size restrictions, only two values θ = 1° and θ = 2° were selected. Figure 6.8 exhibits a unit cell of the mask design employed for the fabrication of FPW devices with a slanted angle θ = 2°.

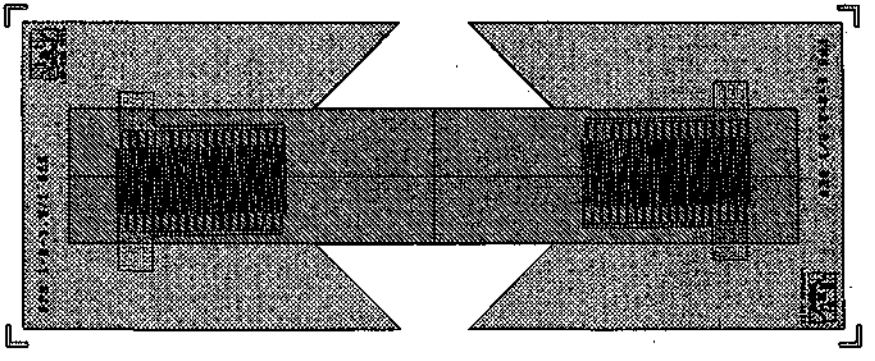

Figure 6.8: Printout of a slanted device with two mask levels used in the Lamb wave delay line fabrication. The slanted angle is 2°.

In conclusion, as micromachined membranes have finite dimensions, the problem of parasitic reflections will always be present. Some techniques which are applicable for SAW devices to suppress or to re-absorb unavoided edge reflections have less effect when transferred to Lamb wave based delay lines. This is especially the case with the simplest method of using a wax absorber behind each IDT. Since the amplitude of SAW propagation is extremely small (a few angströms), the acoustic signal will be almost completely absorbed by any soft layer present on the rear. For Lamb waves, the displacement amplitude can be of the order of a few hundred angströms [6.16], making it more difficult to totally absorb the incoming wave.

In this work, six different Lamb wave designs compose the second layout generation. Figure 6.9 shows three mask levels of the final design and the disposition of FPW devices over the entire wafer.

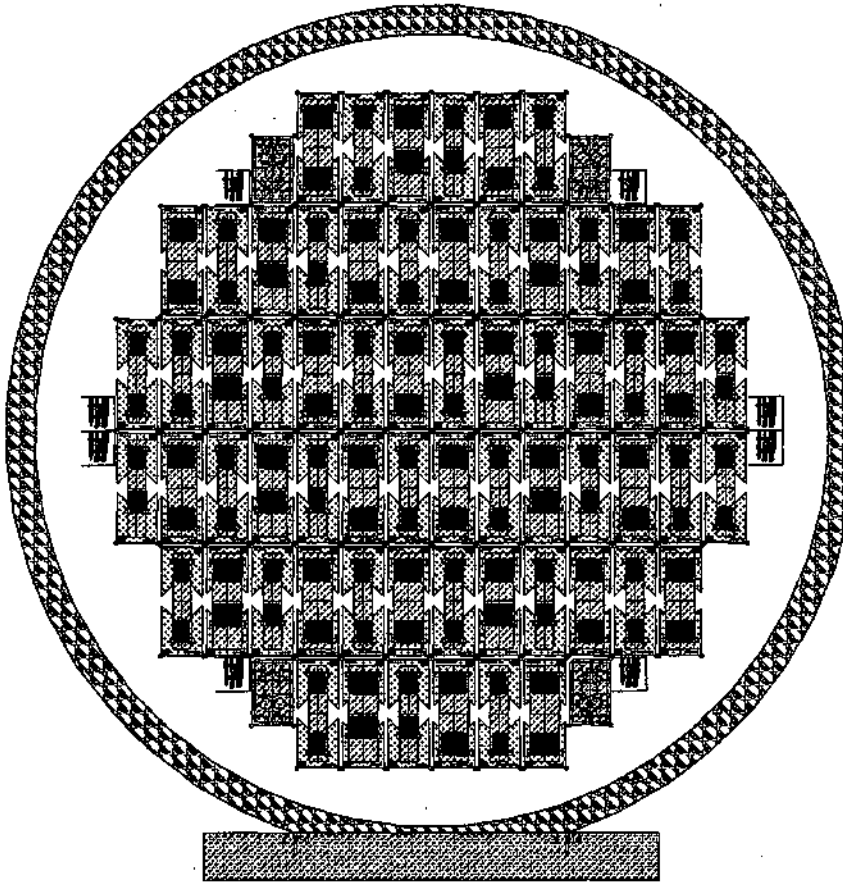

Figure 6.9: Printout of the mask set. Three levels are present (corresponding to different patterns): the membrane areas, the PZT layer and the IDT transducers.

6.3 Fabrication sequence

Acoustic delay lines of the second generation were fabricated using the following fabrication sequence. Starting from a (100) silicon substrate, the composite acoustic membranes were fabricated by sequential deposition of one micron of low-pressure chemical-vapor deposited (LPCVD) low-stress silicon nitride (Si_xN_y), a metal ground plane of tantalum/platinum (10 nm/150 nm), and a 750-nm-thick layer of sol-gel-derived PZT. The relatively thick PZT film was prepared by a sol-gel method and involved multiple deposition and annealing sequences. The complete details of the film-preparation process have been described in chapter 2.

The PZT thin-film capacitor is then patterned by photolithography and wet chemical etching in an ammonium fluoride etchant (BHF) and hydrochloric acid (HCl) solution. This is necessary for contacting the ground electrode.

Interdigitated electrodes (IDTs) of tantalum/platinum (10 nm/150 nm) were then patterned on the surface of the PZT by standard lift-off techniques. In this case, a surface-modification process was applied to obtain resist profiles having overhangs suitable for lift-off metallization [6.17].

The composite membranes were then released from the silicon substrate by anisotropically etching the backside of the silicon wafer in KOH, creating thus a V-groove frame supporting the freestanding acoustic delay line. During this step, a mechanical protection chuck was used to protect the PZT areas on the wafer top side.

This process is outlined in Figure 6.10, while Figure 6.11 shows each processing step.

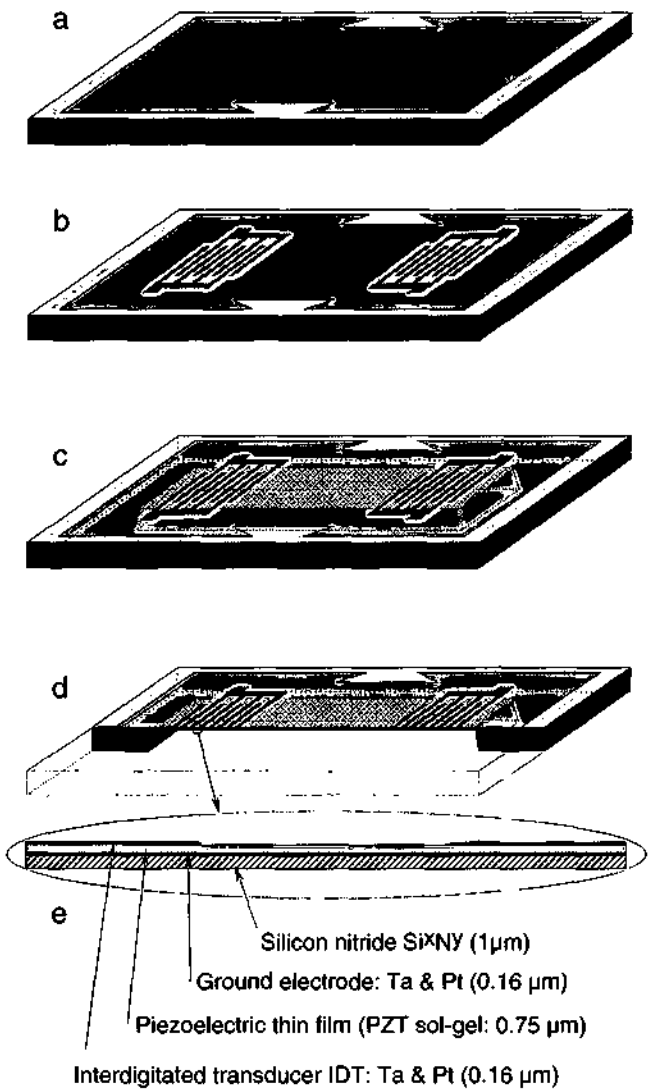

Figure 6.10: Fabrication sequence of the ultrasonic Lamb-wave actuator. (a) Patterning of the piezoelectric PZT thin film by a wet chemical etching. (b) Deposition of the top electrode (IDT) of Ta/Pt and structuring by lift-off technique. (c) Etching of the silicon wafer backside in KOH. (d) Cross-sectional view of the device. (e) Enlarged view of the cross section of the thin composite membrane.

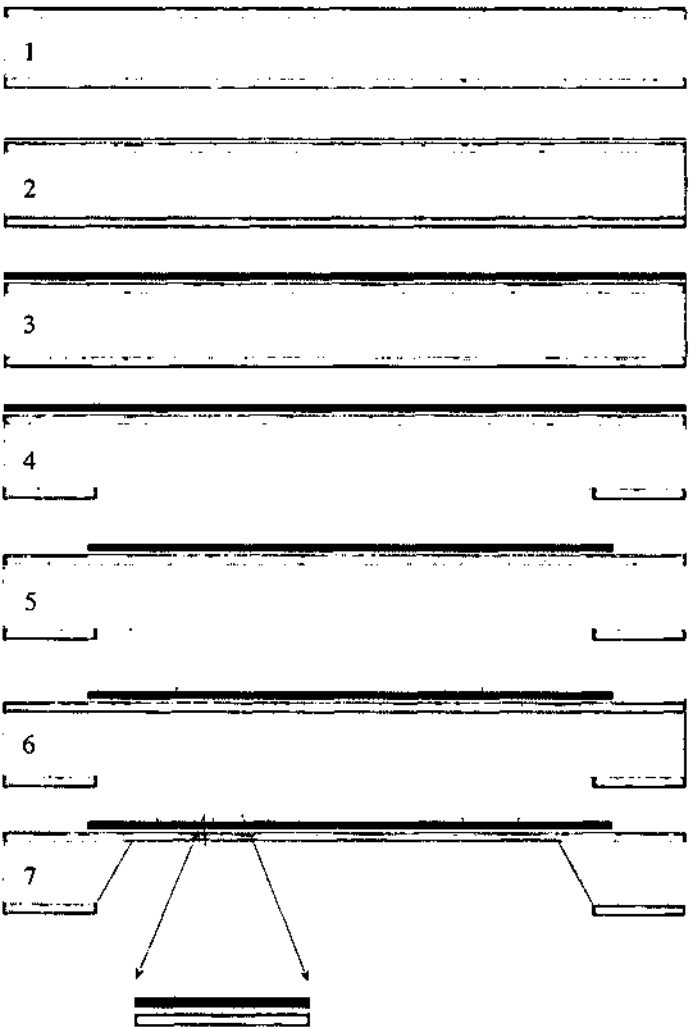

Figure 6.11: Main processing steps of the Lamb-wave fabrication. (1) Deposition of 1 μm LPCVD low stress silicon nitride Si_xN_y. (2) Tantalum/platinum ground plane metallization. (3) Deposition of the sol-gel derived piezoelectric PZT thin film. (4) Backside patterning: the silicon nitride is dry etched to form the windows for the KOH backside etching. (5) Wet chemical etching of the PZT layer. (6) Second metallization: the top IDTs electrodes are defined. (7) Membrane formation by anisotropic etching of the silicon. The silicon nitride provides an excellent etch stop.

It is to be noted, that the silicon nitride dry etch (step 4) can be done before or after the ground plane metallization and subsequent PZT deposition. Most of the wafers processed in this work have been directly metallized after the Si_xN_y deposition and then prepared for the sol-gel process.

Devices of the first generation were realized in the same way as for cantilever beams (cf. chapter 3), except the last step (top silicon dry etch, which is not necessary).

6.4 Thin film deposition and structuring

6.4.1 Low stress LPCVD silicon nitride thin film: the sandwich structure.

One of the key issues in Lamb-wave processing concerns the membrane building materials, their compatibility and selectivity through each fabrication step, and their ability to guarantee a resulting acoustically thin unsupported composite membrane having high mechanical strength. Layers involved for this purpose must be low in stress to prevent film delamination and curling of the final device. PZT and platinum thin films are very tensile and must therefore be deposited over a supporting layer having minimal residual tensile stress and stress gradient. For instance, the residual tensile stresses of a 1 μm thick PZT film deposited over a 0.1 μm thick platinum electrode are 200 MPa and 800 MPa respectively [6.18].

Fundamentally, the supporting layer is expected to overcome five major requirements.

(1) To enable the sol-gel deposition without being affected by it (chemically or thermally).

(2) To serve as a barrier layer against lead-silicon interdiffusion during the PZT formation.

(3) To compensate the residual stress of PZT/Pt films.

(4) To assure a mechanical stability of the entire membrane after having completely etched the underlying silicon.

(5) To allow the propagation of ultrasonic signals with efficiency, since compressive membranes with many crumpled areas are not satisfactory, the acoustic waves being strongly perturbed.

Plasma Enhanced Chemical Vapor Deposition (PECVD) is a very interesting alternative to deposit Si_3N_4 layers at low temperature, typically 350 °C. Films deposited by this technique depend strongly upon the process parameters [6.19]. The deposition rate is about 130 Å/min and the density varies between 2.4 g/cm^3 to 2.8g/cm^3. Unfortunately, PECVD films do not support further high temperature treatment, such as rapid thermal annealing at 650 °C involved during the PZT sol-gel processing. A series of Lamb-wave delay lines made with this supporting layer was strongly affected; most of the final suspended membranes were broken during the final silicon etching in KOH.

A good candidate is the stoichiometric LPCVD Si_3N_4 silicon nitride which offers many attractive characteristics (passivation of devices, high specific resistivity and good mechanical strength, excellent mask for the silicon wet etching in KOH with a etch rate less than 5 Å/hour), but possesses a high residual tensile stress, about 1000 MPa [6.20]. Slightly tensile resulting stress can be obtained when deposited over an SiO_2 thermal oxide layer having adequate thickness [6.21].

Low stress LPCVD Si_xN_y silicon-rich nitride is another very attractive solution [6.22], [6.23]. It is deposited in the same furnace as for standard LPCVD Si_3N_4 , but with a mixture of reactant gases SiH_2Cl_2 and NH_3 whose ratio, deposition temperature and flow rate are varied during the process. It has been used in many applications [6.6], [6.7], [6.24], [6.25], and possesses a residual tensile stress ten times smaller than Si_3N_4 [6.26].

In this work, a silicon-rich nitride layer placed between two LPCVD Si_3N_4 thin films was selected [6.27]. First a 400 Å thick LPCVD Si_3N_4 film is deposited over the silicon substrate, followed by a 0.92 μm thick silicon-rich nitride layer and a second 400 Å thick LPCVO Si_3N_4 film. The deposition rate is about 40 Å/min for Si_3N_4, and 70 Å/min for Si_xN_y.

The use of a Si_3N_4 film before and after the Si_xN_y deposition is motivated by the fact that silicon-rich nitride films have some pinholes, while a homogeneous deposition of Si_3N_4 at a rate of 40 Å/min allows a resulting film practically free of pinholes. Such composite silicon nitride configuration referred to here as a sandwich structure, is thus completely symmetric, permits a reduction of the tensile stress and provides an excellent mask and etch stop when used during very long silicon etching in KOH [6.28], [6.29].

Patterning of the silicon-rich nitride films is made by Reactive Ion Etching RIE. The Si_xN_y etch rate by RIE is about 450 Å/min. Like this, a relatively thick photoresist protection is required during the long etching time (about 22 min for 1 μm thick Si_xN_y). Hence, a positive photoresist AZ 4562 is spun at 500 rpm and 3000 rpm during 3 s and 40 s respectively, to achieve a thickness of 7.5 μm, and then patterned following standard photolithographic methods. It has to be noted, that a very precise alignment of the mask with respect to the wafer flat is required for this first photolithographic step, in order to minimize etching plane deviations during the KOH step (cf. 6.4.3).

During the RIE process, an organic deposition over the entire wafer area occurs and is difficult to remove, even with a standard cleaning using Caro's acid H_2SO_5 or "pirahna" procedure.

In our case, a proper wafer cleaning was simply performed manually using a mechanical friction between the wafer and a "Q-tips" during a few minutes in a recipient filled with acetone. Final cleaning was done with isopropanol and deionized water followed by a drying under nitrogen flow. Attempts to remove the photoresist by plasma O_2, KOH or formed procedures is possible only if no PZT layer is present on the wafer backside. PZT exhibits irreversible, severe deteriorations when submitted to these cleaning procedures without being correctly protected.

As a test of reliability and for practical fluidic applications, the membrane bending strength under hydrostatic pressure was tested with a former supporting layer covered by a 2000 Å thick platinum electrode. This additional Pt film replaces the PZT layer and considerably increases the tensile stress. For this test a wafer has been completely processed, but without PZT. Figure 12 depicts the experimental setup. One of the resulting membrane-based devices was placed over a Printed Circuit Board (PCB) support, the silicon recess being covered with a mechanical cap having an inlet and an outlet silicone tube. Water was slowly injected in the membrane cavity via a syringe and filled the outlet tube to generate a hydrostatic pressure. With this, it was possible to elevate the water level up to 1 m (0.1 bar) over the membrane without observing any damage. Such a simple experiment emphasizes the mechanical strength of micromachined membranes made from silicon-rich nitride layers.

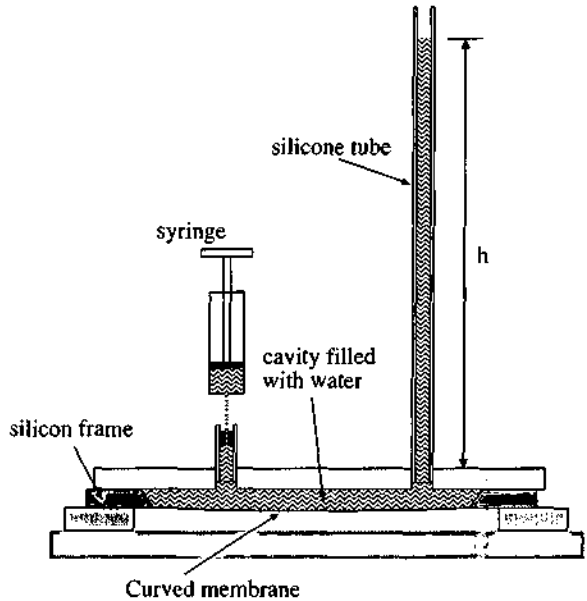

Figure 6.12: Schematic view of a membrane under test. With a syringe, the silicon V-groove is water filled and the liquid pushed into the tube up to h=1m.

6.4.2 Sol-gel PZT thin films structuring.

Two different PZT thicknesses (0.75 μm and 1.4 μm) have been successfully used for Lamb-wave devices of the second design generation, and each sol-gel deposition was performed according to the same description presented in chapter 2. In both cases, the resulting film was of the morphotropic phase boundary composition (mixed rhombohedral/tetragonal) $Pb(Zr_{0.53}Ti_{0.47})O_3$. The PZT areas not destined to be etched were protected by a 1.9 μm thick positive photoresist (AZ 1518) after a standard photolithgraphy. Patterning of the PZT layers was done in a way similar as that used for the cantilever beams (cf. chapter 3), in a $BHF:HCl:H_2O$ solution of concentration 1:2:9.

The etch time depends strongly on the PZT thickness. For a 0.7 μm thick PZT, 135 s are necessary to completely remove the film over the platinum electtode, while this time increases to 185 s for the 1.4 μm thick PZT layer. Residual Pb films are eliminated by rinsing the wafer in deionized water for at least 15 minutes. A comparison of the etching results is shown in Figure 6.13. Films of 0.7 μm and 1.4 μm thickness are on the left and right parts respectively. The AZ 1518 mask protection still remains over the PZT areas in order to observe the under etch, and each picture is presented at the same magnification. The PZT film of 0.7 μm thickness exhibits a small under etch of 2 or 3 μm width and a sharp profile, while the thicker film of 1.4 μm suffers a very large under etch with a poorly resolved profile. This is probably due to the fact that the three elements Pb, Zr and Ti of PZT etch at different rates [6.30], a long etch time thus increasing their relative effects.

In a general manner, it has been observed that PZT thin films with thickness varying from 0.2 μm to 0.8 μm present a better surface homogeneity, a more sharply define border and less roughness than other thicker films. An example of a very smooth film is shown in Figure 6.14 and Figure 6.15.

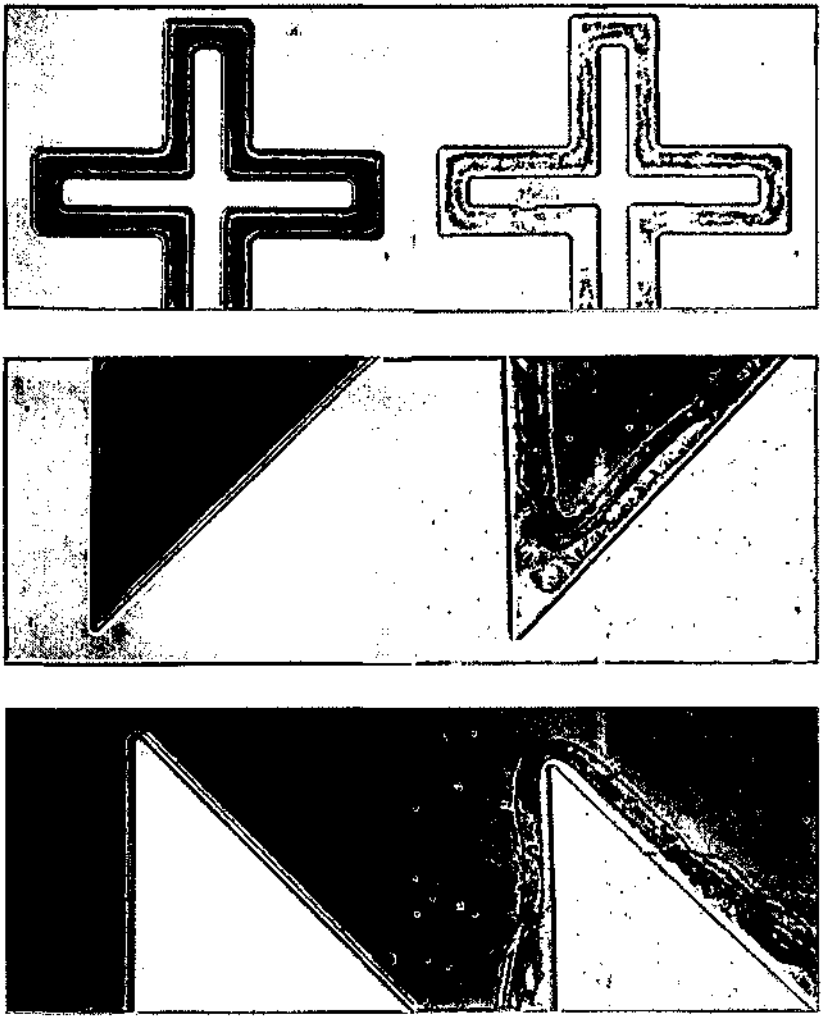

Figure 6.13: Optical views of PZT film areas obtained after a wet chemical etching in an ammonium fluoride etchant (BHF) and hydrochloric acid (HCl) solution. The mask protection (positive photoresist) is still present. Film of 0.7 μm thickness (on the left part) shows negligible under etch and precise border after 135 s of etching. In contrast, the thicker film (on the right part) with 1.4 μm PZT suffers very large under etch and a worse profile resolution, after 185 s of etching.

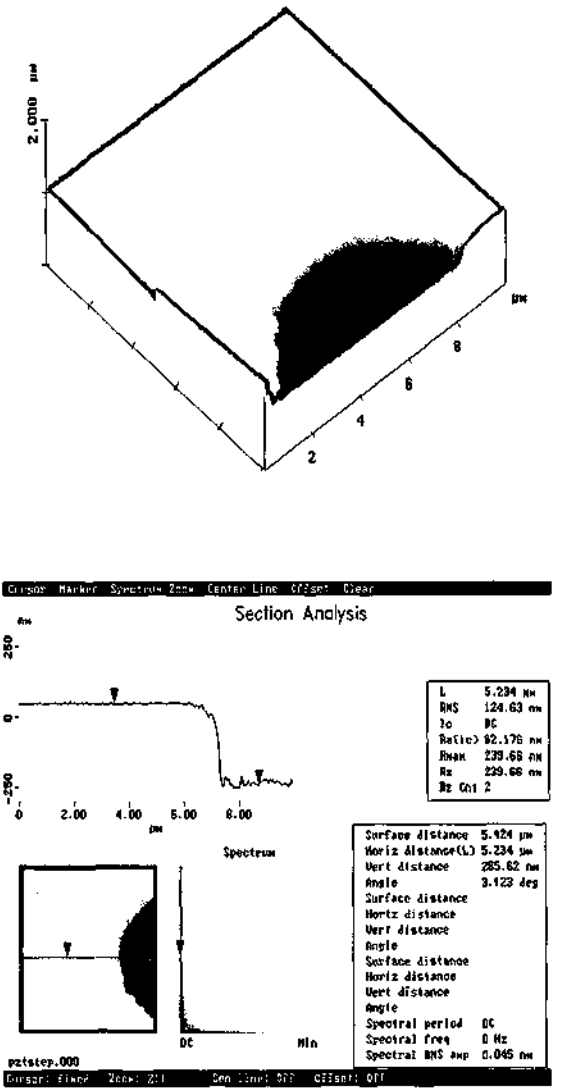

Figure 6.14: AFM topography of a PZT sample deposited over a platinum electrode. The PZT film is 0.28 µm thick and is partially etched on the right part of the picture. The etch time was 40 s. Some small irregularities are visible on the platinum layer and are probably related to the PZT etching process.

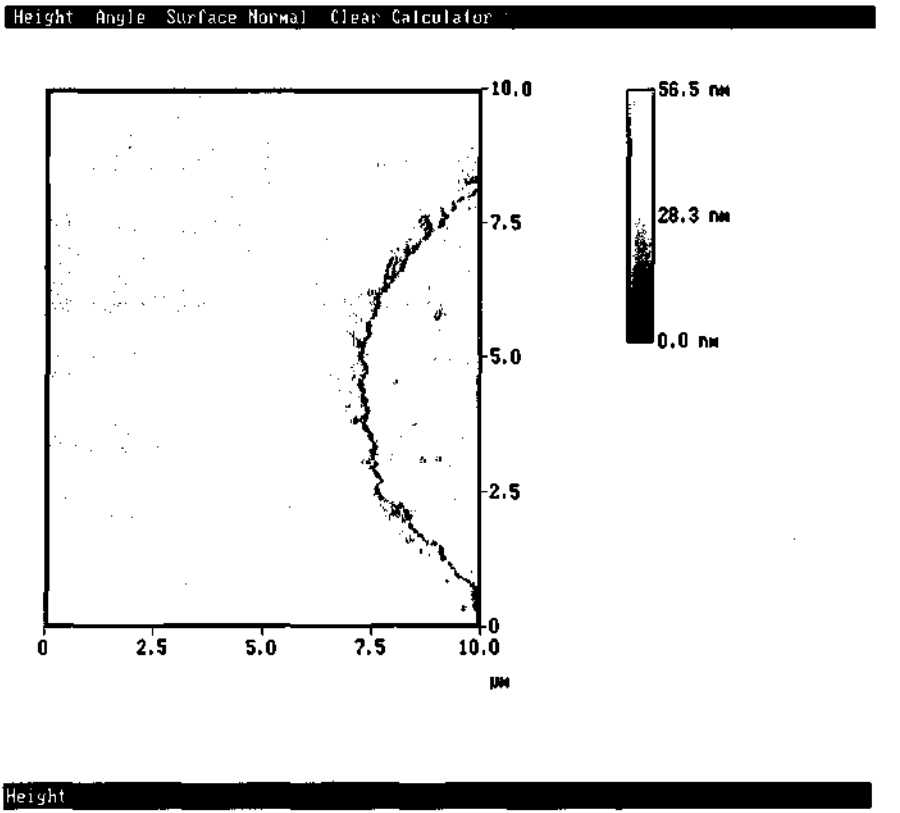

Figure 6.15: AFM top view of the same partially etched PZT area. For such a thin film, a sharply defined edge was achieved with a width of less than 2 µm.

Details of the PZT surface topography are presented in Figure 6.16. The estimated average surface roughness is 5 nm.

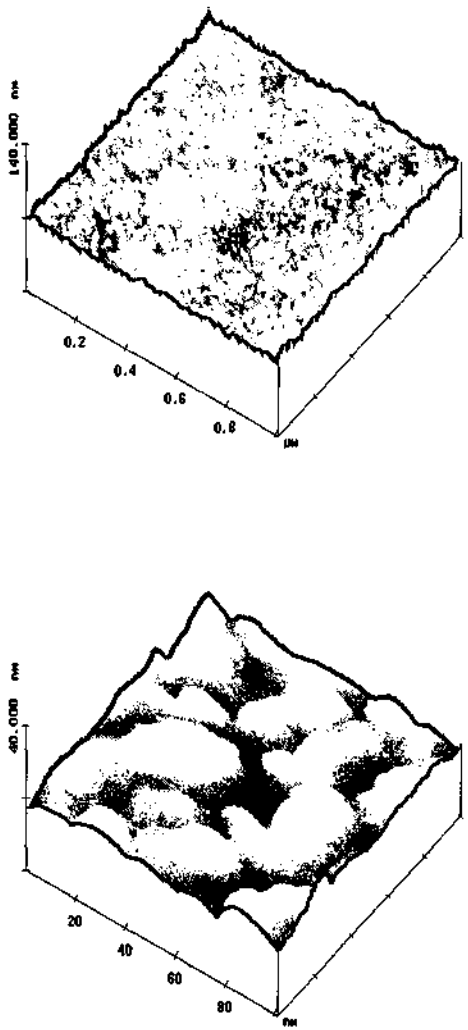

Figure 6.16: AFM imaging of nanoscale PZT topology for a 0.28 μm thick film. The microstructure is isotropic over a large scale and emphasize a polycrystalline state. The mean grain size of about 20 nm is observed.

6.5 Membrane single-sided processing by wet etching

Wet chemical anisotropic etching with KOH is the most common method employed in silicon membrane-based device microstucturing. A one-sided etching technique allows the partial or complete selective removal of the backside silicon areas directly exposed to the etcbing solution, while the other side and the wafer edges are carefully protected in a mechanical O-ring chuck. The main differences between cantilevers and FPW membranes single-sided processing are the etch-stop and the considerable increased fabrication difficulty.

In the case of cantilever structuring, the silicon was not completely etched, a residual silicon plate of about 15 μm thickness being preserved after an estimated average etch time (cf. chapter 3). With such a thickness, the probability of the plate cracking is negligible and the wafer can be easily removed from the chuck. Only a slight risk persists if the wafer presents some inherent defects (e.g. cracks) which will perhaps be a source of process failure. In other words, a KOH step is thus a practical way to simply thin selected backside areas, before the final patterning of cantilevers on the reverse side by a silicon reactive ion etching method. The dimensions of cantilever beams (width and length) depend therefore only on the photolithographic accuracy before RIE and not on the silicon thickness.

For FPW membranes, in spite of a complete silicon etching which provides an excellent thickness uniformity over the entire wafer, problems arise due to the membrane thinness. Residual stress and pressure between the wafer and the protection chuck become an important origin of membrane rupture. Other difficulties concern the precision of anisotropic etching. It is well known that several effects limit the accuracy of KOH-etching and thus cause different membrane sizes [6.2]. In our case, considering the process and the wafer specifications, four of those effects are: the lithography precision

(± 2 μm), the thickness variation (± 7 μm) and taper (± 3 μm), the misorientation of the surface and the misorientation of the flat.

Preparation of the wafer before the long KOH step is essential and was done according to the following. A positive photoresist (AZ 1518) layer is spun over the entire sensitive PZT/platinum area and dried at 80 °C for 45 min. This layer provides a soft contact between the wafer and the plexiglass cap and will allow a temporary reduction of KOH diffusion over the structures in the case of an eventual membrane break. The wafer is then placed in a home-built chuck protection providing a rubber O-ring seal on each side of the wafer and heated up to 60 °C in a convection oven. After a final tightening of the screws at this temperature (to minimize both thermally and mechanically induced stress gradients due to the applied pressure on the wafer), the chuck is immersed in the KOH etching solution.

A natural final etch stop is provided by the silicon nitride Si_3N_4. Based on an average silicon etching rate of 16.5 μm/hour of a (100) plane in a 40 % KOH solution at 60 °C, the total etch time is about 23 hours for a 380 μm thick wafer. A 30 minutes prolongation is often required to assure that each membrane area has been completely formed. This does not significantly affect the final shape of the structures, but removes possible silicon residues due to temperature inhomogeneities in the KOH solution. At last, the mechanical chuck is rinsed for a long time (30 min) in flowing water and carefully opened in a small water filled receptacle.

Examples of the final KOH processed membranes are shown in Figure 6.17. Detail of a membrane corner with an etch-stop over the silicon nitride layer is presented in Figure 6.18.

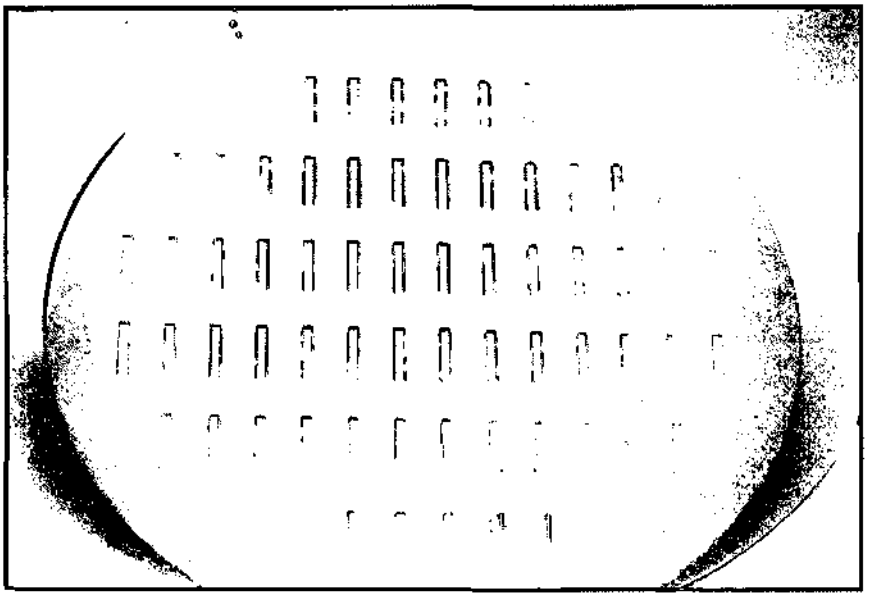

Figure 6.17: Four inch wafer-test with 64 suspended membranes processed after 23 hours in KOH. Each membrane is 1 mm wide and 8 mm long.

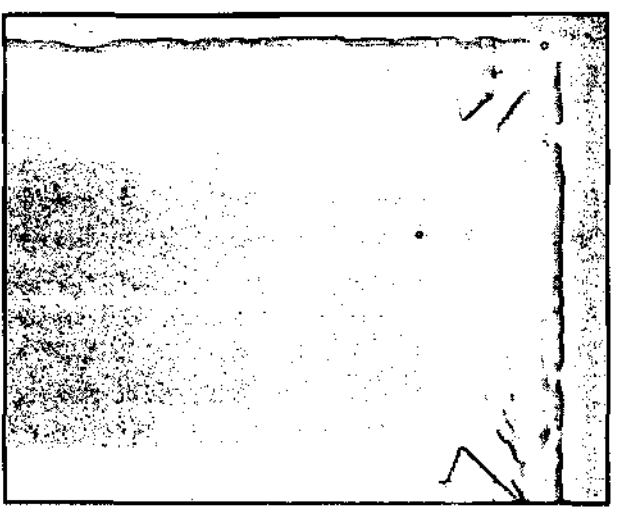

Figure 6.18: Magnified view of membrane corners after a final KOH etch stop over the silicon nitride film.

Several wafers processed like this suffered a membrane break just before the completion of the silicon etching. A quick chuck opening in flowing water permitted sometimes to limit the KOH penetration and to preserve almost 50 % of the devices. Much better results were obtained by stopping the etch earlier in order to keep a thin silicon plate a few μm thick, typically 10 μm, and to allow a more safe wafer handling. After rinsing and drying, the wafer was then placed face down horizontally on a flat ring and each recess manually filled with KOH using a pipette. Based on an etching rate of 1.2 μm/h for a ⟨100⟩ plane in KOH at 20 °C, a total silicon etch is thus obtained after a few hours. Although this setup extends the fabrication, it enables one to guarantee a total silicon etch, without the risk of membrane rupture due to the presence of a mechanical chuck. This technique can be improved by using siloxane-based sealing rings [6.31], a kind of low-stress chuck etch setup which considerably reduces the stress on the wafer. Other possibility involves a mechanical chuck constructed with two teflon parts which allows a nitrogen flow to remove etchant penetration [6.32].

6.6 Processing of ultra thin plates with arbitrary geometric shapes

In most applications involving membrane processing technology, the silicon areas on the wafer back side are chemically wet etched in a solution of potassium hydroxide (KOH). This relatively simple method allows the microfabrication of high quality residual membranes with well controlled thickness. However, three major disadvantages are encountered. First, many layers are not compatible with KOH and must be protected during this step. This is dramatically the case, when a ferroelectric thin film like lead zirconate titanate (PZT) is present on the top side of the wafer. A mechanical protection chuck is then required. Secondly, with the chuck protection, very thin membranes (less than two micrometers thick) having large areas are difficult

to fabricate, due to residual pressure between the membrane and the mechanical protection. In particular, multilayered membranes composed of layers subjected to in-plane tension such as silicon nitride, platinum and PZT thin films, are very sensitive to any small stress gradient between the chuck and the silicon frame. KOH contamination of all of the wafer surface due to one membrane breaking, increases the difficulty of this process. Thirdly, only simple geometrical shapes (squares or rectangles) are generally processed. Polygonal, elliptical or arbitrary shapes are not easy to prepare.

During this work, the possibility of using Advanced Deep Reactive Ion Etching (ADRIE) technology from STS, to process very thin composite plates with large areas over a 400 μm thick wafer has been tested [6.33]. A 0.45 μm thick silicon dioxide (SiO_2) layer is first thermally grown on both sides of the four inch wafer, followed by the plasma-enhanced chemical vapor deposition (PECVD) of a 0.6 μm thick low stress silicon nitride (Si_xN_y) layer on one side. A Ta//Pt (10 nm/150 nm) metal ground plane is then evaporated over the Si_xN_y layer. The membrane pattern is defined by a photolithographic step using an 8 μm thick positive resist. The silicon nitride is etched by dry etching while the silicon oxide is removed by wet chemical etching in a solution of buffered hydrofluoric acid (BHF). In our case, principally rectangular membranes were tested with two different sizes: 1x8mm and 2x8mm. Other small test structures having arbitrary shapes were performed. After 88 min mean time of silicon etching by the ADRIE technique, a selective etch stop is provided by the SiO_2 underlying layer which is then wet etched. Figure 6.19 shows final composite suspended membranes having only 0.76 μm thickness. On the left part, two of them are broken. In Figure 6.20, a closer view of one broken membrane with right angle profile emphasizes the great potential of this technology. A close up view of a test structure having curled membrane edge is presented in Figure 6.21.

Figure 6.19: Photograph of four multilayer membranes (silicon nitride and platinum). Overall dimensions are 1 or 2 mm by 8 mm, while the thickness is 0.76 μm.

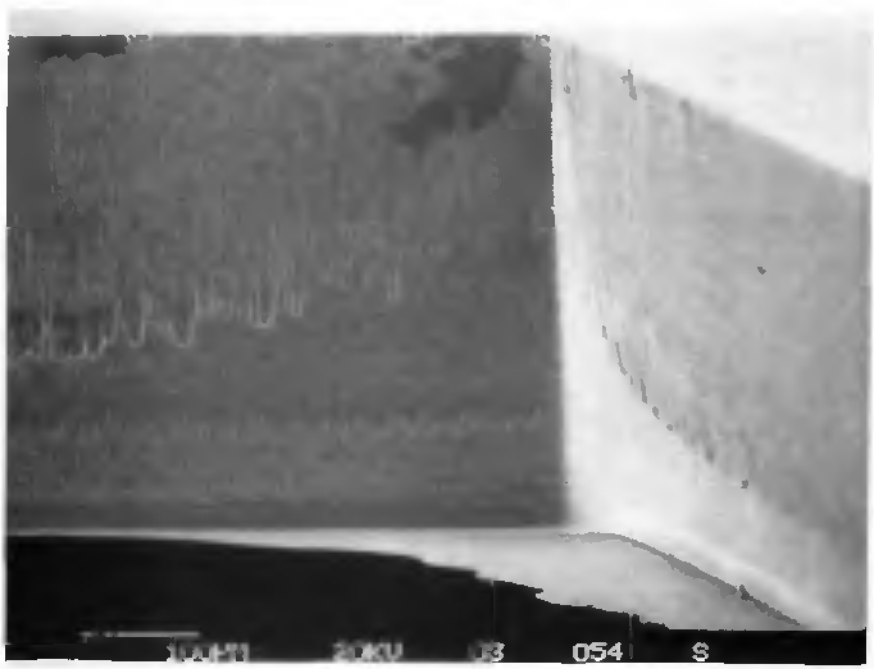

Figure 6.20: SEM close up of the vertical walls. The depth of the cavity is 400 μm. A remaining parts of a broken plate is visible on the bottom right.

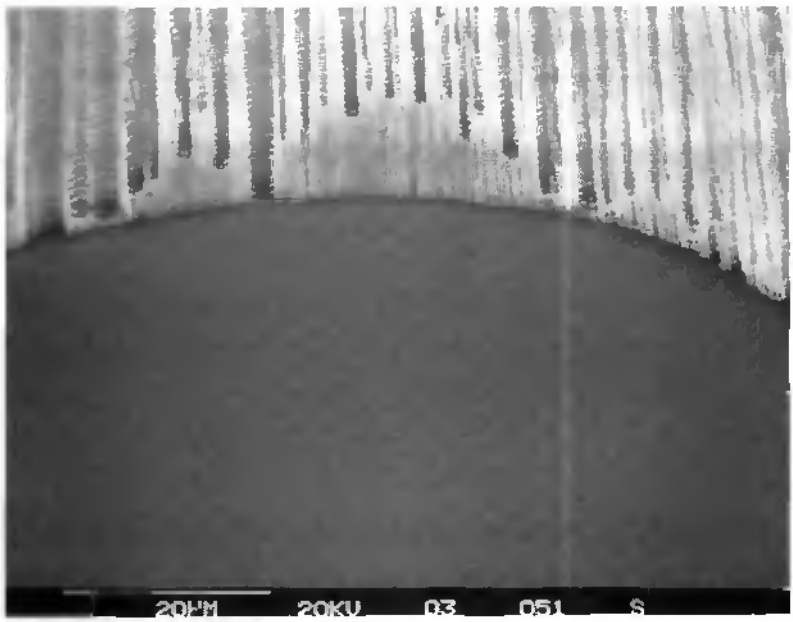

Figure 6.21: SEM details of a membrane edge with arbitrary shape.

6.7 Wafer dicing, die attach on PCB substrate and electrical connections.

Wafer sawing is a critical aspect of FPW device fabrication. In order to effectively protect each delay line during the silicon cutting, both sides of the wafer are covered with a thick photoresist layer. For this, the wafer is held vertically and fixed to a support using a teflon clip. Photoresist is then simply dispensed with a pipette and dried on this setup at room temperature during 24 hours to minimize mismatched thermal expansions between the device and the package: it thus plays the role of a soft package while the wafer is handled and sawed. It also protects the membrane from dust and other solid particles. After dicing, each structure is released in acetone and carefully cleaned in different baths containing acetone, isopropanol and deionized water, respectively.

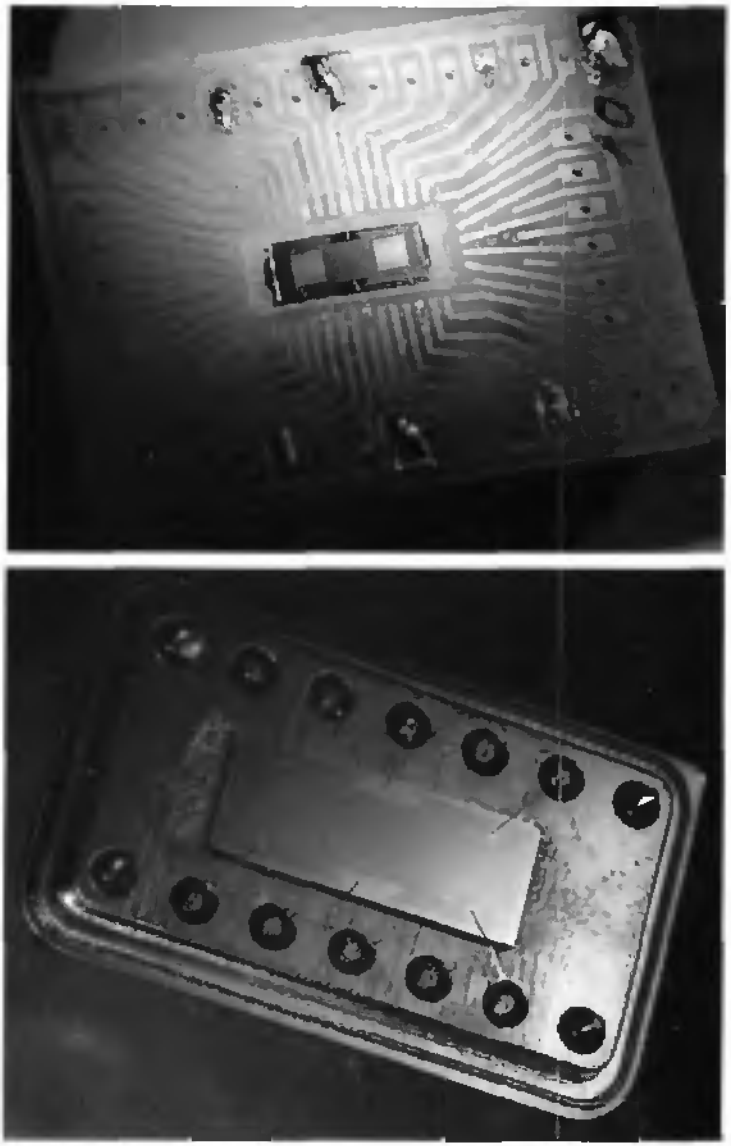

Figure 6.22: Optical views of final Lamb-wave devices. (Top): mounted over a PCB substrate. (Bottom): mounted over a standard DIL package. In both cases, aluminium wires are ultrasonically bonded to the contact pads of each IDTs transducers.

Most of the Lamb wave devices are individually mounted over a mother substrate, a commercial laminate material FR-4 (epoxy resin strengthened with glass fiber mats) with flat copper strips on the top side, by gluing the silicon frame structure on the PCB. Two glue points on the frame extremities enable a solid, stable device fixation (this is necessary for ultrasonic wire bonding) and a small residual compressive stress in the membrane. Attempts to completely glue the frame area generates large compressive stresses in the silicon and results in a buckled membrane. Figure 6.22 (top) shows a final FPW delay line mounted over a PCB with 35 µm thick copper lines. The outside strip is connected to the ground electrode. Figure 6.22 (bottom) shows a same device mounted over a standard DIL package.

For a device mounted over a PCB, the access to the membrane backside is provided by a rectangular hole in the center of the substrate, and is presented in Figure 6.23.

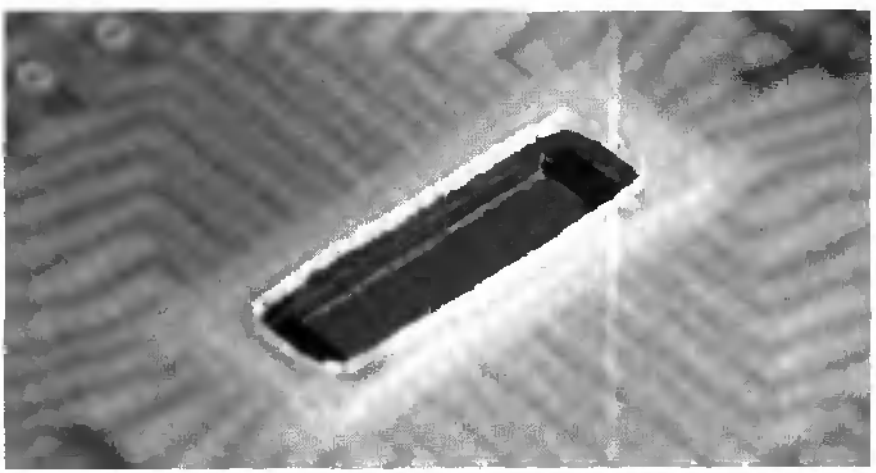

Figure 6.23: Optical view of the PCB backside. A rectangular hole enables to have a direct access to the membrane.

Connections between copper strips on PCB and transducer pads have been tried in three different ways: ultrasonic wire bonding, wire gluing and strip painting. Wire bonding is the most reliable method to contact electrically the IDTs. In the case of FPW devices, IDTs contact pads are directly placed on the PZT layer over the silicon bulk frame. It means that a short between bottom and IDT top electrodes can easily be done if the ultrasonic bonds are not properly performed. Precise settings (applied force, ultrasonic power and contact duration) of the bond apparatus is therefore required. Other difficulties can appear in the case of poor electrode adherence.

Some of the devices suffered a bad adherence of the IDTs Ta/Pt over the PZT film, and necessitated to be electrically connected with glued wires. For each connection, a thin copper wire was first soldered to the substrate. Small glue bumps were deposited over the IDTs pad areas. The glue is an electrically conductive, silver filled epoxy paste with two components, (Epo-Tek E 4110 from Epoxy Technology). Then, the extremity of each copper wire was carefully dipped in the glue bump, and the complete device cured at 100 °C for one hour in a convection oven. Figure 6.24 shows a structure connected with this method.

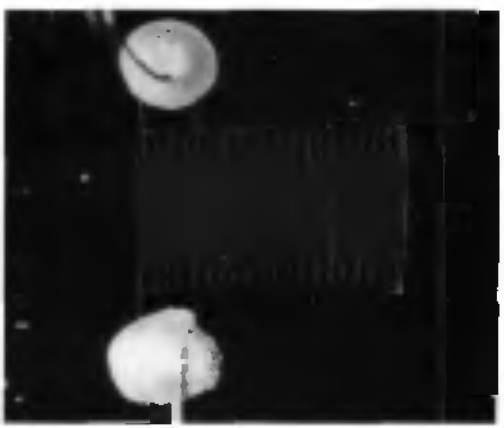

Figure 6.24: Optical view of a FPW device having its electrical wire connections glued on the contact pads.

Strip painting is an easier and quicker way to connect the IDTs. Prior to the painting, a silicone rubber is locally applied over the ground electrode to avoid short circuits. Then the conductive strip is formed using a thin sharp syringe tip and the same former noted epoxy paste. Figure 6.25 exhibits such a contact.

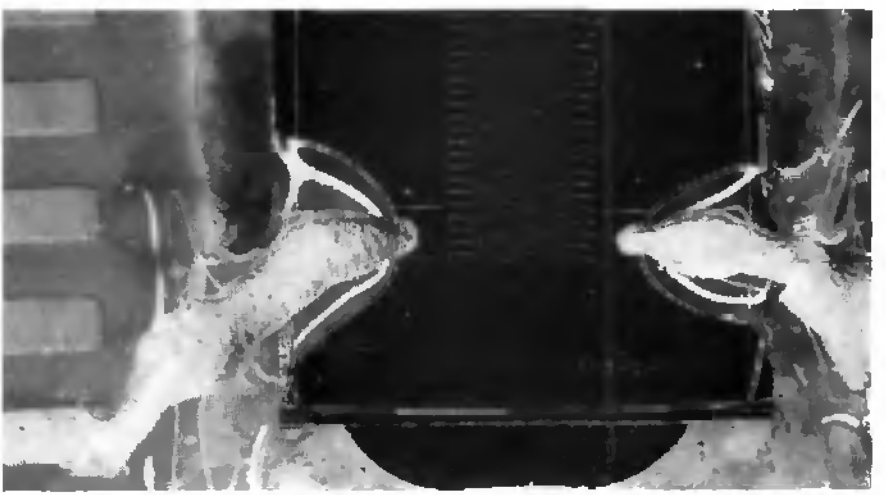

Figure 6.25: Optical view of a FPW device having its electrical wire connections painted on the silicone rubber.

6.8 References

[6.1] K. E. Peterson, "Silicon as a mechanical material," *IEEE Proc.* **70**, 420 (1982).

[6.2] W. Lang, "Silicon microstructuring technology", Materials Science and Engineering, R17 (1996) 1-55.

[6.3] H. Seidel, L. Csepregi, A. Heuberger and H. Baumgärtel, *J. of Electrochem. Soc.*, **137** (1990) 3612-3626.

[6.4] C. Linder, T. Tschan, and N. F. de Rooij, "Deep dry etching techniques as a new IC compatible tool for silicon micromachining," in 1992 *Int. Conf. Solid-State Sensors Actuators (Transducers '91)*, p. 524.

[6.5] C. Linder, L. Paratte, M.-A. Grétillat, V. P. Jaecklin and N. F. de Rooij, "Surface micromachining", *J. Micromech. Microeng.* **2** (1992) 122-132.

[6.6] S. M. Sze "Semiconductor sensors", New York, John Wiley & Sons, Inc. 1994, ch. 2.

[6.7] A. D. Roming Jr. and J. H. Smith, "The coming revolution in ICs: intelligent, integrated microsystems", *Micromachined Devices*, Vol.3 N°2, February 1998, pp. 4-6.

[6.8] D. S. Ballantine, R. M. White, S. J. Martin, A. J. Ricco, E. T. Zellers, G. C. Frye, H. Wohltjen, "Acoustic Wave Sensors: Theory, Design, and Physico-Chemical Applications", San Diego, Academic Press Inc. 1997, ch.3.

[6.9] R. L. Smith and S. D. Collins, "Micromachined Packaging for Chemical Microsensors", *IEEE Trans. Electron Devices*, vol. 35, no. 6, pp. 787-792, June 1988.

[6.10] S. Middelhoek, A. A. Bellekom, U. Dauderstädt, P. J. French, S. R. Hout, W. Kindt, F. Riedijk, and M. J. Vellekoop, "Silicon Sensors", Meas. Sci. Technol. **6** (1995) 1641-1658.

[6.11] M. Feldmann and J.Hénaff, " Surface Acoustic Waves For Signal Processing", Boston, Artech House, 1989.

[6.12] C. Campbell, "Surface Acoustic Wave Devices and Their Signal Processing Applications", London, Academic Press Inc. 1989, ch. 6.

[6.13] C. S. Hartmann, P. V. Wright, R. J. Kansy and E. M. Gerber, "An analysis of SAW interdigital transducers with internal reflections and the application to the design of single-phase unidirectional transducers," *Proc. 1982 IEEE Ultrasonics Symp.*, pp. 40-45, 1982.

[6.14] A. J. de Vries, R.L. Miller and T. J. Wojcik, "Reflection of a surface wave from three types of 1D transducers," *Proc. IEEE 1972 Ultrasonics Symp.*, pp. 353-358, 1972.

[6.15] E. Dieulesaint, D. Royer, "Ondes élastiques dans les solides. Applications au traitement du signal". Masson et Cie, Paris 1974, ch. 7.

[6.16] R. M. Moroney, R. M. White, and R. T. Howe, "Ultrasonically Induced Microtransport", *Appl. Phys. Lett.* **59**, 774-6 (1991).

[6.17] M. Hatzakis, B. J. Canavello, and J. M. Shaw, "Single-Step Optical Lift-Off Process", *IBM J. Res. Develop.*, Vol. 24, No 4, July 1980.

[6.18] A. Prodromides, A. Seifert, "Etude des contraintes dans des films minces de $PbZr_xTi_{1-x}O_3$ en vue de l'utilisation de ses propriétés piézoélectriques", Sommer stage report 1997, Swiss Federal Institute of Technology, EPFL, Laboratoire de Céramiques MX-D Ecublens, CH-1015 Lausanne, Switzerland. (Unpublisched).

[6.19] A. Stoffel, A. Kovacs, W. Kronast, and B. Müller, "LPCVD against PECVD for micromechanical applications", *J. Micromech. Microeng.* **6** (1996), pp. 1-13.

[6.20] S. M. Sze, "VLSI Technology", McGraw-Hill Internationational Editions, New York 1988, pp. 262-263.

[6.21] P. Muralt, M. Kohli, T. Maeder, A. Kholkin, K. Brooks, N. Setter, and R. Luthier, "Fabrication and characterization of PZT thin-film vibrators for micromotors", *Sensors and Actuators* A 48 (1995) 1577-165.

[6.22] M. Sekimoto, H. Yoshihara, and T. Ohkubo, " Silicon nitride single-layer x-ray mask", *J. Vac. Sci. Technol.*, 21(4), 1017-21, Nov./Dec. 1982.

[6.23] P. French. R. Wolffenbuttel, R. Mallee, and P. Sarro, "Optimization of a low stress silicon nitride process for surface micromachining applications", *Eurosensors' 94*, p. 205.

[6.24] A. Folch, M. S. Wrighton, and M. A. Schmidt, "Microfabrication of Oxidation-Sharpened Silicon Tips on Silicon Nitride Cantilevers for Atomic Force Microscopy", *Journal of Microelectromechanical Systems*, Vol. 6, No. 4, 303-306, December 1997.

[6.25] R. A. Steward, J. Kim, E. S. Kim, R. M. White, and R. S. Muller, "Young's modulus and residual stress of LPCVD silicon-rich silicon nitride determined from membrane deflection", Sensors Mater. **2** (1991), 285-98.

[6.26] L. Lin, A. P. Pisano, and R. T. Howe, "A Micro Strain Gauge with Mechanical Amplifier", *Journal of Microelectromechanical Systems*, Vol. 6, No. 4, December 1997.

[6.27] C. Beuret, G.-A. Racine, "Méthode de déposition de couches minces piézoélectriques pour actuateurs intégrés", Semester work, University of Neuchâtel, Institute of Microtechnology, 1992. (Unpublisched).

[6.28] G. A. Racine, R. A. Buser, N. F. de Rooij, G. Stucki, R. Stucki, and K. Pretzl, "Low-temperature Operating Silicon Bolometers for Nuclear Radiation Detection", *Sensors and Actuators*, A21-A23 (1990) 478-481.

[6.29] C. Beuret, Ph. Niedermann, U. Staufer and N. F. de Rooij, "Fabrication of metallic probes by a new technology based on double molding", *Microelectronic Engineering*. 41/42 (1998) 543-546.

[6.30] S. Mancha, "Chemical etching of thin PLZT", *Ferroelectrics*, 1992, Vol. 135, pp. 131-137.

[6.31] J. Brugger, G. Beljakovic, M. Depont, H. Biebuyck, N. F. de Rooij, and P. Vettiger, "High-yield wafer chuck for single-sided wet etching of MEMS structures",

International Conference on Solid-State Sensors and Actuators,Transducers'97, Chicago, June 16-19, 1997, Digest of Technical Papers, Volume 1, pp. 711-713.

[6.32] J. T. Kung, A. N. Karanicolas, and H.-S. Lee, "A compact, inexpensive apparatus for one-sided etching in KOH and HF", *Sensors and Actuators* A, 29 (1991) 209-215.

[6.33] P.-A. Clerc, L. Dellmann, F. Grétillat, M.-A. Grétillat, P.-F. Indermühle, S. Jeanneret, M. Koudelka, Ph. Luginbuhl, C. Marxer, T. Pfeffer, G.-A. Racine, S. Roth, P.Thiébaud, and N. F. de Rooij, "Advanced Deep Reactive Ion Etching a Versatile Tool for Micro-Electromechanical Systems", accepted for publication in *Journal of Micromechanics and Microengineering*.

7. Experimental results

7.1 Introduction

A very thin suspended membrane along which acoustic waves are generated and detected, surrounded by a solid thick silicon frame, is the key component of a so called Lamb-wave sensor and/or actuator. Any external perturbations that induce a variation of the synchronous frequency, can be investigated, e.g. temperature, pressure, added mass, electric field, shock, phase transition, etc., and an accurate device selectivity is therefore necessary. On the other hand, the acoustic power carried by progressive waves can be used to move solid particles or liquids in contact with the membrane.

This duality of micromachined Lamb-wave devices allows many experiments to be performed. Furthermore, the device configuration enables access to either side of the suspended membrane.

This chapter is essentially based on various experimental results that are presented in [7.1], [7.2] and [7.3], and highlights the great potential of ultrasonic Lamb-wave devices.

7.2 Piezoelectric thin film capacitor characterization

7.2.1 Measurement of the relative dielectric permittivity ε_r for various PZT films

The potential electrostatic energy stored in a PZT thin film capacitor is given by:

$$E_{pot} = \frac{1}{2} C V^2 \qquad (7.1)$$

where C is the PZT capacitance and V the potential. The capacitance of a parallel plate capacitor is:

$$C = \varepsilon_{PZT} \frac{S}{d} = \varepsilon_r \varepsilon_0 \frac{S}{d} \qquad (7.2)$$

where ε_{PZT} is the dielectric permittivity of PZT, S the plate area, d the PZT film thickness, ε_r the relative dielectric permittivity of PZT, and ε_0 the permittivity in vacuum.

For the generation of piezoelectric acoustic waves, the energy remaining E^*_{pot} in the capacitor after emission of depolarization waves is [7.1]:

$$E^*_{pot} = \left(1 - K^2\right) E_{pot} \qquad (7.3)$$

where K^2 is the electromechanical coupling factor. Hence, the efficiency of the device to launch acoustic waves depends essentially on the K^2 factor and on the stored energy, which is proportional to ε_{PZT} . (Other factors like the IDT geometry, mode conversion, are not considered here for simplicity). The

capacitor impedance, or more precisely its capacitive reactance X_c as a function of the circular frequency ω has the form of:

$$X_c = \frac{1}{\omega C} \qquad (7.4)$$

Hence, with formula (7.2) and (7.4), the capacitive reactance is given by:

$$X_c = \frac{1}{\varepsilon_r \varepsilon_0} \frac{d}{\omega S} \qquad (7.5)$$

Practically, several capacitors having different areas were conceived and used as test structures (see Figure 7.1). The capacitive reactance X_c of each capacitor is measured at a frequency ω of 10 kHz. Then the different capacitances C are calculated from formula (7.4) and reported as a function of the plate areas. According to formula (7.2), the linear dependence between the capacitance C and the area S enables the relative dielectric permittivity ε_r of the PZT film to be extracted, as shown in Figure 7.2.

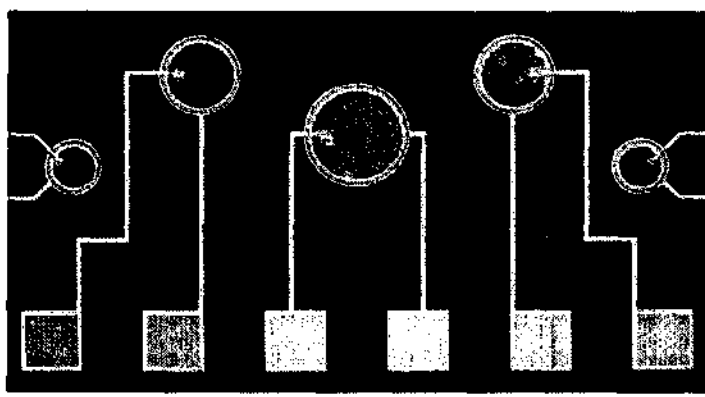

Figure 7.1: Optical view of micromachined plate capacitors for the characterization of the piezoelectric PZT thin film.

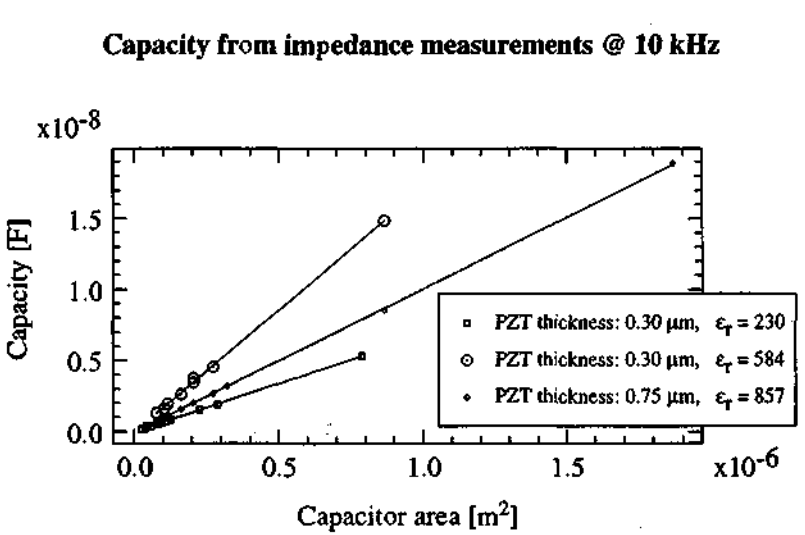

Figure 7.2: Experimental determination of the relative dielectric permittivity ϵ_r for various PZT thin films.

7.2.2 Loss factor and IDT impedance-phase versus frequency measure

For the generation of flexural waves, each comb of the IDT acts as a parallel plate capacitor filled with a PZT dielectric medium. Like every condenser, the PZT film capacitor is subject to a dielectric loss which represents the amount of energy absorbed in the medium due to the applied alternating voltage. The dielectric loss is defined by $tan\delta$, δ being the difference in phase between current and potential [7.1]. Figure 7.3 illustrates the measured loss factor and the impedance magnitude for a single comb of an IDT. Up to the synchronous frequency (near 3 MHz), the loss factor is less than 5%, and we observe that the impedance magnitude of the comb is largely capacitive up to a frequency of 10 MHz.

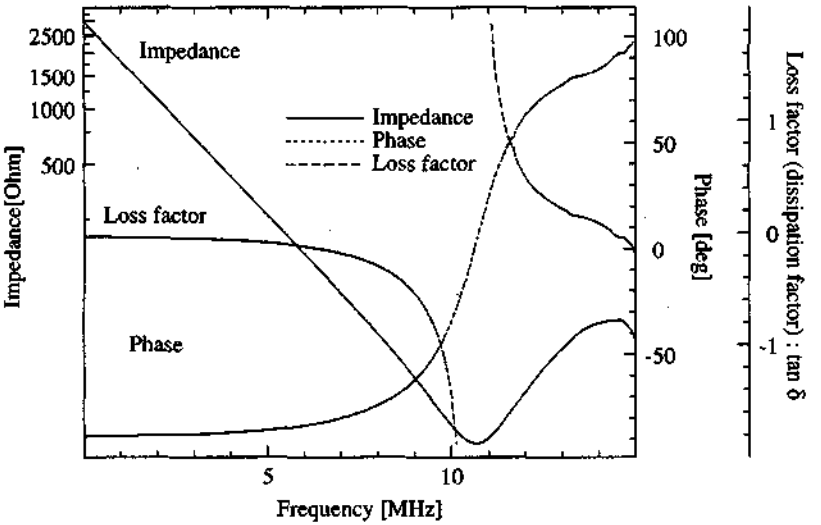

Figure 7.3: Measured impedance magnitude and loss factor of a single IDT comb. The PZT film thickness is 0.7 μm.

7.3 Measurement set-up and electrical connections

A printed circuit board, patterned over a 10 cm by 7 cm, 1 mm thick commercial laminate PCB, is used to easily connect the Lamb wave device to the HP network analyzer. This circuit enables to couple the input and output HP coaxial cables to the small mother substrate over which the Lamb wave device is already mounted (c.f. chapter 6, section 6.7).

Generation of progressive waves in the membrane, with maximal efficiency, is achieved by applying a bipolar excitation to the IDT emitter. The emitter transducer is thus driven differentially with respect to the ground plane.

Hence, a balun transformer (power splitter/combiner, PSCJ-2-1 from Mini-Circuit™) is placed between each IDT and its external coaxial connection. Figure 7.4 shows the design of the printed circuit.

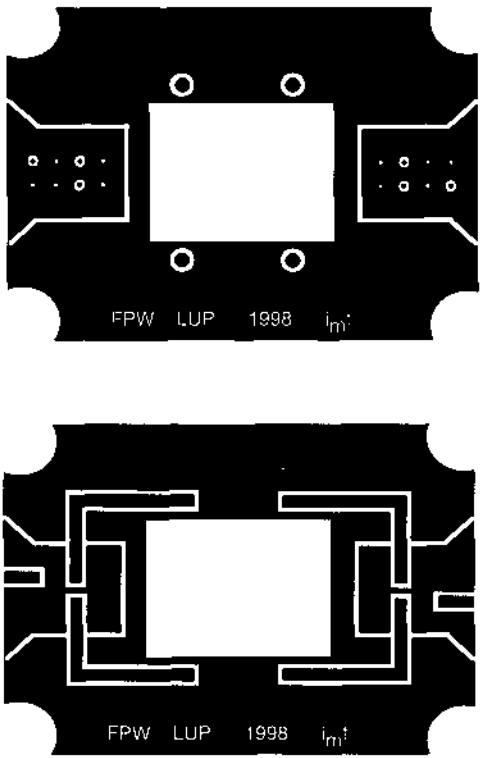

Figure 7.4: Schematic view of the double sided printed circuit board.

Figures 7.5 and 7.6 illustrate the experimental setup and its connections to the HP network analyzer, respectively.

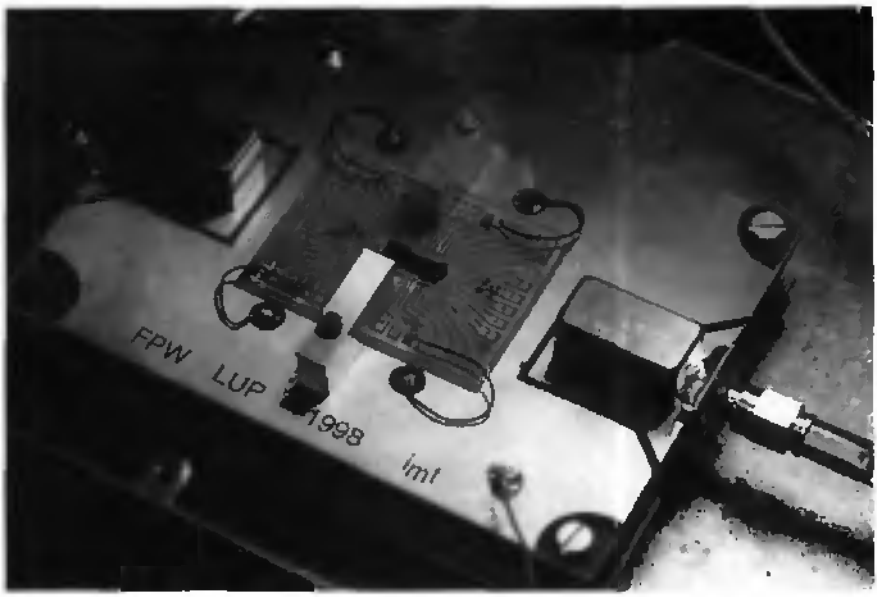

Figure 7.5: Optical view of the experimental setup. This configuration with two PCB levels, allow for stable device handling and minimal noise. An e.m. shield is placed between the contact lines of each balun, to suppress their direct capacitive coupling.

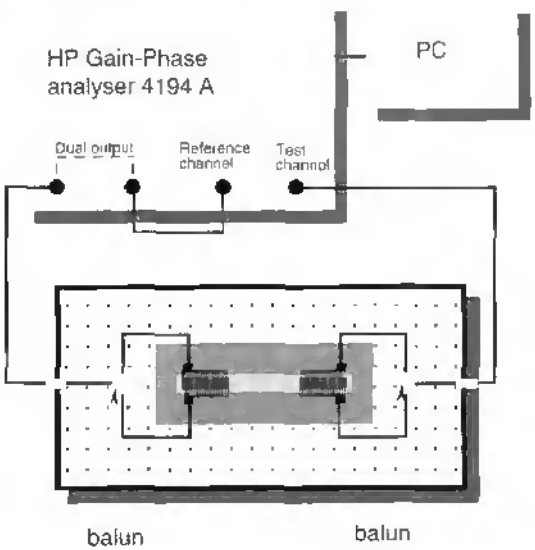

Figure 7.6: Schematic view of the setup used during frequency measurements.

7.4 Air-loaded FPW devices of the second generation

This paragraph deals with measurements performed on several Lamb wave devices belonging to the second generation, i.e. each structure was processed according to the fabrication sequence previously described in section 6.3. During the measurement, both sides of the membrane are in contact with air at atmospheric pressure.

7.4.1 Frequency responses

Propagating signals through the acoustic delay line are detected by observing the minimal insertion loss using the gain-phase analyzer. Figure 7.7 shows the frequency response of a device up to 80 MHz. As predicted by the theory of acoustic waves in plates with small thickness-to-wavelength ratios, only two modes propagate: the antisymmetric a_n and symmetric s_n modes. The lowest order a_0 (n=1) mode exhibits the highest detected signal. It is in accordance with the fact that flexural motions are predominantly generated when the IDT is driven at its fundamental synchronous frequency. At higher frequencies, the time constant of the IDT capacitor prevents a complete energy storage, and the electromechanical coupling constant K^2 may differ from that of the lowest order.

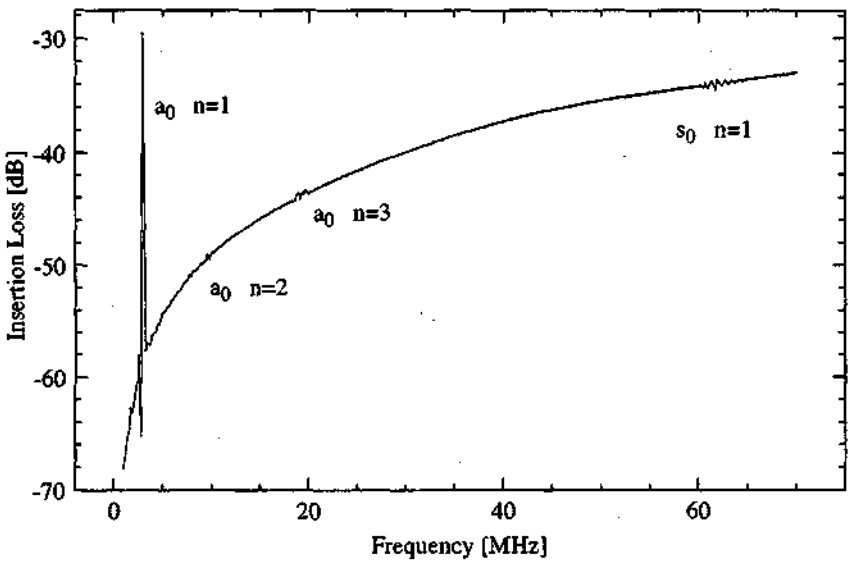

Figure 7.7: Measured frequency response of a FPW device. Fundamentally, the antisymmetric a_0 and symmetric s_0 modes are the only two modes that can propagate in a plate with small thickness-to-wavelength ratio. Here, the a_0 mode is detected with its two lowest harmonics: the even (n=2) and the odd (n=3). The lowest symmetric mode s_0 (n=1) appears at a frequency near 60 MHz.

In Figure 7.8, a narrowband frequency sweep emphasizes two main signals (approximately at 2.9 MHz and 3.1 MHz) with multiple peaks. These two main signals are due to destructive interferences between forward and backward emitted waves (bidirectionality of the IDT and edge reflection, c.f. section 7.4.8). The multiple peaks (jaggedness of the passband) are produced by cross talk and triple-transit-interferences (see section 7.4.18). Despite the fact that destructive interferences reduce the acoustic amplitude, a propagating wave is detected with a gain up to 30 dB, which should greatly increase in the case of pure constructive interferences with the waves reflected at the edge.

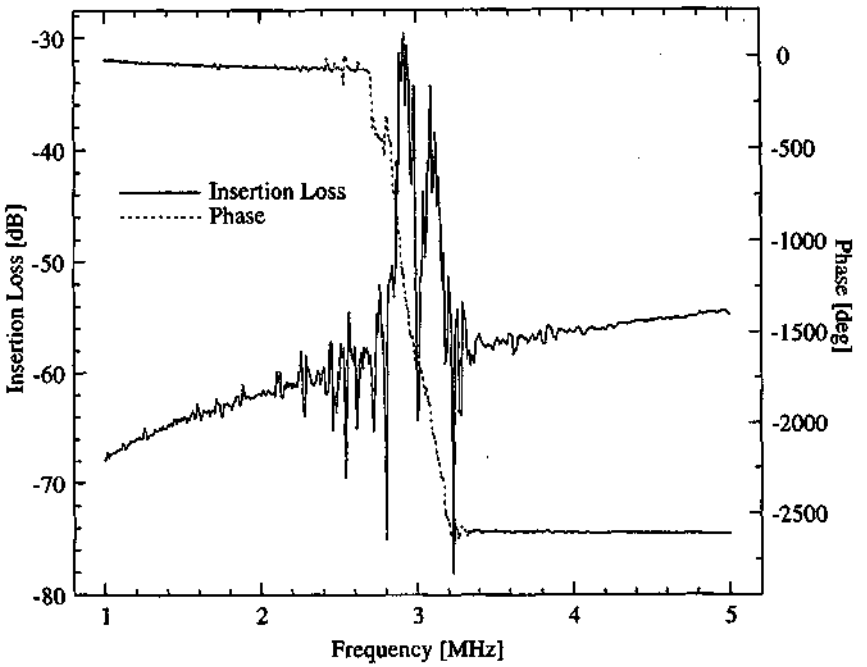

Figure 7.8: Narrow-band frequency sweep showing magnitude and phase around the passband of the a_0 (n=1) mode.

Instead of having only one main signal for the lowest order flexural mode a_0 (n=1), the edge reflection acts as an acoustic beam splitter which produces two frequency-separated signals. This characteristic also appears in the two harmonic a_0 (n=2) and a_0 (n=3) modes. In Figure 7.9, the weakly detected even harmonic (n=2) is visible with its two distinct beams, approximately at 8 MHz and 9.5 MHz. The odd harmonic (n=3) is slightly stronger than the even one, yielding two signals at 18.7 MHz and 19.7 MHz, respectively (c.f. Figure 7.10).

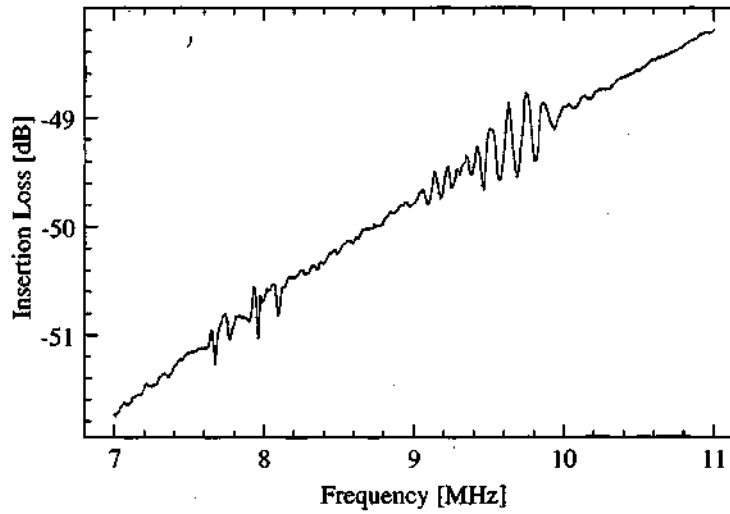

Figure 7.9: Narrow-band frequency response showing an even harmonic (n=2) of the flexural a_0 mode.

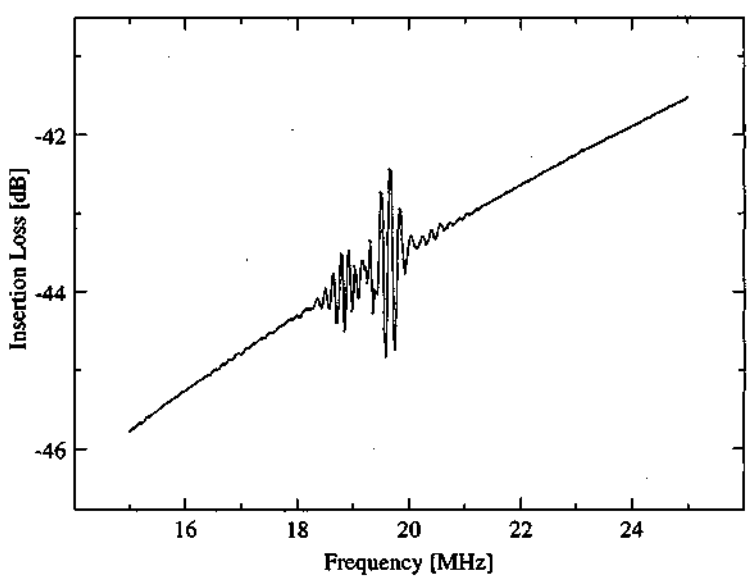

Figure 7.10: Narrow-band frequency response around the odd harmonic (n=3) of the flexural a_0 mode.

In Figure 7.11, the symmetric mode s_0 (n=1) presents only one beam at about 62 MHz. This suggests that the mode suffers less deterioration due to edge reflections. Possible reasons are that the backward beam might be completely absorbed at the membrane clamp, and (or) that symmetric wave patterns induced by the combination of two piezoelectric constants d_{31} and d_{33}, allow constructive interferences between the main signal and the reflected beam. The symmetric mode propagates at a velocity of about 6200 m/s, which is much higher than ordinary SAWs velocity.

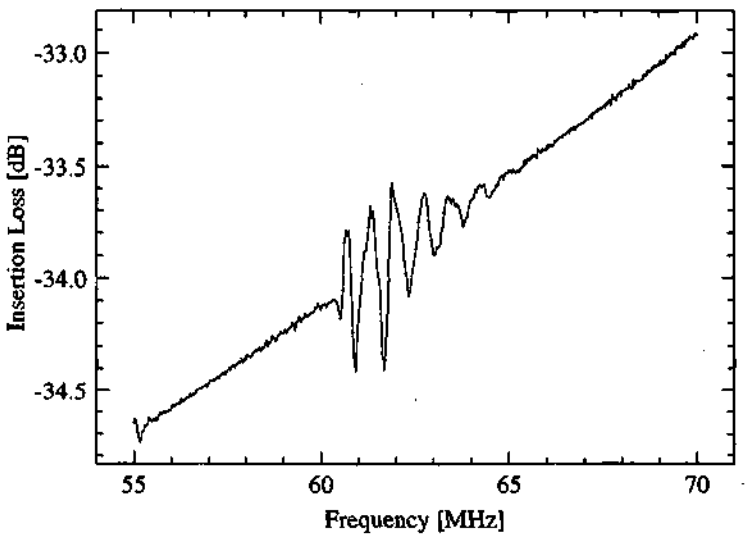

Figure 7.11: Narrow-band frequency response showing the symmetric s_0 (n=1) mode.

7.4.2 Influence of the bias voltage on the frequency response: polarization and depolarization

In order to obtain an acceptably transmitted acoustic signal, it was found necessary to superpose a d.c. bias on the applied r.f. signal. The application of the d.c. bias along the direction of preferred polarization effectively "poled" the PZT film, causing a local anisotropy in the ceramic layer due to a reorientation of the ferroelectric domains [7.4], and increasing both the amplitude of the wave motion and the stress in the membrane. Maximal efficiency was therefore obtained by keeping the absolute voltage amplitude (d.c. bias added to the r.f. excitation) just below the PZT saturation. In this way, each voltage excitation cycle is translated to a higher value on the hysteresis loop.

For acoustic purposes, as the ratio between the wavelength and ferroelectric domain size is of the order of 100 to 0.1, almost no wave scattering occurs due to unpoled PZT regions. Furthermore, due to a membrane thickness 50 times smaller than the acoustic wavelength, the IDT emitter, driven at the fundamental synchronous frequency, induces a flexural motion along the membrane with a periodicity of 100 μm. In comparison, SAW devices operating at several hundreds of megahertz have a wavelength of only a few micrometers and are, therefore, more sensitive to any physical variation of the substrate along the acoustic path.

Figure 7.12 shows the influence of the poling due to 9 V d.c. bias. A resonance frequency shift of 50 kHz associated with 28 dB insertion loss variation is observed. The phase velocity raise by an amount of 5 m/s and is related to the increase of the tension in the membrane (cf. paragraph 4). This example highlights the strong dependence between the bias voltage and the acoustic wave amplitude in ferroelectric Lamb-wave based devices.

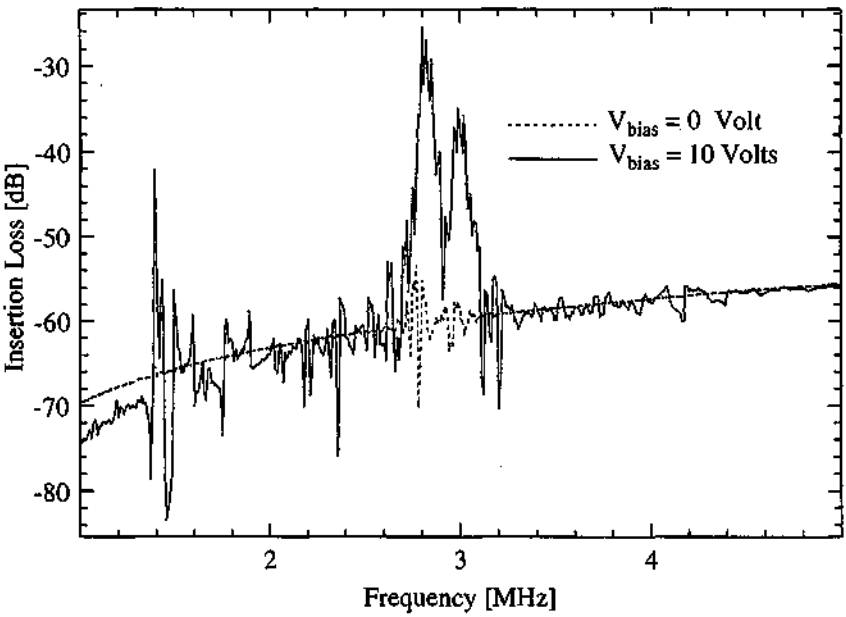

Figure 7.12: Influence of the poling due to 9 V d.c. bias. The resonance frequency shift is 50 kHz associated with a 28 dB increase of the insertion loss.

In the following, the frequency-response variations induced by the application of increasing bias voltages, is presented for several modes. The d.c. bias are 2V and 4V with respect to the unpoled case $V_{bias} = 0$ V.

Figure 7.13 exhibits the shape of standing waves near 1.4 MHz. The bias voltages increase the wave amplitude (9.466 dB for a bias of 4 V at a frequency very close to 1.4 MHz) but do not induce a significant frequency shift.

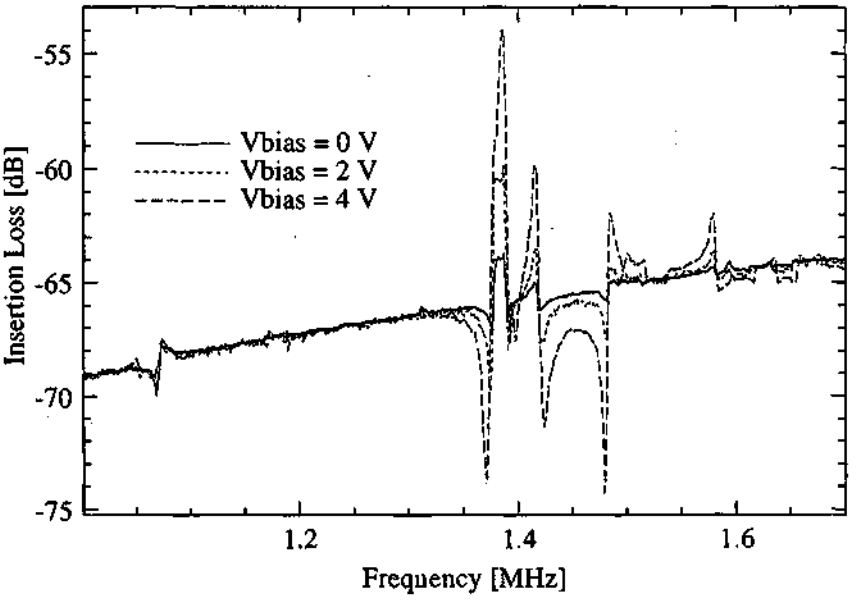

Figure 7.13: Standing waves emitted at frequencies between 1.35 MHz and 1.6 MHz, for three d.c. bias voltages: 0V, 2V and 4V.

Figures 7.14; 7.15; 7.16 and 7.17 point out the shape variations for the propagating modes a_0 (n=1); a_0 (n=2); a_0 (n=3) and s_0 (n=1), respectively. The a_0 (n=1) insertion loss pattern is shifted to higher frequencies with a gain of 16 dB, and a shift of 5 kHz for 4V bias. Harmonic modes a_0 (n=2) and a_0 (n=3) are less shifted than the fundamental mode. The even harmonic (n=2) undergoes a frequency *decrease* of 15 kHz while the odd harmonic mode (n=3) is slightly shifted (Δf= 12.5 kHz) to higher frequencies. The frequency of the symmetric mode is almost insensitive to bias voltage. These results are summarized in Table 7.1. It is obvious that the electromechanical coupling constant K^2 is much stronger for the lowest flexural a_0 (n=1) mode than for every other propagating mode.

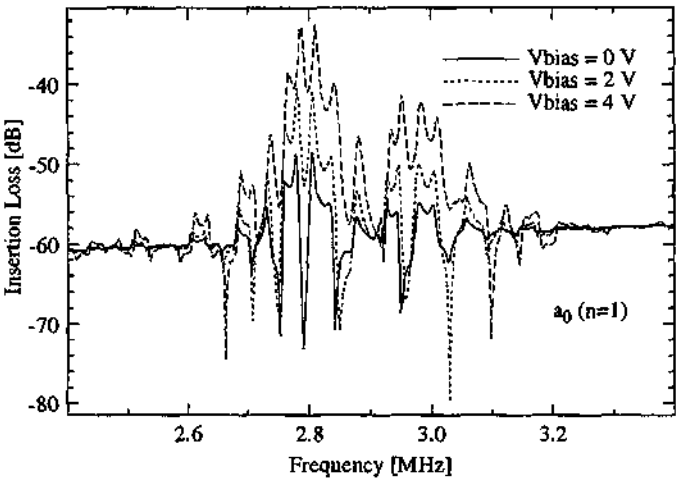

Figure 7.14: Frequency response for three d.c. bias voltages: 0V, 2V and 4V for the a_0 (n=1) mode.

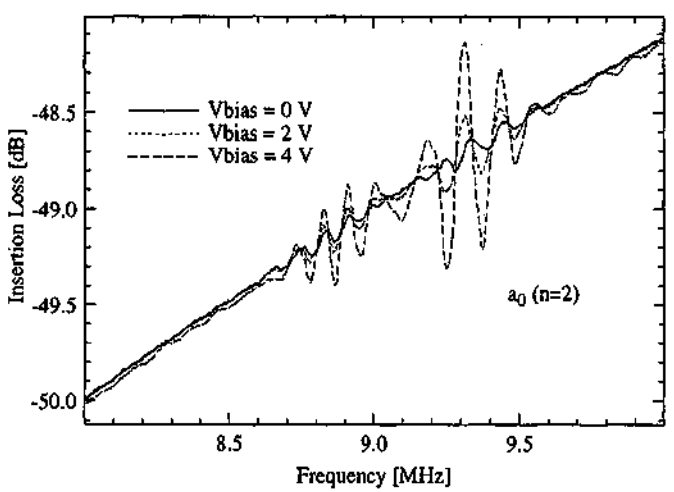

Figure 7.15: Frequency response for three d.c. bias voltages: 0V, 2V and 4V for the a_0 (n=2) mode

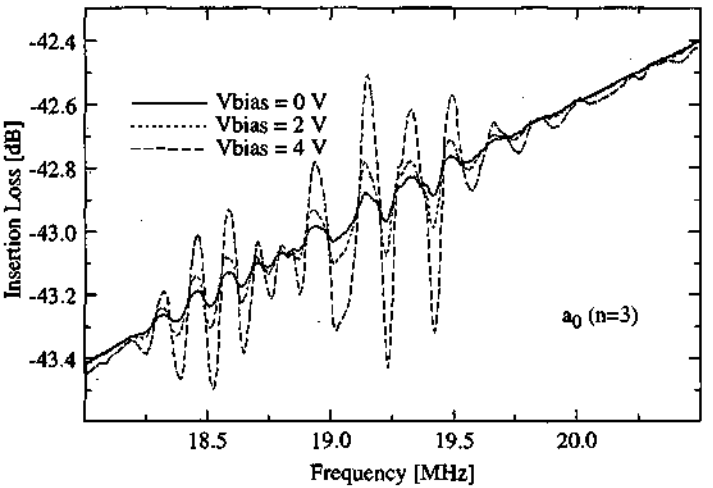

Figure 7.16: Frequency response for three d.c. bias voltages: 0V, 2V and 4V for the a_0 (n=3) mode

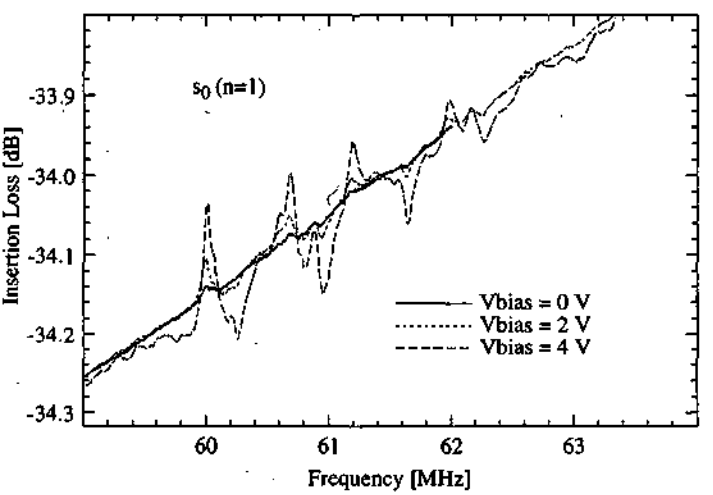

Figure 7.17: Frequency response for three d.c. bias voltages: 0V, 2V and 4V for the s_0 (n=1) mode

Wave type	Resonance frequency without bias [MHz]	Frequency shift induced by 4V bias [kHz]	Insertion Loss variation due to 4 V bias [dB]
standing waves	1.38675	0	9.46
flexural a_0 (n=1)	2.805	5	16
flexural a_0 (n=2)	9.33	-15	0.49
flexural a_0 (n=3)	19.1375	12.5	0.37
symmetric s_0 (n=1)	60.6725	0	0.08

Table 7.1: Polarization: frequency shift and amplitude increase of acoustic waves under the influence of a 4 V d.c. bias.

As soon as the d.c. bias is removed, the induced polarization decreases rapidly (depolarization) and the ferroelectric layer tends to approach a new state of equilibrium along its hysteresis curve. A remanent polarization is achieved after a few hours. In order to study this phenomenon with Lamb waves, a 9 V bias (saturation) was applied for a few minutes on a device at room temperature and then removed. The frequency response of this device was measured before the bias application and 12 hours after its suppression. Figures 7.18-21 show the insertion loss for each propagating mode, and Table 7.2 the principal results.

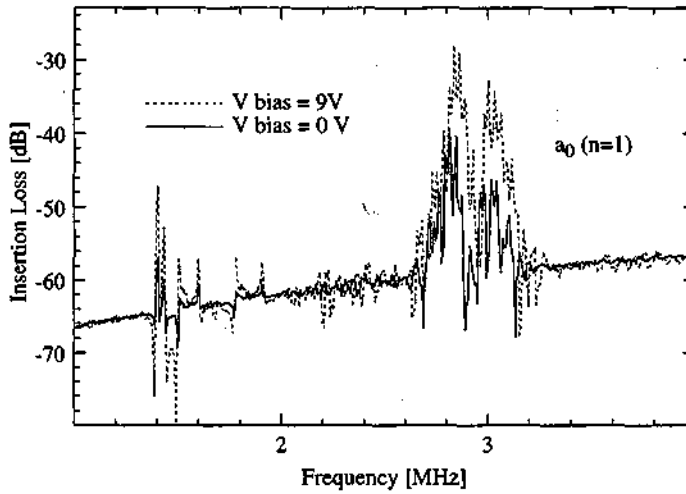

Figure 7.18: Frequency response of the a_0 (n=1) mode before and after the removal of a 9 V d.c. bias.

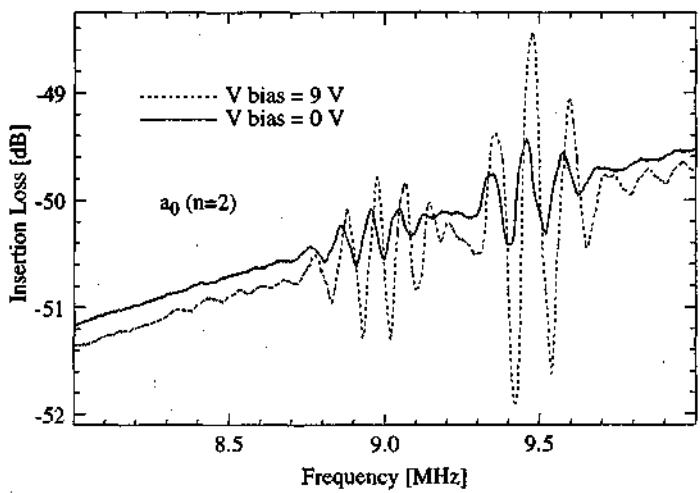

Figure 7.19: Frequency response of the a_0 (n=2) mode before and after the removal of a 9 V d.c. bias.

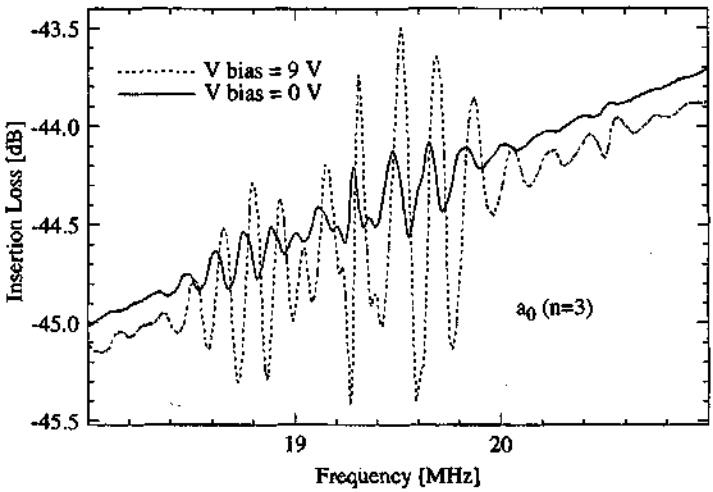

Figure 7.20: Frequency response of the a_0 (n=3) mode before and after the removal of a 9 V d.c. bias.

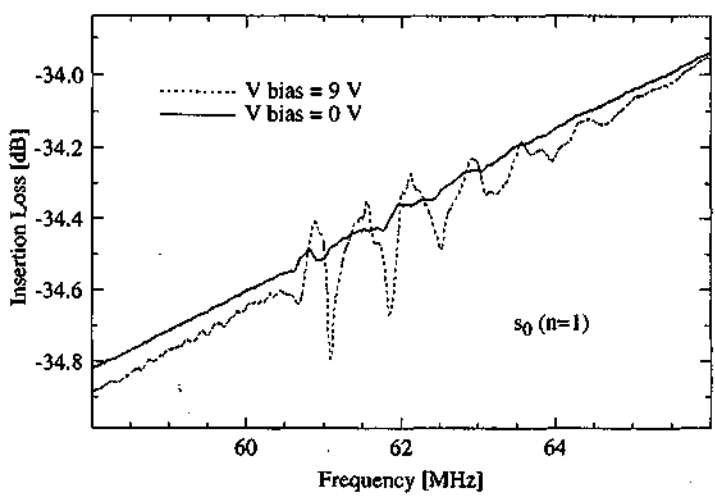

Figure 7.21: Frequency response of the s_0 (n=1) mode before and after the removal of a 9 V d.c. bias.

Wave type	Resonance frequency with 9 V bias [MHz]	Frequency shift [kHz]	Insertion Loss variation [dB]
standing waves	1.405	0	9.95
flexural a_0 (n=1)	2.8375	22.5	11.44
flexural a_0 (n=2)	9.48	20	0.98
flexural a_0 (n=3)	19.515	37.5	0.62
symmetric s_0 (n=1)	62.12	140	0.08

Table 7.2: Depolarization: frequency shift and amplitude decrease of acoustic waves induced by the suppression of a 9 V d.c. bias.

7.4.3 Lamb wave voltage sensor

A SAW device can be used as a d.c. voltage sensor when the propagating path between the two IDTs has electrodes on both sides of the substrate [7.5], [7.6], [7.7]. Sensors based on SAW offer the possibility of high-voltage measurements from -10 kV to 8 kV with a resolution of 0.4 V [7.8]. In case of Lamb wave devices, the upper voltage value is limited by the breakdown strength (kV/cm) of the piezoelectric sample. For our 0.7 μm thick PZT film, experimental tests give an upper limit value varying from 60 kV/cm up to 200 kV/cm. The breakdown strength depends on the ceramic composition and its processing. A 600 kV/cm strength was experimentally achieved on a 0.3 μm thick PZT layer, which corresponds to a bias voltage of 18 V. Hence, Lamb wave voltage sensors based on thin piezoelectric films are not foreseen as high-voltage measurement.

As previously seen, for our Lamb wave devices, the lowest order flexural mode a_0 (n=1) is much more sensitive than any other propagating mode, to a stress induced in the membrane. Here, the stress is produced by a biasing electric field under each IDT, and only the sensitivity of this fundamental a_0 mode is highlighted. Moreover, the acoustic path between both IDTs is not covered by an electrode, that is, only the region under the transducers contributes to induce an additional stress in the membrane. A bias voltage is applied to the ground electrode, and the frequency response is recorded, between 0 and 12 volts. Due to the ferroelectric PZT layer, the device was not subjected to a previous bias, in order to avoid a remanent polarization. Figure 7.22 shows 8 measured curves of insertion loss related to the flexural mode, between 2.7 MHz and 2.85 MHz. At 0 volt bias, the highest amplitude corresponds to a frequency just below 2.77 MHz.

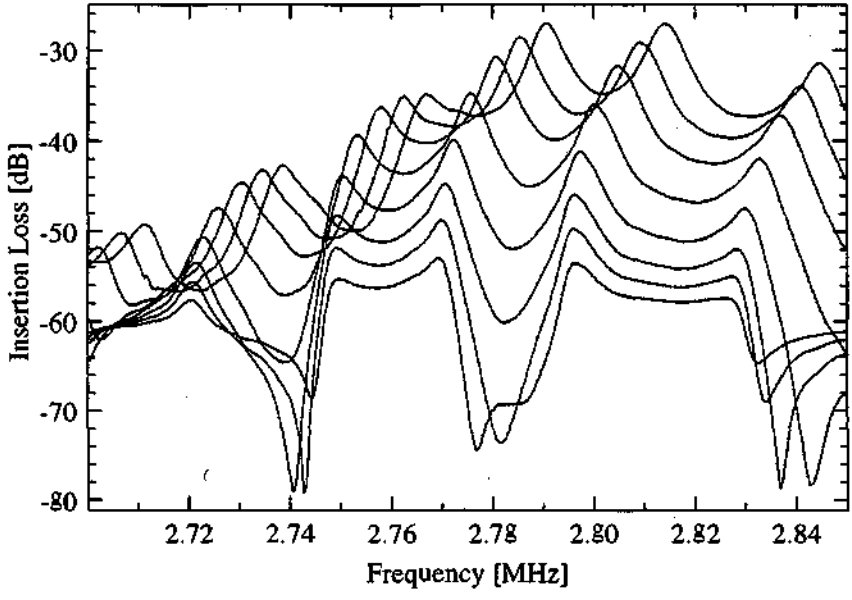

Figure 7.22: Influence of an increasing bias voltage (from 0 V, up to 7 V, with 1 V steps) on the lowest order a_0 (n=1) flexural mode.

The frequency and the insertion loss of this highest resonance peak are separately reported in Figure 7.23 as a function of the applied bias voltage. The synchronous frequency varies in accordance with a typical hysteresis loop in such ferroelectrics, with a saturated value near 9 volts bias. In the linear domain of piezoelectricity, between 4 V and 7 V, the frequency shift is 5 kHz/V. From this measurement, the voltage resolution at an oscillation frequency of 2.78 MHz is 5kHz/V, which suggests that this kind of device should act as a very sensitive d.c. voltage sensor when used in a differential closed-loop configuration with thermal and humidity compensation.

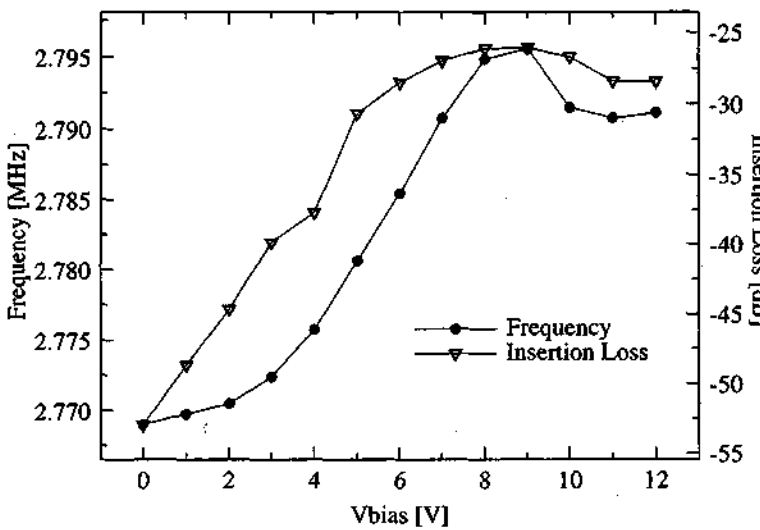

Figure 7.23: Influence of the poling bias on the resonance frequency and the insertion loss for the a_0 mode.

In comparison, SAW devices have a resolution of 13.8 Hz/V for a 0.5 mm thick $LiNbO_3$ substrate [7.9], or 60 Hz/V for a 1.8 μm thick ZnO layer on a Si substrate [7.10].

K. Toda et a.l. [7.11], have investigated the sensitivity of the zeroth symmetrical Lamb-wave mode on a 0.18 mm thick piezoelectric ceramic plate, and have obtained a resolution of about 2.5 kHz/V.

It is to be noted, that the sensitivity of our device can be greatly improved by placing a thin metallized electrode on top of the PZT film between the two IDTs. In that case, the propagating wave will be affected along its acoustic path and should therefore be extremely sensitive to any variation of the bias voltage.

7.4.4 Behavior of the resonance frequency and the insertion loss with time under a constant bias voltage

In this experiment, a constant biasing electric field is superimposed on the IDT alternating excitation provided by the HP gain-phase analyzer, and the IDT synchronous frequency of a Lamb wave device is observed as a function of time. More exactly, only the synchronous frequency of a given propagating mode is recorded during each frequency sweep. The resonant frequency corresponds to the flexural a_0 (n=1) mode. For a better accuracy, the frequency span is limited to 3 kHz only, and an averaging time of "8" allows a slow frequency sweep (38 s for each measure). A metallic closed box in which the device is placed, prevents air flow and external electromagnetic perturbations, while the bias voltage remains constant with a stability better than 10^{-4} V. Figures 7.24, 7.25 illustrates the Lamb wave sensor responses corresponding to a 3 V and a 9 V bias, respectively. Each curve corresponds to approximately 26 frequency sweeps. In both cases, we observe that the resonance frequency and the gain increase with time. This variation is not related to a temperature rise induced by the bias voltage, because it has been reported, that the oscillator frequency of a Lamb wave device *decreases* linearly when the temperature increases [7.12].

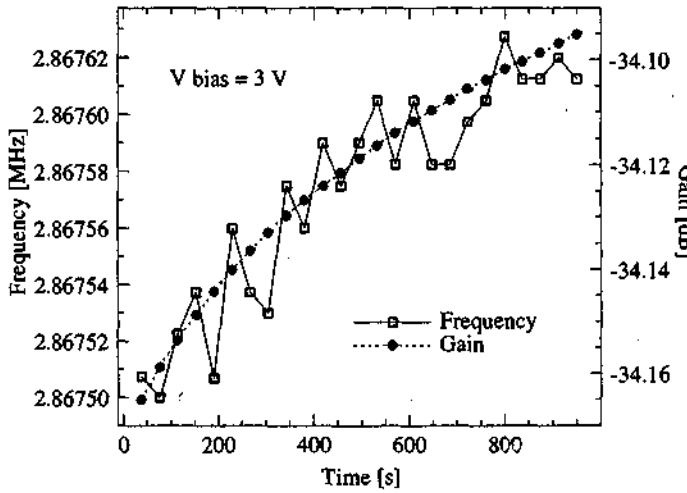

Figure 7.24: Stability of a Lamb wave sensor as a function of time. The excitation voltage is 90 mV and the fluctuation of the 3 V bias is less than 10 $^{-4}$ V.

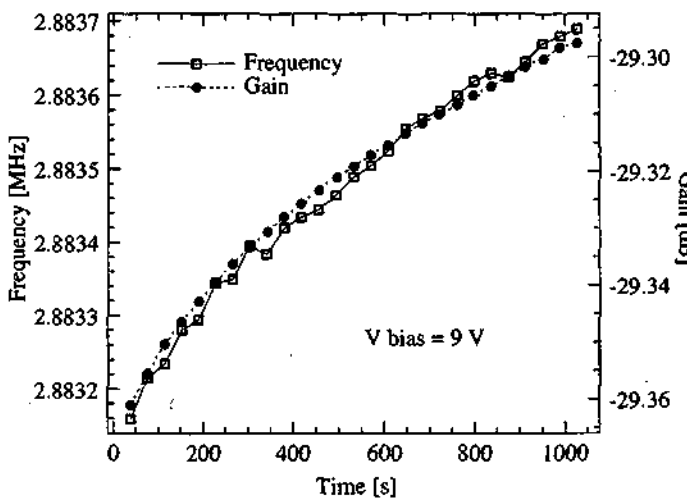

Figure 7.25: Stability of a Lamb wave sensor as a function of time. The excitation voltage is 90 mV and the fluctuation of the 9 V bias is less than 10 $^{-4}$ V.

Owing to the Lamb-wave voltage resolution (5 kHz/V), bias instabilities (< 10^{-4} V) allow only a frequency fluctuation of 0.5 Hz. This does not correspond to the observed frequency shifts of 120 Hz and 500 Hz after a time of 1000 s for a bias of 3V and 9V respectively. Voltage instabilities are therefore not involved. The reason for this variation is probably due to ferroelectric domain motions in the PZT film, which modify its stability, and *increase* its polarization with time [7.13]. Dynamic domain motion in terms of a minimal potential energy configuration could therefore be a reason for this peculiar behavior.

By analogy to the aging process (c.f. section 7.4.5) and despite the fact that our PZT sample was not initially poled, we observe that its physical properties, related here indirectly to frequency and gain shifts of a FPW acoustic a_0 mode, change linearly with the logarithm of time when a constant bias voltage is applied.

These results emphasize the important contribution of ferroelectric domain motions in PZT thin films, especially when a Lamb-wave device based on such piezoelectric layer has to be used in a closed-loop configuration under a constant bias field. If the ferroelectric sample is not previously correctly poled, the domain motion induced by the bias voltage will continuously shift the IDT synchronous frequency, causing an additional parametric variation to the aging process, and making the device less selective to a specific measurand.

7.4.5 PZT fatigue, aging and fast depolarization

For actuation purposes, the superposed d.c. bias and bipolar R.F. signal generates fatigue in the PZT thin film [7.14], [7.15]. With a 6-V d.c. bias and a 6-V_{pp} bipolar excitation at 3 MHz, a significant decrease of the FPW performance was observed after only 30 min. This decrease of piezoelectric coefficient also depends on the metal used as the IDT top electrode, (e.g.

metallic diffusion from electrode, space charge effects, electrode interface, ...) [7.16]. Another mechanism involved is the aging rate [7.17]. The aging rate or duration stability of a piezoelectric ceramic refers to properties that change with time, after a poling of the ceramic layer with an appropriate poling field strength, temperature and time [7.18]. Such a piezoelectric degradation of the PZT thin film can be illustrated by the decay of the piezoelectric response under d.c. bias and after its removal. The measurement of the resonance frequency amplitude with time of micromachined piezoelectric cantilever beams after removal of the bias voltage, allowed to point out this phenomenon. Figure 7.26 shows the amplitude decay of a beam after removal of a 410-kV/cm d.c. bias, which was applied during a 20-min period at ambient temperature on a 0.3 μm thick PZT film. This characteristic has been measured with an optical interferometer. A typical logarithmic decay has been obtained, with an initial fast component followed by a slow decrease. The measurement technique is explained in chapter 3.

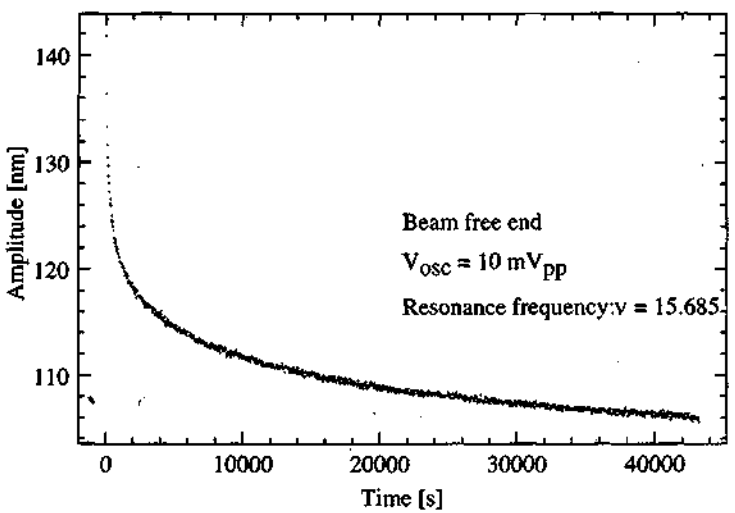

Figure 7.26: Interferometric measure of the amplitude decay of a 1-mm-length piezoelectric cantilever beam at the resonance frequency n = 15.685 kHz, after removal of a 410-kV/cm d.c. bias.

7.4.6 Poling of the PZT thin film

Due to the random orientation of the ferroelectric domains in the ceramic film, the PZT layer does not possess any piezoelectric properties before being poled. During the poling process, an external d.c. poling field 3 or 4 times larger than the coercive field (which decreases as the temperature increases) of the sample is applied to the layer and forces the ferroelectric domains to be globally reoriented.

Depending on the time duration, the breakdown strength and the temperature of poling, a remanent polarization will occur after the poling process. This remanent polarization will then be influenced by aging and fatigue phenomena which decrease the remanent strain and allow a reorientation of the dipoles. Usually, most of the lead-system piezoelectric ceramics are poled under a field of 2.5 to 4.5 kV/cm at 100-170 ^{0}C during 10-30 min [7.10].

Figure 7.27 exhibits a remaining polarization of a Lamb wave device, in term of insertion loss (I.L.) variation with time. Practically, only the region under the IDTs was poled with a 6 V bias at 95 ^{0}C during one hour. The dotted curve on Figure 7.27 corresponds to the frequency response before poling, while the upper curve is obtained just after the poling process. Two other curves, respectively measured 3 and 48 hours later, emphasize a slight or small decrease of the remaining polarization. Due to this thermal poling process, the I.L. decrease is only 2 dB after 48 hours.

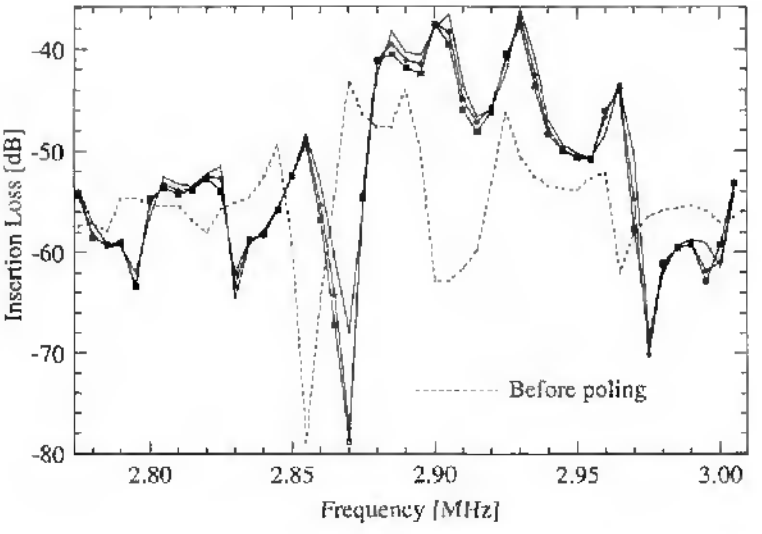

Figure 7.27: Frequency responses of a Lamb wave device before and after poling. The dotted curve corresponds to the frequency response before poling. The three upper curves correspond to the device response directly after poling, 3 hours and 48 hours later, respectively.

7.4.7 Optical visualization of standing wave patterns

It is possible to visualize standing Lamb waves by using a differential interference contrast (Nomarski) method [7.19]. Figure 7.28 shows the back side of the membrane with the two transducers located at the membrane ends in the opposite sides. When both IDTs are driven simultaneously, standing waves are produced in the membrane and allow useful observations. For instance, we see that the width of the standing wave channel between the two IDTs corresponds to the electrode aperture without major degradation along the acoustic path. In Figure 7.29 a detail of standing waves between the membrane extremity and one IDT is presented.

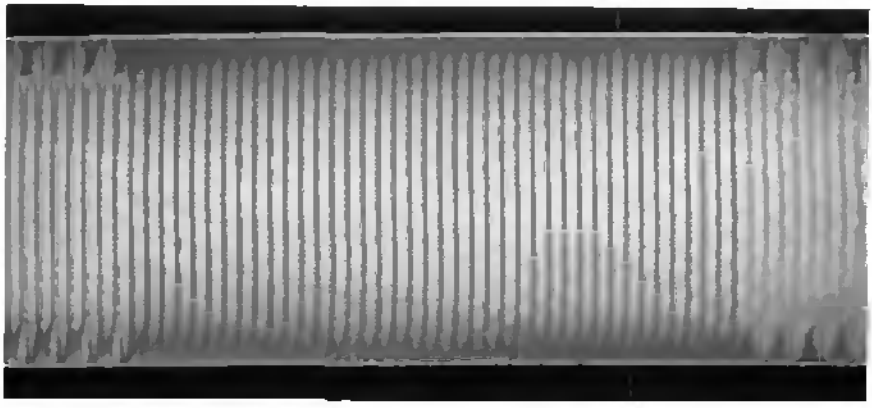

Figure 7.28: Micrograph of a FPW device illustrating standing Lamb waves when both transducers (left and right on the picture) are simultaneously excited at 2.87 MHz with 10 V bias added to a $1V_{pp}$ r.f. signal.

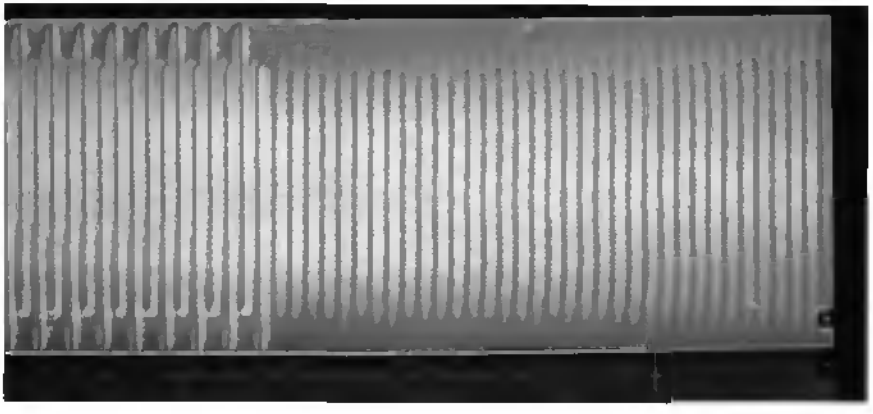

Figure 7.29: Optical view of standing Lamb waves between one membrane extremity and a driven IDT, excited at 2.87 MHz with 10 V bias added to a $1V_{pp}$ r.f. signal. (A small bead and its reflected image is visible on the bottom right).

When the excitation voltage and the bias increase, a rather complicated standing wave pattern appears due to in-plane stress gradients and waves reflections, and nodal profiles suffer an important distortion. An example of these profiles is given in Figure 7.30.

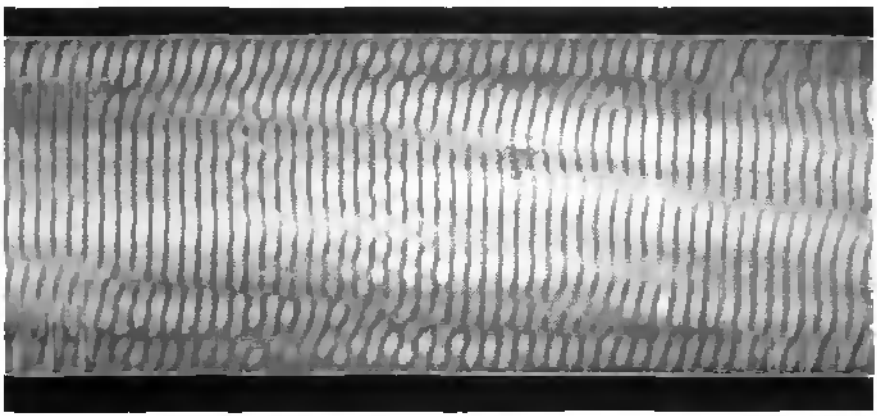

Figure 7.30: Standing Lamb waves pattern. The nodal line profiles are more complicated when both bias and excitation voltages increase. Here the bias is 10 V with an excitation of 5 V_{pp}.

Figure 7.31 shows the case when only one IDT is driven (the emitter is partially visible on the left of the picture). The propagating signal (not visible on the photograph) is strongly superposed on standing waves which build a rather complicated pattern. Vertical nodal holes (parallel to the IDT fingers) are coupled to horizontal standing waves (parallel to the top and the bottom of the picture) with various intensities. For some frequencies below the lowest-order propagating flexural mode a_0 (n=1), the IDT emitter generates pure standing waves. Figure 7.32 shows a pattern of such standing waves. The driven IDT is partially visible on the left. In this case, the IDT emitter was slanted.

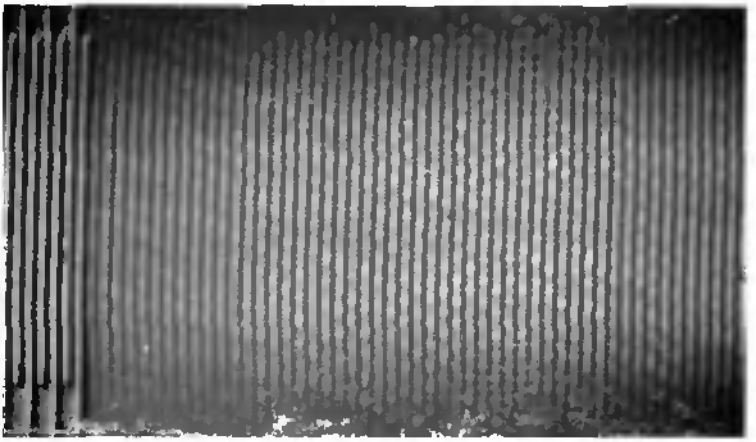

Figure 7.31: Nomarski view of standing Lamb waves when only one transducer (partially visible on the left) is excited. The driving frequency is 2.8625 MHz and corresponds to the synchronous frequency of the propagating lowest order flexural mode a_0. Multiple wave reflections occur at the edges of the suspended membrane.

Figure 7.32: Nomarski picture of standing waves corresponding to a driving frequency of 1.92 MHz. The emitter (partially visible on the left) is slanted. No propagating signal occurs for this frequency.

7.4.8 Edge reflections

As previously observed, reflections of the propagating acoustic signal on the membrane edges, represent the most important source of frequency response degradation. In SAW devices, spurious reflections are easily suppressed by using a soft layer behind each IDT at the extremities of the device, because the amplitude of these waves are only a few Angströms. For Lamb-wave devices, it is also possible to use this simple method, although the wave amplitude is two or three orders of magnitude greater. Here, the edge extremities of the membrane were covered on both sides by a small amount of epoxy and soft photoresist materials. Figure 7.33 shows a detail of a suspended membrane where the angular edge profile is modified with the epoxy glue. The new profile is supposed to avoid destructive interferences between the forward and backward reflected waves.

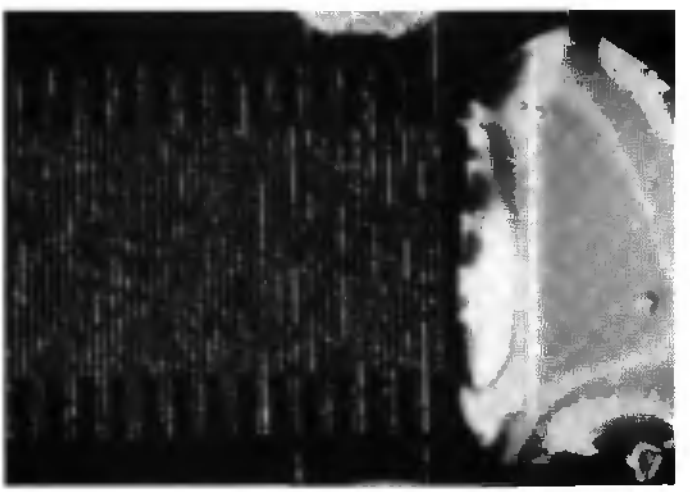

Figure 7.33: Optical view of a modified membrane edge profile. The soft epoxy glue allows to suppress spurious reflections.

The efficiency of this simple method is demonstrated in Figures 7.34-37. Figure 7.34, shows the frequency response of the device before using epoxy. The two main signals are clearly present. In Figure 7.35, only one main signal, with some ripples, is essentially present.

This is also visible in the pictures (7.36 and 7.37) for the even and odd harmonics respectively.

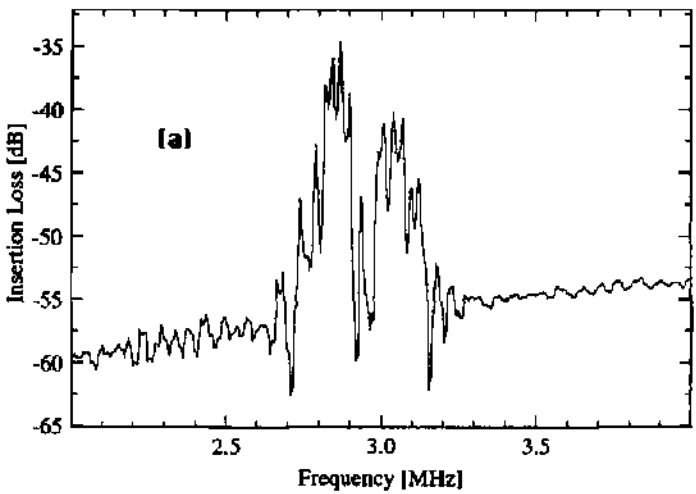

Figure 7.34: Experimental study for the suppression of spurious Lamb-wave edge reflections. Here, the device has its two extremities not covered by an epoxy layer and shows therefore two main signals..

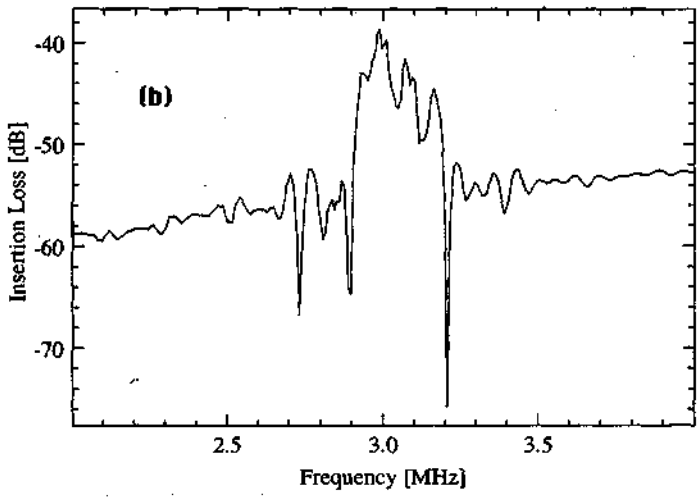

Figure 7.35: Experimental study for the suppression of spurious Lamb wave edge reflections. Here, the same device exhibits only one main signal when the spurious edge reflections are partially absorbed.

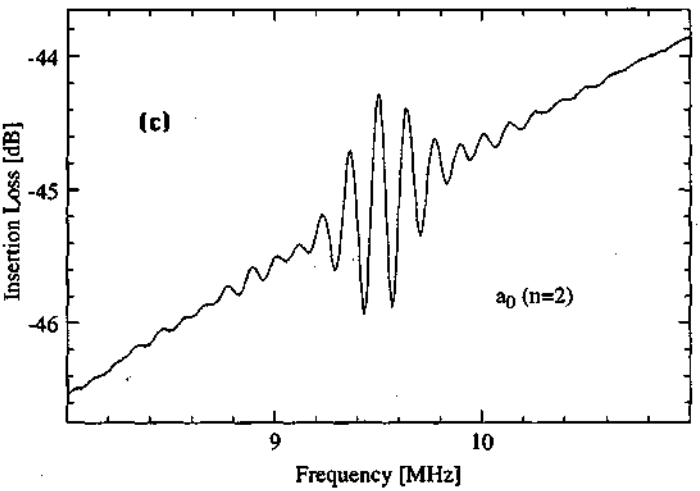

Figure 7.36: Experimental study for the suppression of spurious Lamb wave edge reflections. The harmonic mode a_0 (n=2) shows only one main signal.

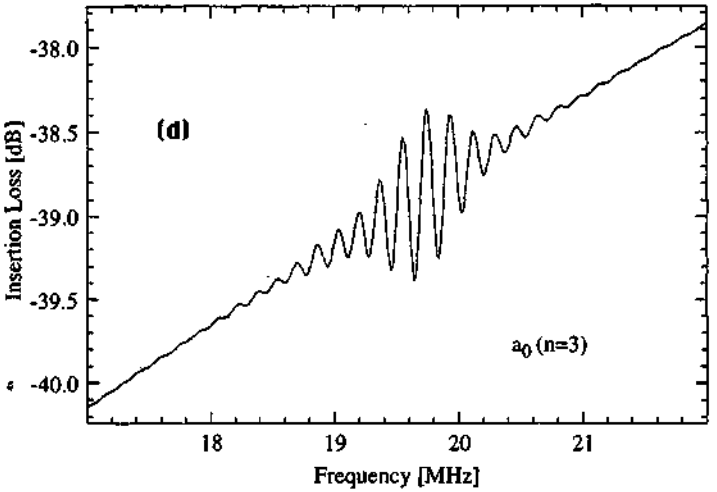

Figure 7.37: Experimental study for the suppression of spurious Lamb wave edge reflections. The harmonic mode a_0 (n=3) shows only one main signal.

7.4.9 Experimental phase and group velocities of the lowest order (n=1) a_0 and s_0 modes

Phase velocities Vp of each fundamental a_0 and s_0 (n=1) modes are obtained using the phase relationship:

$$Vp = f_0\lambda \qquad (7.6)$$

where f_0 is the resonant frequency and λ is the acoustic wavelength (100 μm). f_0 was determined by observing the frequency at which maximal transmission of the acoustic signal between the IDTs occurred.

Group velocities of the a_0 mode are determined by pulsing the delay line with a bipolar burst of 10-20 cycles at the IDT synchronous frequency f_0, and measuring on an oscilloscope the delay time required to propagate the r.f. signal from the transmitting IDT to the receiving IDT. Figure 7.38 shows a typical oscilloscope trace of the lowest order antisymmetric mode a_0. The trace shows a rather complicated pattern of responses. The first burst in the trace is the radiative feedthrough which propagates at the velocity of light and marks the beginning of the r.f. burst t=0 s. The second burst is the transmitted lowest order antisymmetric Lamb wave and shows a delay time of 8.4 μs. The remaining sets of bursts which follow the main signal, result from reflections of the acoustic energy from the ends of the suspended membrane and IDTs themselves.

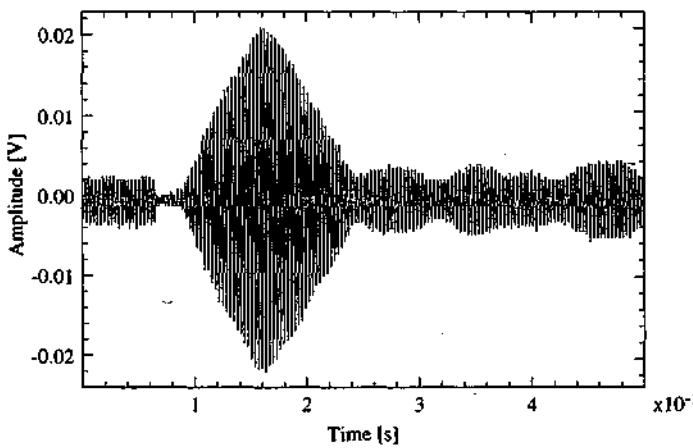

Figure 7.38: Oscilloscope trace of the lowest order a_0 antisymmetric mode. Burst of 20 shots at a frequency f_0 = 3.119 MHz and with V_{bias} =15 V and $V_{excitation}$ = 1.4 V_{pp}.

Figure 7.39 shows another oscilloscope trace of the detected a_0 mode when a 20-shot burst is applied to the emitter at a frequency of 2.86 MHz with an amplitude of 2 V peak-to-peak. Here the delay time is 9.35 μs.

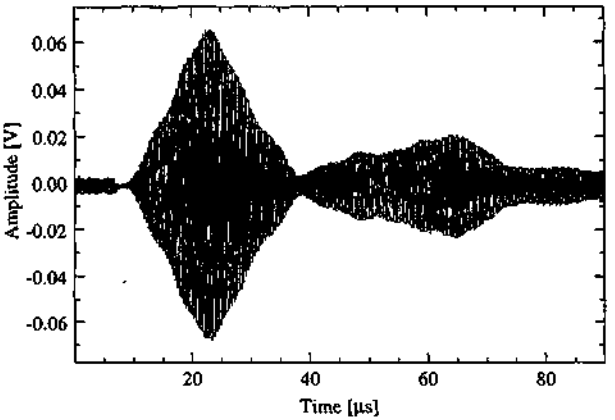

Figure 7.39: Oscilloscope trace of the fundamental a_0 antisymmetric mode. The time delay is 9.35 µs, corresponding to a group velocity of 374 m/s. The excitation voltage is 2 V_{pp} at a synchronous frequency of 2.86 MHz.

Figures 7.40 and 7.41 illustrate two other impulse responses with a more complicated set of remaining bursts after the main signal.

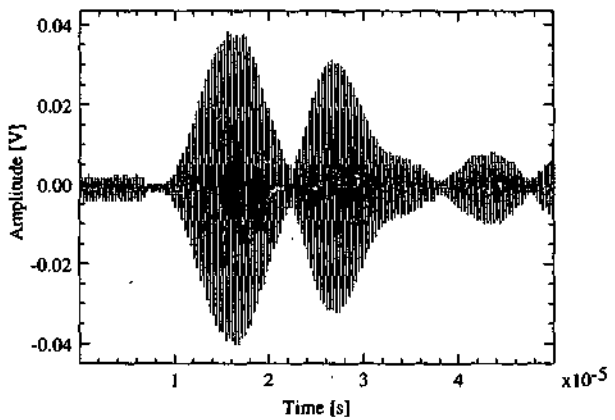

Figure 7.40: Example of a Lamb-wave impulse responses. The resonant frequency is 2.979 MHz with a bias of 15 V, an excitation of 5 V_{pp} and a burst of 20 shots.

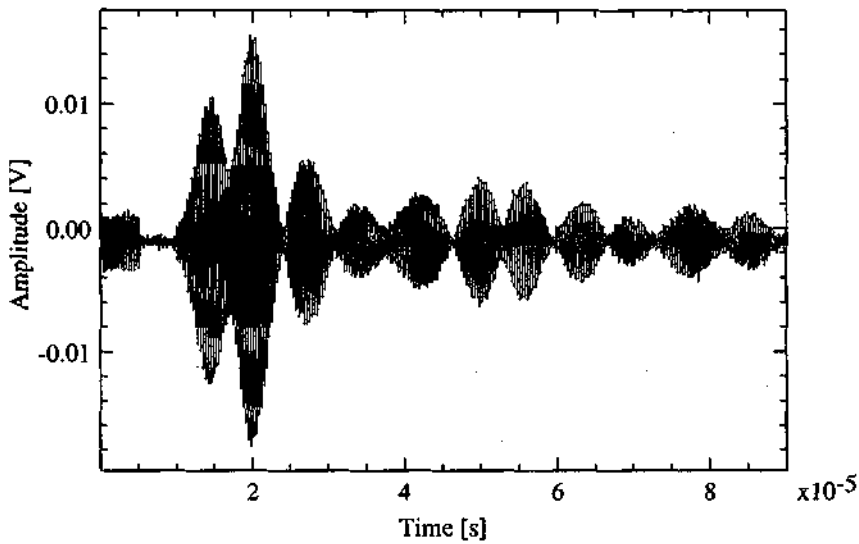

Figure 41: Example of a Lamb-wave impulse responses. The resonant frequency is 3.0025 MHz with a bias of 9 V, an excitation of 4 V_{pp} and a burst of 15 shots.

The acoustic delay-lines of the second generation resulted in phase velocities between 286-312 m/s and group velocities between 374-454 m/s, for the thinnest membranes and for the lowest order (n=1) antisymmetric plate mode a_0. The phase velocity is a very sensitive function of both the thickness and residual stress of the membrane. Variations in the velocities (dispersion) reflect small differences in the thickness of the composite membranes due to processing variations. The group velocity is approximately 1.31-154 times the phase velocity, indicating the anomalous dispersion of the antisymmetric flexural mode a_0.

For symmetric modes s_0 , the phase velocities are situated between 6.1-6.2 km/s and present almost no dispersion. Unfortunately, it was not possible to measure their group velocity, the burst pulsation of the HP function generator being limited to 5 MHz. Table 7.3 summarizes these experimental velocities.

wave type	bias voltage [V]	resonant frequency [MHz]	phase velocity V_p [m/s]	group velocity V_g [m/s]	V_g/V_p ratio
flexural a_0	15	3.119	311.9	413.8	1.33
flexural a_0	15	2.980	298	448.3	1.50
flexural a_0	10	2.950	295	454.5	1.54
flexural a_0	10	2.860	286	374	1.31
symmetric s_0	10	62	6200	----	----

Table 7.3: Experimental Lamb-wave phase and group velocities of the lowest order (n=1) antisymmetric a_0 and symmetric s_0 modes.

7.4.10 Comparison between measured and calculated phase and group velocities of the lowest order (n=1) a_0 mode

Exact calculation of Lamb wave velocities in a composite membrane are possible, using a numerical program [7.20]. Here, the phase and group velocities are calculated with the simple formula given in chapter 4, and compared with experimental results. Formally, it is more an estimation than a pure calculation, because several parameters (e.g. Poisson's ratio, Young's modulus and the density of low stress silicon nitride) are difficult to determine precisely.

According to formula (4.10), the phase velocity Vpa_0 is obtained without taking into account the in-plane tension T. For this estimation, we use the following values:

λ = 100 µm (IDT period)

d = 1.9 µm (membrane thickness)

$E = 0.5(E_{PZT} + E_{SixNy}) = 0.5(7.246 \cdot 10^{10}\,Nm^{-2} + 300 \cdot 10^{9}\,Nm^{-2})$

$= 1.862 \cdot 10^{11}\,Nm^{-2}$

$\upsilon = 0.5(\upsilon_{PZT} + \upsilon_{SixNy}) = 0.5(0.2949 + 0.22) = 0.2575$

$p = 6.25 \cdot 10^{3}\,kgm^{-3}$ (calculated by summing the density values of each layer which compose the membrane)

Poisson's ratio and Young's modulus for PZT and Si_xN_y are obtained from [7.10] and [7.21], respectively. We obtain: Vpa_0 = 194.7 m/s, which is much lower than the experimental value given in Table 7.3

If we do not neglect the in-plane residual tension T, the same procedure can be applied to formula (4.24). In that case, the resulting in-plane tension is estimated by:

$$T = d(\sigma_{PZT} + \sigma_{SixNy}) = d(0.2 \cdot 10^{9}\,Nm^{-2} + 0.1 \cdot 10^{9}\,Nm^{-2}) = 570\,Nm^{-1}$$

and we obtain: Vpa_0 = 293.1 m/s. In both previous calculations, the platinum layer was neglected.

For the group velocity Vga_0, we refer to formula (4.47) and use the three following experimental values: Vpa_0 = 300 m/s, f_1 = 3 MHz, and f_3 = 19 MHz, where Vpa_0 is the phase velocity, f_1 the fundamental IDT synchronous frequency and f_3 the resonant frequency of the odd harmonic n=3.

We obtain: $Vga_0 = 1.432\ Vpa_0$ which is in good agreement with experimental results. Table 7.4 summarizes the former results.

wave type	calculated phase velocity without tension: formula (4.10)	calculated phase velocity with tension: formula (4.24)	measured phase velocity	calculated group velocity: formula (4.47)	measured group velocity
a_0 (n=1)	194.7 m/s	293.1 m/s	298 m/s	427.2 m/s	448.3 m/s

Table 7.4: Comparison between phase and group velocity estimations and experimental results.

7.4.11 Calculation of the group velocity for the even harmonic (n=2) a_0 mode

With equation (4.50) it is possible to obtain the group velocity of the first even harmonic mode (n=2). As an example, we refer here to the experimental results presented in section 7.4.2. The synchronous frequency of the fundamental a_0 mode is 2.81 MHz, and the even n=2 harmonic mode is located near 9.3 MHz when a 4 V bias is applied (c.f. Figures 7.14 and 7.15).

With k=100 μm, $Vpa_0(n=2) = 465$ m/s and $Vpa_0(n=1) = 281$ m/s, we find:

$$Vga_0(n=2) = 1.212\ Vpa_0(n=2) = 563.4 \text{ m/s}$$

As a consequence, we observe that the dispersion of harmonic Lamb modes is smaller than that of the fundamental mode n=1.

7.4.12 Determination of the residual in-plane stress T of the membrane

For thin microfabricated membranes, the in-plane residual tension is an important parameter and is difficult to quantify precisely. Methods based on the membrane deflection versus pressure have been reported [7.22]. Here the proposed method is very simple, because it requires only to determine the circular frequencies ω_1 and ω_3 of the flexural a_0 fundamental mode (n=1) and first odd harmonic (n=3), respectively.

This can be rapidly done by observing the frequency response of the device. In chapter 4, section 4.8, an expression (4.43) was derived which relates the in-plane tension T to the former frequencies, the plate density and the plate thickness. For the calculation of T we use:

$p = 6.25 \cdot 10^3$ kgm^{-3} (plate density)
$d = 1.9$ μm (plate thickness)
$k = 2\pi/\lambda$
$\lambda = 100$ μm (IDT period)
$\omega_1 = 2\pi f_1 = 2\pi$ 2.81 MHz
$\omega_3 = 2\pi f_3 = 2\pi$ 19.13 MHz

and we obtain: T = 451 N/m.

If the bulk silicon frame does not generate additional perturbation, then the tensile stress in the 1.9 μm thick composite membrane corresponds to 0.24 GPa, which is in accordance with experimental data given in chapter 6, section 6.4.1.

This simple method can be applied to thin membranes coated with a superconducting film (e.g. Nb or high-T_c $Y_1Ba_2Cu_3O_7$). The phase transition between normal and superconducting states generates ultrasound attenuations [7.23], which could be detected by measuring the IDT synchronous frequency shift induced by the tensile stress variation.

SAW attenuation due to the electron-phonon interaction at the superconductive transition has been studied for high frequencies [7.24], [7.25]. In our case, despite the fact that the FPW synchronous frequency is very low, the high sensitivity of the a_0 (n=1) mode offers a unique opportunity to find some acoustic signal connected with superconductivity.

7.4.13 Acoustic attenuation measurement

For a wave packet generated by the IDT emitter, and traveling along the membrane between the two transducers, there are many factors that influence the acoustic attenuation (spurious reflections, scattering, dissipation in the different layers, etc.) In our case, the amount of acoustic attenuation in terms of the voltage amplitude variation of a given burst signal, corresponding to one edge reflection and one acoustic path length, was extrapolated. Figure 7.42 illustrates the measured amplitude voltage at the IDT receiver, as a function of the burst amplitude for 9 V poling bias and a 20-shot burst. The main signal, measured at the receiver before the first edge reflection, corresponds to the wave group that has crossed one acoustic path length between the centers of the two transducers. The first echo corresponds to a wave packet detected at the same IDT receiver, which has crossed the whole membrane length three times and has been reflected twice on the membrane edges.

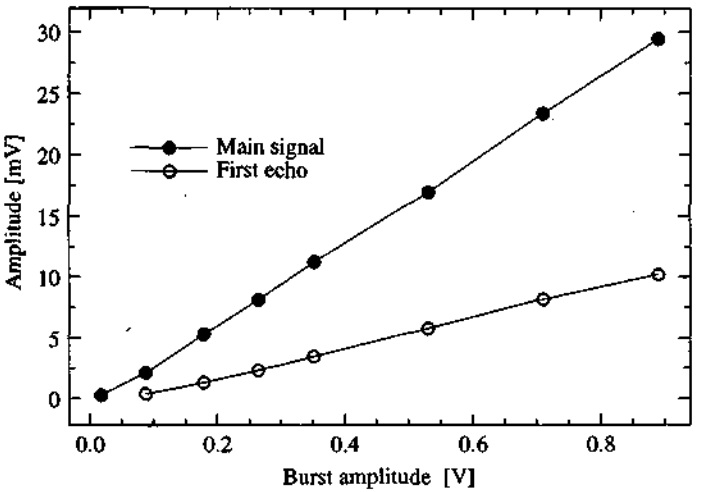

Figure 7.42: Measured voltage amplitude at IDT receiver as a function of the burst amplitude. Poling bias is 9 V, synchronous IDT frequency is 2.83 MHz, and the excitation is provided by a 20-shot burst. The main signal corresponds to one acoustic path length, while the first echo corresponds to three acoustic path lengths and two edge reflections. The extrapolated acoustic attenuation corresponding to one membrane length and one edge reflection is 33% of the initial amplitude.

It has been possible to extract the propagating wave packet loss by measuring the difference between the main signal and the first echo (see Fig. 7.42). This measurement results in a 33% acoustic wave packet loss after one membrane path length and one edge reflection.

Instead of varying the burst amplitude, it is possible to study the acoustic attenuation by varying the burst shots, as shown in Figure 7.43. In that case, we observe that the resulting acoustic attenuation is comparable to the previous one.

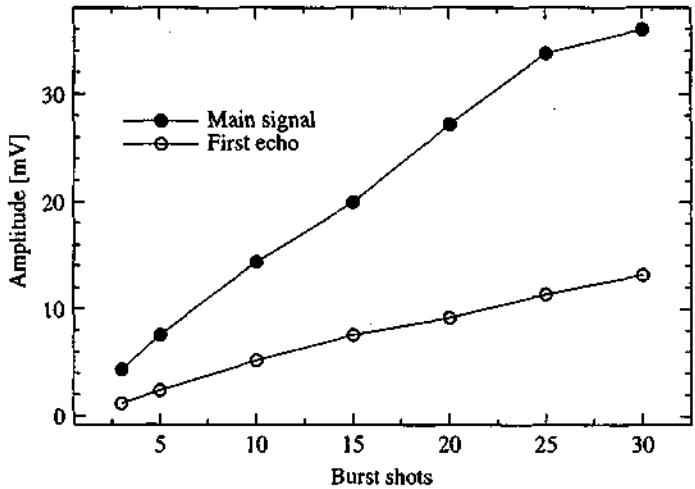

Figure 7.43: Measured amplitude voltage at IDT receiver as a function of the burst shots. Poling bias is 9 V, synchronous IDT frequency is 2.83 MHz. The main signal corresponds to one acoustic path length, while the first echo corresponds to three acoustic path lengths and two edge reflections. The extrapolated acoustic attenuation corresponding to one membrane length and one edge reflection is about 33% of the initial amplitude.

For mechanical transport applications, the power carried by the reflected wave packet strongly affects the velocity of moving microparticles and fluids.

7.4.14 Unipolar voltage excitation (IDT unbalanced)

When one comb of the IDT emitter is not activated but simply connected to the ground potential, the other comb can be driven separately. With this configuration (IDT unbalanced), it is also possible to generate acoustic waves, but less efficiently. Figure 7.44-45 shows a comparison between two frequency responses obtained with the balanced and unbalanced configurations. In our case, one comb of the driven IDT is floating instead of being connected to the

ground, and for both measures, the acoustic signal is detected with a balanced IDT receiver. An insertion loss difference up to 10 dB is observed.

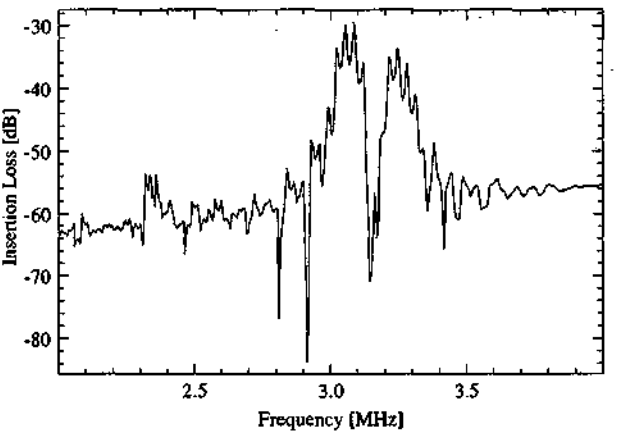

Figure 7.44: Frequency response obtained with a balanced IDT emitter. The receiver transducer is balanced, and bias voltage is 0 V.

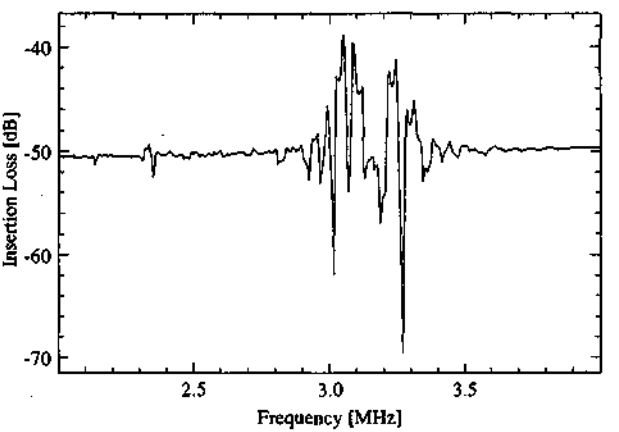

Figure 7.45: Frequency response obtained with an unbalanced IDT (floating). The receiver transducer is balanced, and bias voltage is 0 V.

7.4.15 Electromagnetic feedthrough and triple-transit-interferences (TTI) degradation

As mentioned in chapter 5, section 5.5, electromagnetic feedthrough and TTI between the two IDTs generate periodic ripples across the passband of the transducer at frequencies $f_r = 1/\tau$ and $f_r = 1/2\tau$ respectively, where τ is the acoustic delay time between both IDTs. The delay time is given by:

$$\tau = \frac{d}{V_{pa_0}} \qquad (7.7)$$

with d the acoustic path length and Vpa_0 the phase velocity of the considered propagating mode. On Figure 7.46, the jaggedness of the passband is principally due to these ripples, which occur at periodic frequency intervals Δf. Figure 7.46 shows that: 20 kHz ≤ Δf ≤ 35 kHz.

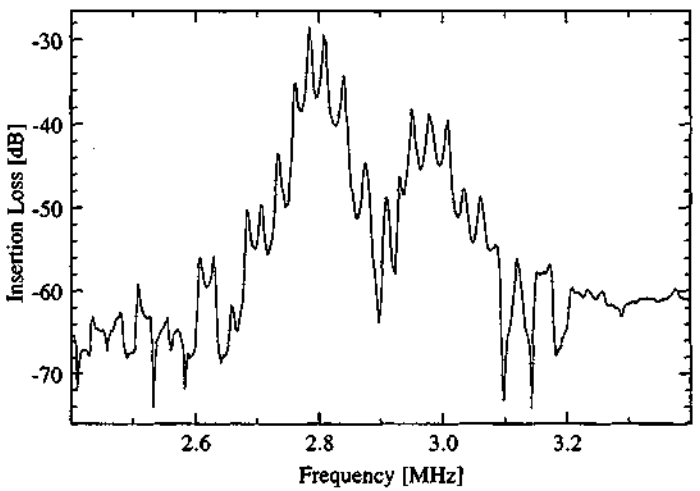

Figure 7.46: Frequency response of a Lamb wave device showing periodic ripples.

For the device involved here, $Vpa_0 = 280$ m/s and d = 5.45 mm. Hence, if we calculate the TTI frequency, we find $f_t = 1/2\tau = 25$ kHz, in good agreement with the experimental values.

7.4.16 Noise measurement

The frequency response of our FPW devices is characterized by an increase of Insertion Loss (IL) with frequency. This r.f. leakage arises due to mutual coupling between the external circuitry connected to the input and output IDTs, as well as due to the direct coupling between both transducers (electromagnetic feedthrough and TTI).

The mutual coupling between the external circuitry only, can be measured without device under test, i.e. both IDTs are disconnected from the external circuitry, and this coupling is referred to here as "noise measurement".

Figure 7.47 (a) shows such a measurement. The phase response is almost linear with frequency up to 100 MHz, the R.F. leakage being non dispersive in air. If the frequency is represented on a log scale (see Fig. 7.47 (b)), the previous I.L. shows a linear dependence with frequency. Hence, by analogy with the behavior of a capacitance versus frequency (c.f. section 7.2.2), we observe that the increase of I.L. with frequency is essentially due to a *capacitive* coupling between input and output connections to the IDTs.

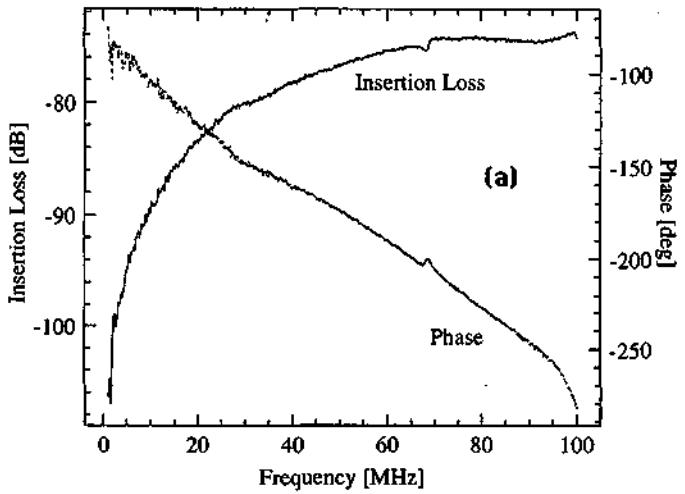

Figure 7.47 (a): Frequency response without FPW device under test. A resulting 30 dB variation occurs with a linear phase response up to 100 MHz.

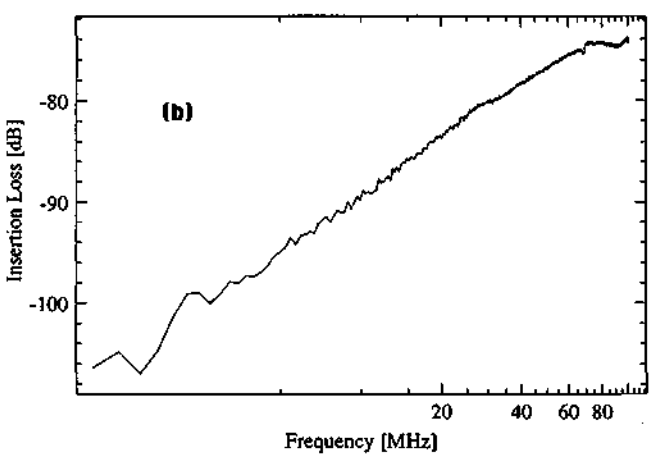

Figure 7.47 (b): Frequency response without FPW device under test.. The I.L. behavior indicates a capacitive coupling between the external circuitry.

7.5 Air-loaded FPW devices of the first generation

This paragraph deals with Lamb wave devices fabricated with the same process as for piezoelectric cantilever beams (c.f. chapter 3). Due to pinholes in the PZT film, only a few devices have shown ability to launch Lamb waves. Figures 7.48 (a) and (b) presents one of the various configurations investigated. This design allows us to observe an interaction between several waves at various angles. Unfortunately, only one of the three sets of IDTs was not shorted to the ground level. Compared to Lamb wave structures of the second generation, the devices presented here have a passivation layer (0.9 μm of Chemical-Vapor-Deposited silicon dioxide, CVD SiO_2 at 350 ^{0}C) which covers the entire area.

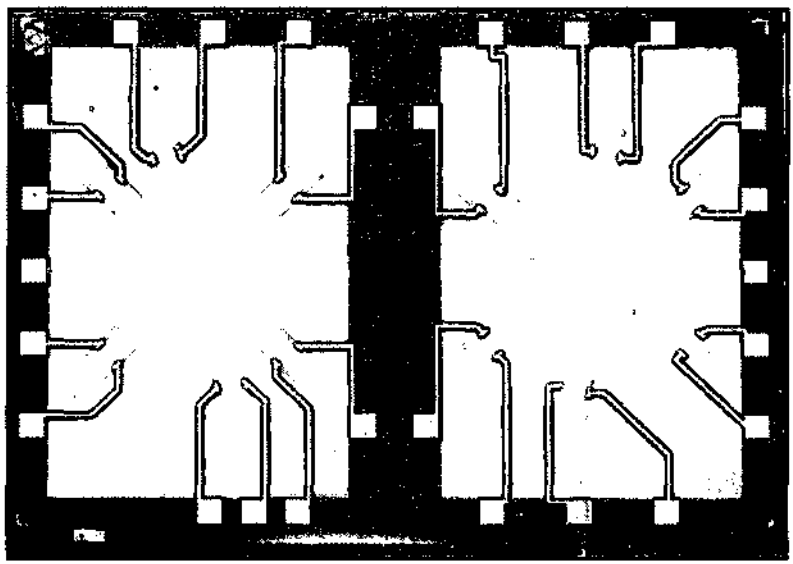

Figure 7.48 (a): Optical view of a Lamb wave device of the first generation. The suspended membrane is 4.74 mm width and 7.64 mm long. Three sets of two IDTs are differently oriented. Each IDT consists of 10 apodized finger-pairs with a period of 100 μm.

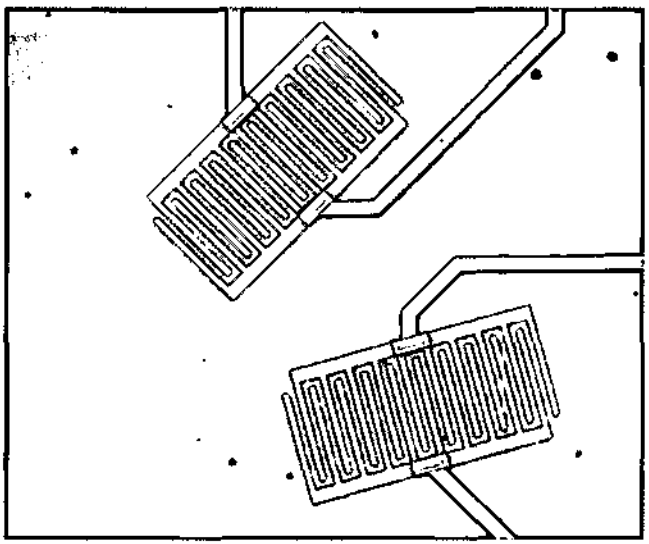

Figure 7.48 (b): Detail of two slanted IDTs of the first generation

7.5.1 Frequency response of a 16.4 μm thick plate device

Figures 7.49 and 7.50 illustrate the frequency response of such a device. The plate thickness is 16.44 μm, i.e. consists of 14.3 μm Si, 0.7 μm Si_xN_y, 0.1 μm Ta/Pt, 0.44 μm PZT, and a 0.9 μm SiO_2 passivation. In (a), the three noisy regions between 1MHz and 14 MHz are associated with standing waves. The lowest order (n=1) flexural mode a_0 is detected at a center frequency of 18 MHz (bias = 8 V), while in (b), this mode appears at a center frequency near 16.5 MHz when the bias is only 5.9 V. Spurious edge reflections are not present because the backward emitted waves are strongly deviated and can not interfere with the main signal. Therefore, the insertion loss of the a_0 mode is symmetric with respect to its synchronous frequency. The rapid increase of I.L. with frequency is due to strong capacitive coupling between the input and output IDTs external connections.

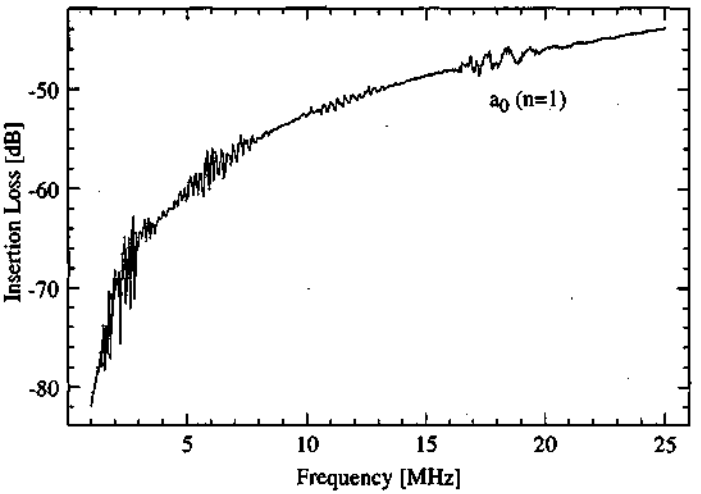

Figure 7.49: Frequency responses of a 16.4 μm thick Lamb wave device. On the left part, the detected signals up to 14 MHz correspond to standing waves. A flexural mode a_0 (n=1) is generated at a frequency near 18 MHz. Bias voltage is 8 V.

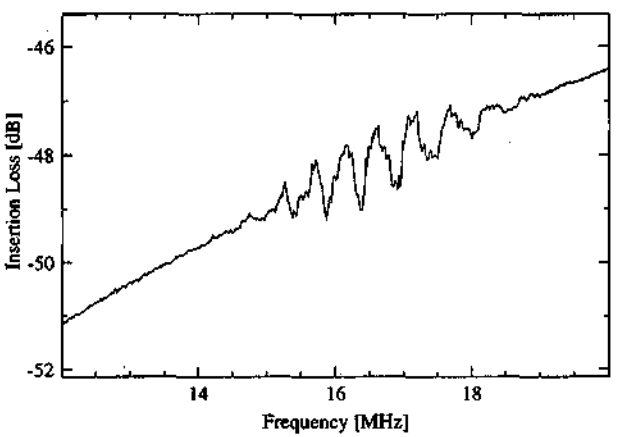

Figure 7.50: Narrow view of the frequency responses of a 16.4 μm thick Lamb wave device. The synchronous frequency of the flexural mode is about 16.5 MHz for a bias of 5.9 V.

7.5.2 Frequency response of a 2.2 μm thick plate structure

The structure involved presently, has a plate constituted of 0.6 μm Si_xN_y, 0.08 μm Ta/Pt, 0.58 μm PZT, and a 0.9 μm CVD SiO_2 passivation, i.e. the total plate thickness is 2.16 μm. Figure 7.51 shows the frequency response under a bias of 16 V. The a_0 (n=1) mode appears at 2.25 MHz, the a_0 (n=3) harmonic approximately at 18 MHz, and the symmetric s_0 (n=1) mode at about 55 MHz. The even harmonic (n=2) is not clearly visible, due to noise.

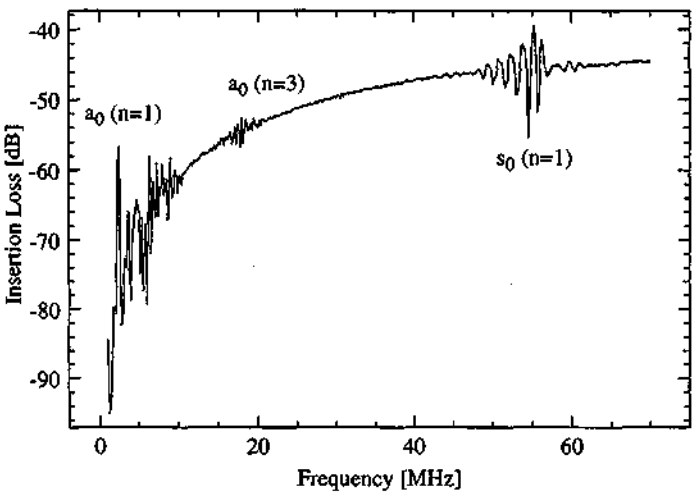

Figure 7.51: Frequency response of a 2.2 μm thick Lamb wave device. Propagating modes are detected at: 2.25 MHz, 18 MHz and 55 MHz for a_0 (n=1) , a_0 (n=3) and s_0 (n=1) modes respectively.

The preceding frequencies permit us to calculate the group velocity Vga_0 according to formula (4.47). We find:

$$Vga_0 = 1.78\ Vpa_0 = 396\ m/s.$$

Using formula (4.43), we can calculate the residual in-plane tension T. First, the plate density ρ has to be estimated through the summation of each density of the plate constituents. From the literature, [7.1], [7.26], $\rho(Si_xN_y) = 3.1$ g/cm^3, $\rho(Pt) = 21.45$ g/cm^3, $\rho(PZT) = 7.4$ g/cm^3, $\rho(SiO_2) = 2.1$ g/cm^3, and we obtain $\rho(plate) = 4.518$ g/cm^3. The plate thickness being 2.16 μm, the in-plane tension is T = 117 N/m, giving a residual tensile stress σ = 54.2 MPa.

This residual tensile stress is 4.4 times smaller than that calculated for membranes of the second generation, which are not passivated with a CVD SiO_2 thin layer. It verifies the fact that CVD SiO_2 is much less stressed than Si_xN_y, and can be used to diminish the residual tensile stress of microbafricated membranes. Furthermore, with a small in-plane tension T of 117 N/m only, the group velocity Vga_0 increased to 1.78 times the phase velocity Vpa_0, approaching thus the limiting value for an unstressed membrane, given by: $Vga_0 = 2\ Vpa_0$. This measurement confirms the fact that the absence of tension in the membrane decreases the phase velocity, while it increases the group velocity. Furthermore, despite the fact that the piezoelectric layer is coated with a 0.9 μm thick CVD SiO_2 passivation, previous results emphasize the possibility of Lamb wave generation.

7.5.3 Influence of the bias voltage and wave reflection

As mentioned in section 7.5.1, the IDT orientation with respect to the bulk silicon edges strongly attenuates spurious reflections. This is clearly visible in Figure 7.52. At 0 V bias, the flexural a_0 frequency response closely resembles that of a characteristic sync function (c.f. formula (5.9), chapter 5). When the bias is 16 V, a gain of 22 dB occurs without the emergence of two main signals as observed for Lamb wave devices of the second generation. The

reflected acoustic beam does not interfere destructively with the signal that propagates in the space separating the IDTs. The jaggedness of the passband is due to high capacitive coupling between external connections.

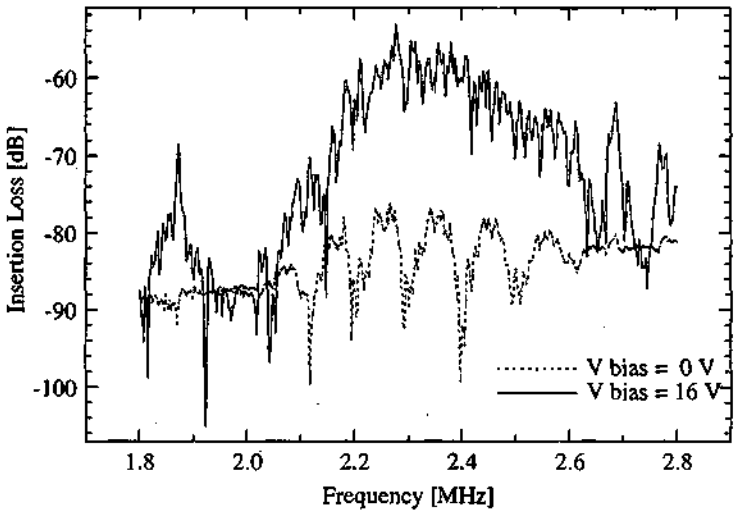

Figure 7.52: Narrow view of the frequency response of a 2.2 μm thick Lamb wave device. An oblique reflection of the backward emitted waves prevents destructive interferences with the forward emitted waves.

7.6 Vacuum loaded FPW device

Lamb waves are very sensitive to mass loading [7.27]. A small change in the characteristic of the acoustic path between the two transducers causes a change in the synchronous frequency. Figures 7.53 (a) and (b) illustrate this change for a device operating first in air (1 bar) and then in vacuum (0.02 mb).

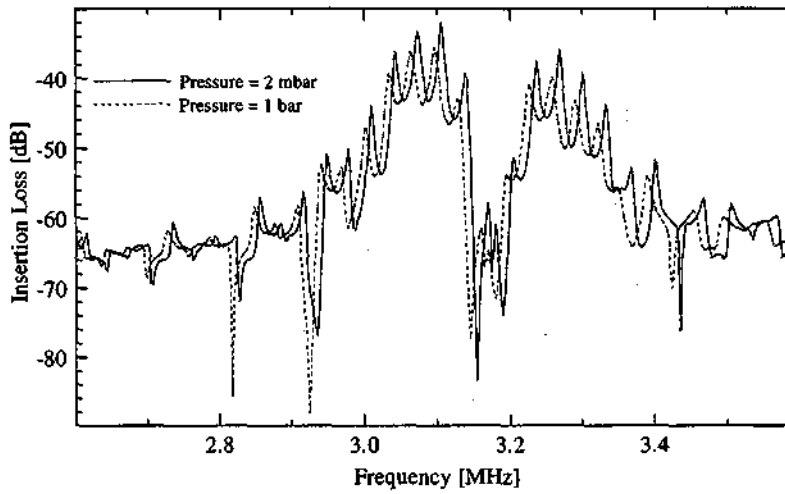

Figure 7.53 (a): Comparison between air loaded and vacuum loaded Lamb wave device. The presence of air on both membrane sides decreases the gain and shifts the entire frequency response to lower values. (b) Narrow view of the signal.

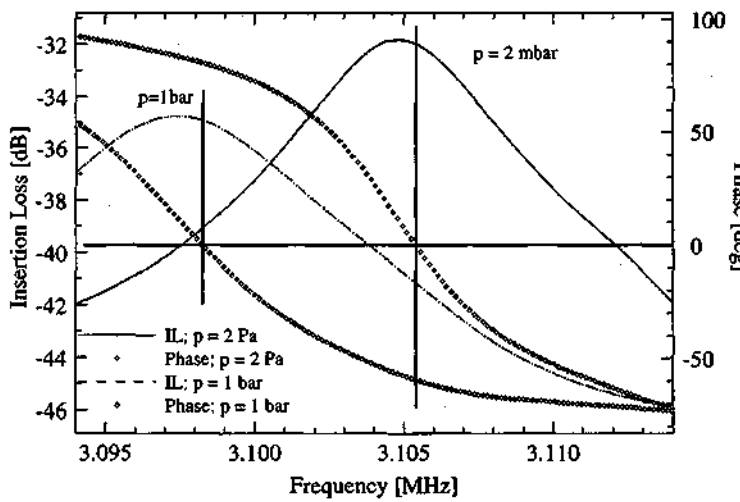

Figure 7.53 (b): Comparison between air loaded and vacuum loaded Lamb wave device. Narrow view of the signal.

During the measurement, both sides of the membrane are in contact with the gas, at the same pressure. Mass loading due to normal air pressure induces a 7.4 kHz frequency shift, and an increase of 3 dB of the insertion loss, compared to the same device operating in vacuum. Table 7.5 summarizes these results.

	vacuum	normal pressure	difference
Insertion loss [dB]	-31.817	-34.752	2.935
Resonant frequency [kHz]	3104.8	3097.4	7.4
Quality factor	554	455	99

Table 7.5: Comparison between air loaded and vacuum loaded Lamb wave device.

In Figure 7.53 (b), for a device operating in vacuum, the frequency of maximal I.L. amplitude does not correspond to the frequency of zero round-trip phase shift: a shift of 600 Hz arises.

Physically, the frequency at which a zero round-trip phase shift occurs represents the frequency eigenvalue ω_0 of an undamped free oscillator. In case of damping, the mechanical resonant frequency ω_r is below the eigenvalue ω_0. The ratio ω_r / ω_0 can be expressed [7.28]:

$$\frac{\omega_r}{\omega_0} = \sqrt{1 - \frac{1}{2Q^2}} \qquad (7.8)$$

where ω_r and ω_0 are the former frequencies and Q the resonance quality factor.

With values of Table 7.5 , the left part (a) of formula (7.8) divided by the right part (b) gives: a/b = 0.9998, indicating that our FPW delay line

operating in vacuum can be considered as a mechanically damped oscillator. The damping is due to residual mass loading and in-plane residual tension. A similar procedure can be applied to an air loaded device.

7.7 Water loaded FPW devices

The effects of fluid charge loading of such membranes with different liquids have been studied by many authors [7.29], [7.30], [7.31], [7.32], [7.33], [7.34], [7.35]. In the following, we restrict our attention to Lamb wave devices having only one membrane side in contact with water.

7.7.1 Frequency responses and gravimetric sensitivity

A typical frequency response is illustrated in Figure 7.54. We see that the antisymmetric a_0 transmitted acoustic signal suffers very little attenuation (2.3 dB) when the back side of the silicon nitride membrane is in contact with a 15-mm high column of deionized water, and that the entire operating band of the transducer is shifted to lower frequencies. In our case, a decrease in frequency as large as 30 % of the initial air loaded resonance frequency is observed.

Strictly speaking, the former 2.3 dB attenuation is mainly due to a decrease of capacitive-coupling noise between input and output IDTs connections. If we consider the amplitude variation of the highest signals in air and in water with respect to the noise variation, it indicates that the lowest order flexural mode a_0 is almost not attenuated due to liquid loading with deionized water.

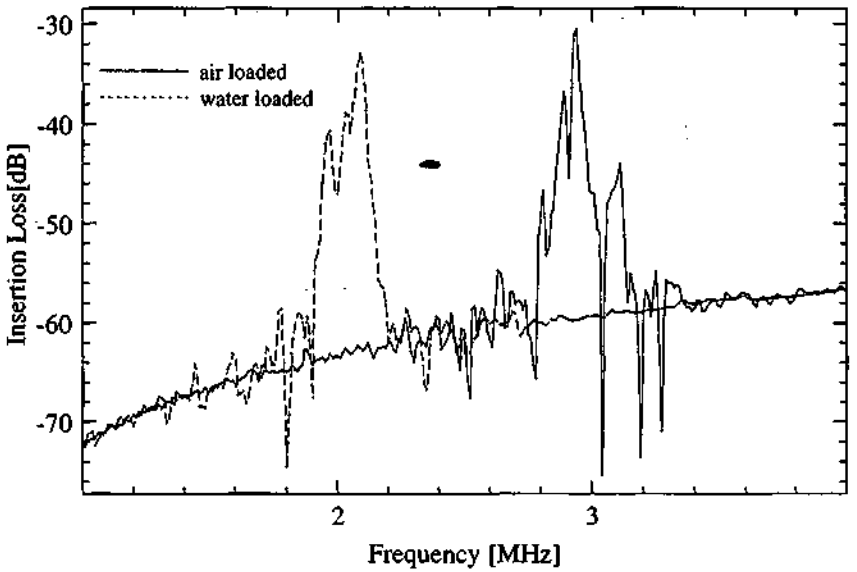

Figure 7.54: Frequency response of the FPW device loaded in air and in water. A frequency shift of 850 kHz and a very small insertion loss variation are observed when the back side of the membrane is in contact with a 15-mm high column of deionized water. Bias is 10 V.

In Figures 7.55-58 several narrowband frequency responses of an air-loaded and water-loaded FPW device are compared, under a bias of 9 V. In 7.55, the entire lower-order propagating mode a_0 (n=1) is strongly shifted to lower frequencies with a small attenuation, while for some frequencies below 2 MHz, which correspond to standing waves, the presence of liquid only attenuates the signal amplitude. Triple-transit-interferences are significantly reduced in the presence of liquid on the membrane. In 7.56 and 7.57, the even (n=2) and odd (n=3) harmonic a_0 modes are translated to lower frequencies and slightly attenuated, while in 7.58, the symmetric mode undergoes a small shift and a low attenuation. These results indicate that the a_0 (n=1) mode is much more sensitive to liquid loading than any other mode [7.36]. Table 7.6 summarizes these results.

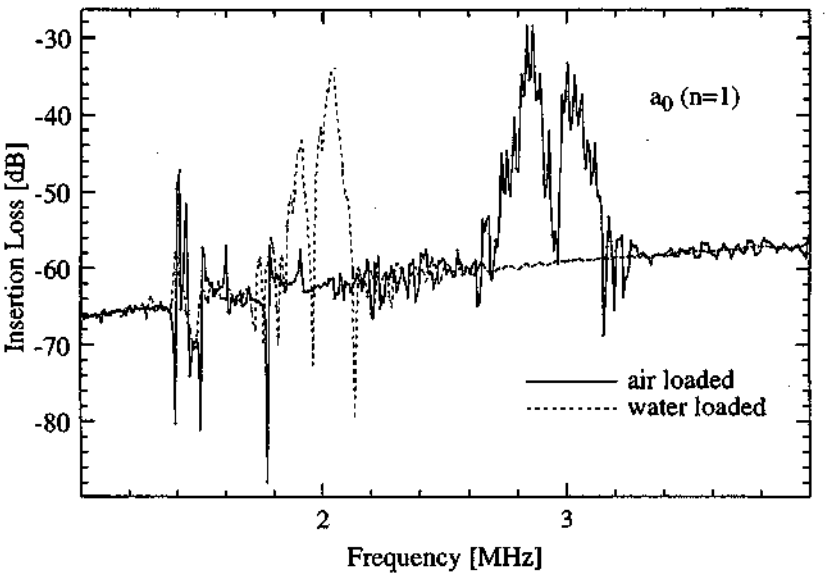

Figure 7.55: Frequency shift and amplitude attenuation for the a_0 (n=1) mode due to liquid loading on one side of the membrane.

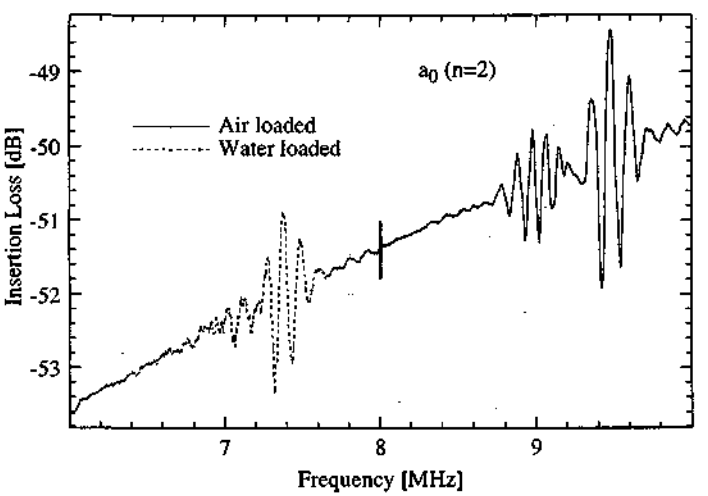

Figure 7.56: Frequency shift and amplitude attenuation for the a_0 (n=2) mode due to liquid loading on one side of the membrane.

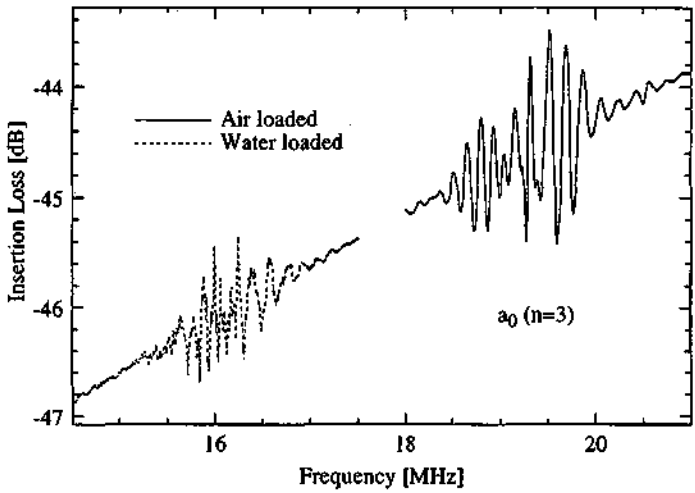

Figure 7.57: Frequency shift and amplitude attenuation for the a_0 (n=3) mode due to liquid loading on one side of the membrane.

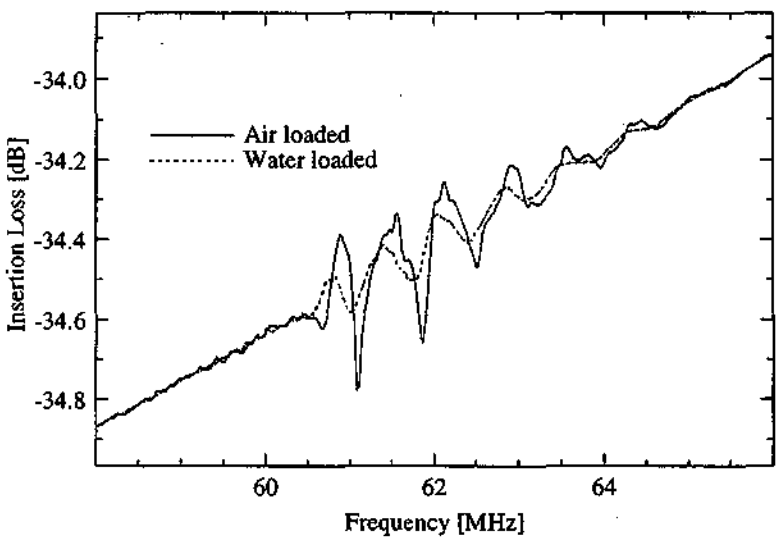

Figure 7.58: Frequency shift and amplitude attenuation for the s_0 (n=1) mode due to liquid loading on one side of the membrane.

Wave type	Air loaded device Synchronous frequency [MHz]	Water loaded device Synchronous frequency [MHz]	Fractional frequency shift Δf/f	Amplitude attenuation [dB]
a_0 (n=1)	2.8375	2.035	0.28	3.9
a_0 (n=2)	9.480	7.375	0.22	1.22
a_0 (n=3)	19.515	16.240	0.17	0.76
s_0 (n=1)	62.120	62.040	0.0013	0.23

Table 7.6: Comparison between air-loaded and water-loaded Lamb wave device.

If we neglect the tension effects, i.e. the variation of frequency with hydrostatic pressure (differential pressure), the fractional frequency shift Δf/f due to the added mass per unit area Δm_{fluid} when a fluid is in contact with the membrane, is proportional to the gravimetric sensitivity $(S_m)_{fluid}$, which can be expressed, according to [7.37], as

$$(S_m)_{fluid} = \left(\frac{\Delta f}{f}\right)\frac{1}{\Delta m_{fluid}} = -\frac{1}{2\left(M + \rho_{fluid}\delta\right)} \qquad (7.9)$$

where M is the mass per unit area of the composite membrane, ρ_{fluid} the fluid density and δ the decay length of the evanescent acoustic field in liquid. For a wavelength of 100 μm, this evanescent decay distance is 16 μm in water [7.38].

For our FPW device, the theoretical value of the mass sensitivity is $(S_m)_{fluid}$ = -179 cm^2/g (calculated with M=11.9· 10^{-3} kg/m^2 and δ=16μm). This

suggests that our FPW sensor operating at 3 MHz with a short-term instability less than 1 Hz is able to detect a minimum mass change

$$\Delta m_{fluid} = \left(\frac{\Delta f}{f}\right) \frac{1}{(S_m)_{fluid}} \qquad (7.10)$$

of the order of 1 ng/cm^2.

7.7.2 Impulse response

In order to use the FPW device as an active component for microfluidic applications such as a micropump, the FPW impulse response was measured with the backside cavity of the membrane filled with a drop of water. Comparison between air-loaded and water-loaded impulse response are shown, respectively, in Figures 7.59-60.

In air, the delay time is 9.03 μs, corresponding to a group velocity of 388 m/s. In water, the delay time increases to 10.60 μs, while the group velocity decreases to 330 m/s. This attenuation for the lowest-order flexural motion in the presence of a liquid on a very thin membrane, is considered to be dependent on the ratio between the fluid and the plate density [7.39]. In our case, this ratio is 0.16. For a propagating wave without any loss into the fluid, this ratio would be close to zero. These measurements confirm the possibility of operating FPW devices in liquids.

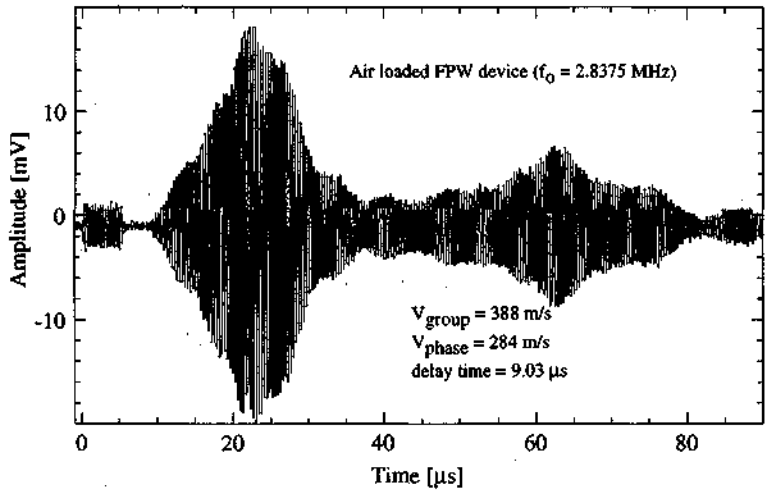

Figure 7.59: Air-loaded FPW impulse response.

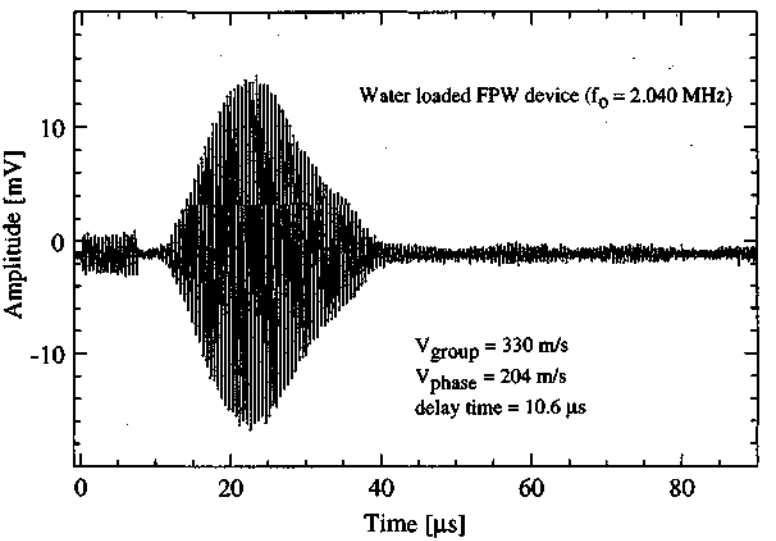

Figure 7.60: Water-loaded FPW impulse response.

7.7.3 Real time frequency shift visualization due to liquid evaporation on the membrane

When one side of the membrane is in contact with water, an important shift of the passband occurs. This property can be used to observe how the gradual evaporation of a thin liquid layer evolve with time.

Figures 7.61-66 highlight this experiment. In (61), the form of the device passband for the flexural a_0 (n=1) mode is given before and after contacting the liquid. As long as the thickness of the liquid layer on the membrane is greater than the evanescent decay length, nothing happens. In (62), the evaporation starts progressively. In (63), no liquid is present on the acoustic path *between* the two IDTs, but both transducers and the membrane edges are still covered by the liquid.

It is interesting that the evaporation does not simply shift the passband, but first decreases the acoustic amplitude and only after, shifts the frequency response. These mechanics emphasize the fact that only a small layer thickness is involved to move the passband (i.e. the decay length).

In (64) the liquid is removed everywhere, except along the edges due to surface tension. This residual liquid absorbs spurious reflections, and prevents destructive interferences. In (65), the liquid is progressively removed along the edges. Finally, in (66), evaporation is complete.

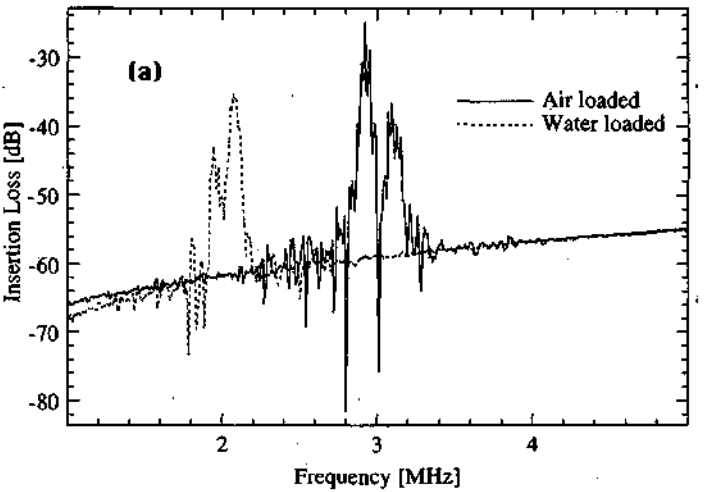

Figure 7.61: Evaporation of a thin liquid layer on the membrane. See text for details.

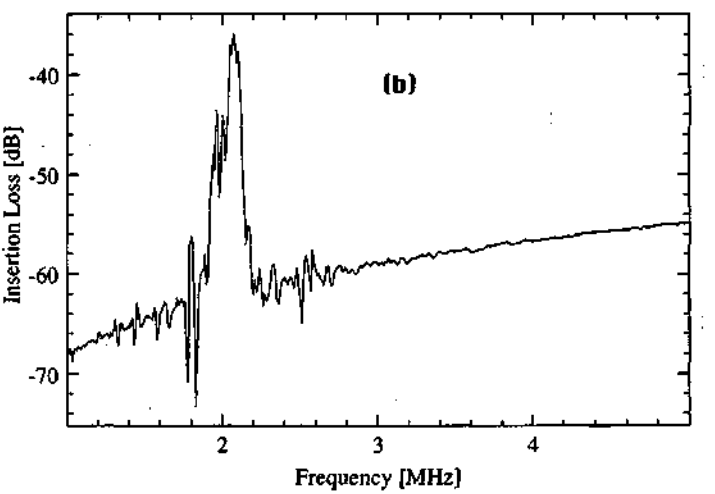

Figure 7.62: Evaporation of a thin liquid layer on the membrane. See text for details.

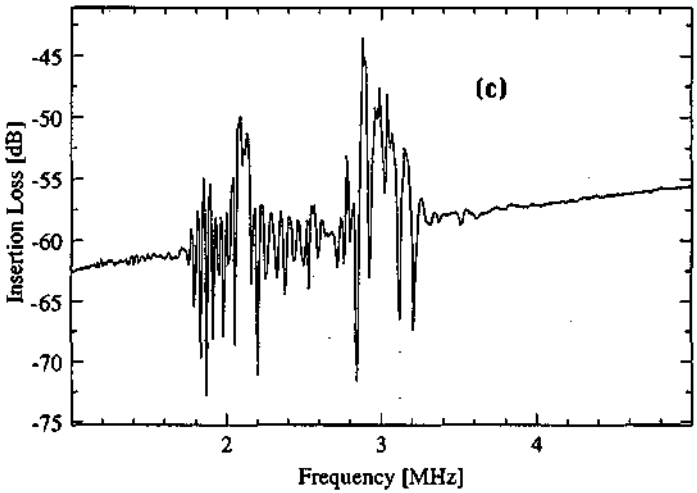

Figure 7.63: Evaporation of a thin liquid layer on the membrane. See text for details.

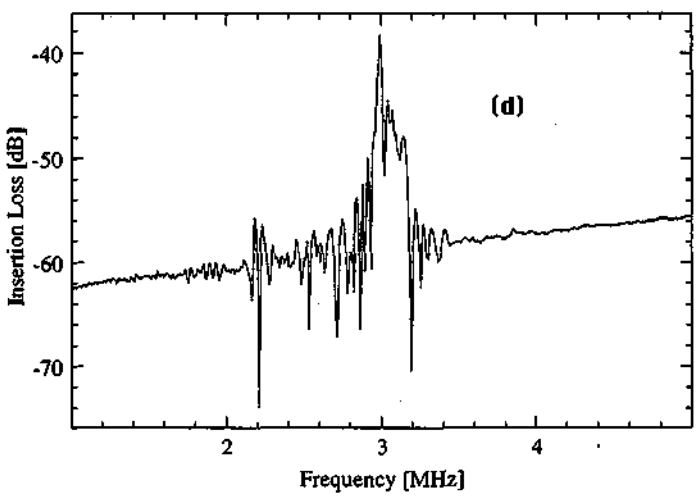

Figure 7.64: Evaporation of a thin liquid layer on the membrane. See text for details.

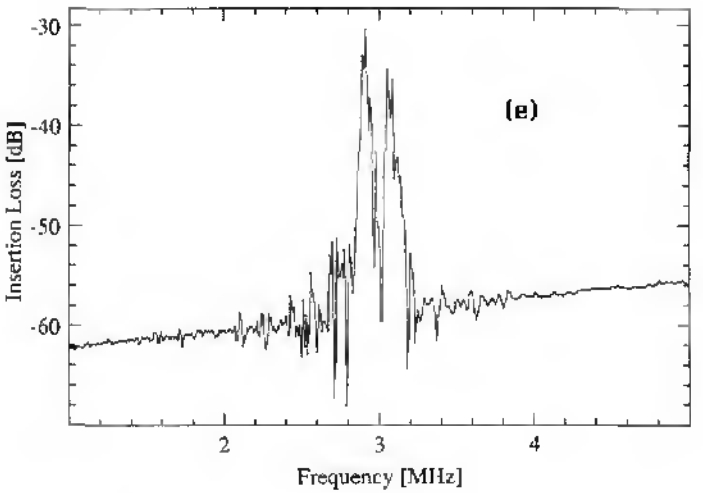

Figure 7.65: Evaporation of a thin liquid layer on the membrane. See text for details.

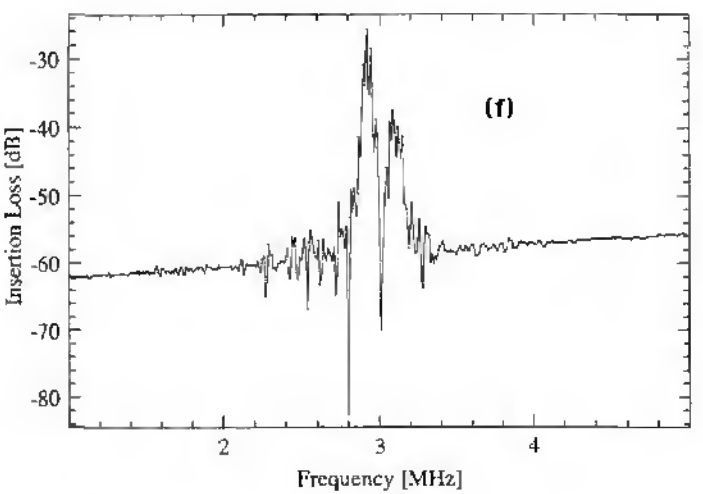

Figure 7.66: Evaporation of a thin liquid layer on the membrane. See text for details.

7.8 Mass transport and micropump

7.8.1 Trapping of granular solids

Figure 7.67 (a) shows the back side of the membrane with two IDTs not energized. A 75-μm glass sphere is located between the two IDTs. A bias of 10-V d.c. increases significantly the stress under every IDTs finger pair so that the transducers are clearly visible. In Figure 7.67 (b), the microsphere is trapped in a nodal region of the membrane. By slowly changing the frequency, the trapped bead can jump forward and backward into another "nodal hole" (see Figures 7.68 and 7.69). Optical observations also indicate that the trapped particle has a very fast rotary movement.

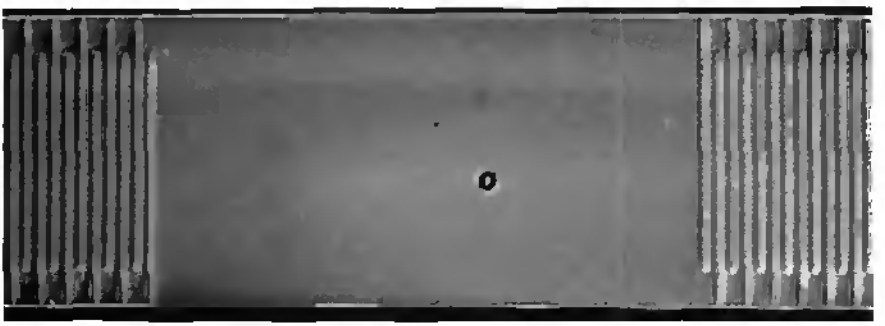

Figure 7.67 (a): Optical views of the backside of the membrane using the Nomarski method. Induced stress under the IDTs fingers due to 10 V_{bias} without r.f. excitation.

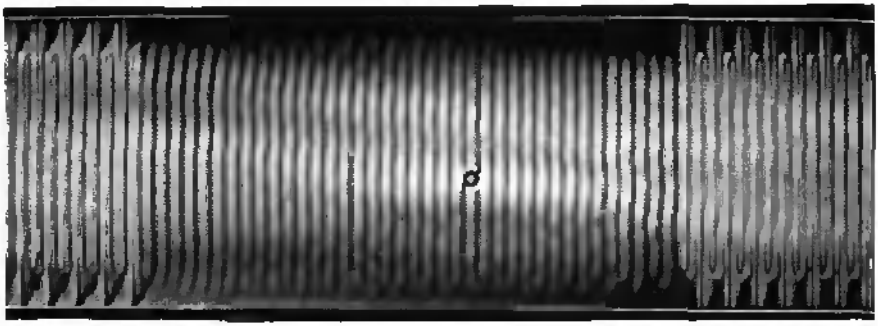

Figure 7.67 (b): Optical views of the backside of the membrane using the Nomarski method. A 75-μm glass sphere is trapped between the two transducers when they are activated.

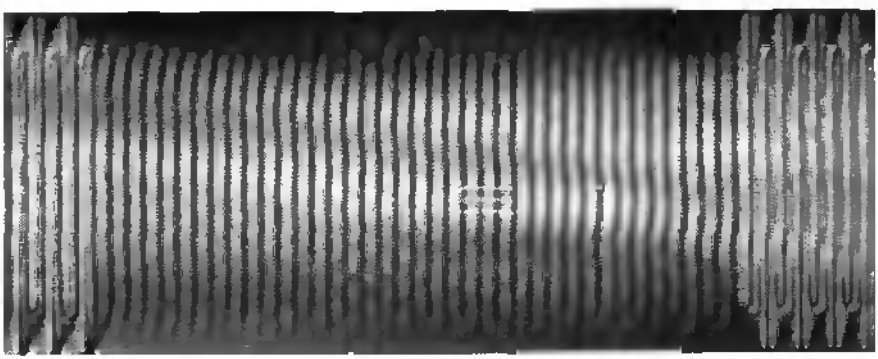

Figure 7.68: Micrograph of standing Lamb waves. A 75-μm glass bead jumps forwards and backwards between two nodal lines.

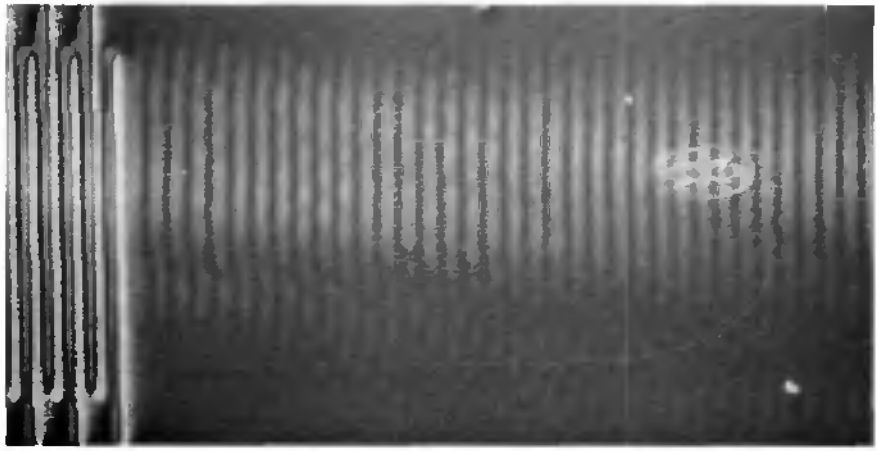

Figure 7.69: Optical view of a 75-μm particle moving rapidly along a circular path on the membrane.

7.8.2 Mechanical transport of granular solids

The mass translational properties of the PZT acoustic delay line is investigated by observing the physical translation of glass microspheres (Duke Scientific) across the surface of the membrane. Figures 7.70 and 7.71 illustrate these observations. A sequence of five successive video frame captures is presented in Figure 7.70. The FPW actuator is placed IDT-side down under the recording setup. A small amount of granular solids of different sizes (10- and 75-μm) were placed on the membrane in the etched silicon well. At time t=0 s, the major part of the microspheres is located near the left end of the membrane. By activating continuously the left transducer (not visible on the picture), which has a bidirectional power flow, a set of microballs moves quickly to the right end of the acoustic channel, while the other particles are moving to the left. It was observed, that some particles cross the entire membrane length during a time shorter than the measuring interval of 0.040 s

between two frame captures, implying a microbead velocity greater than 20 cm/s.

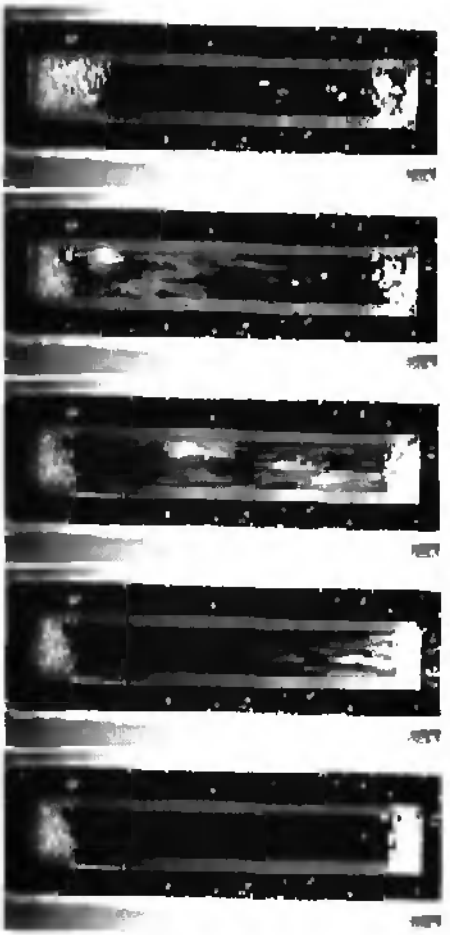

Figure 7.70: Optical views of the mechanical transport of granular solids induced by the lowest a_0 Lamb mode in the membrane. At time t = 0 s (top picture) the major part of the glass beads having different sizes is located in the left. The microspheres are moving from the left to the right. The membrane length is 8 mm. With a measuring interval of 0.040 s between each frame capture, it is found that the faster particles have a velocity greater than 20 cm/s.

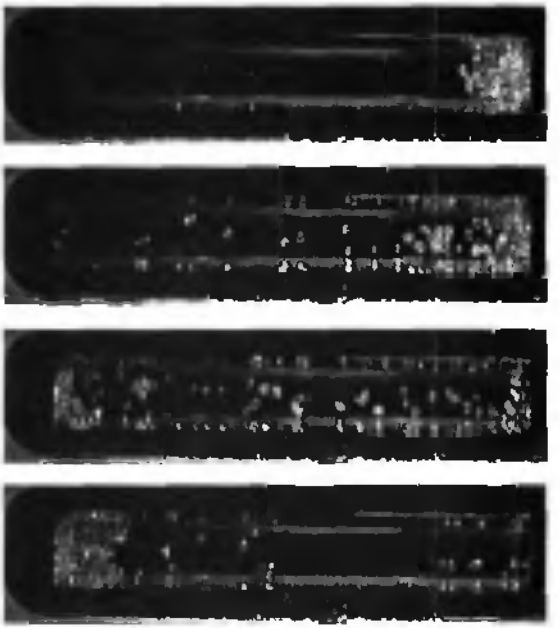

Figure 7.71: Sequence of four video frame captures showing the displacement of different sized particles (50 to 220 μm wide). In this case, the microspheres are moving from the right to the left. At time t = 0 s (top picture) the major part of the glass beads having different sizes is located in the right. The interval between each frame capture is 160 ms.

7.8.3 Micropositioning of a single microsphere

In order to have a better control of the particles motion, only one particle sphere was deposited on the piezoelectric layer. Figure 7.72 shows the movement of a single 75 μm glass sphere across the surface of the membrane between the two transducers. Each picture shows the displacement of the sphere after a burst of 1500 shots at 3.85 MHz with 7 V DC bias and 8 V_{pp} excitation.

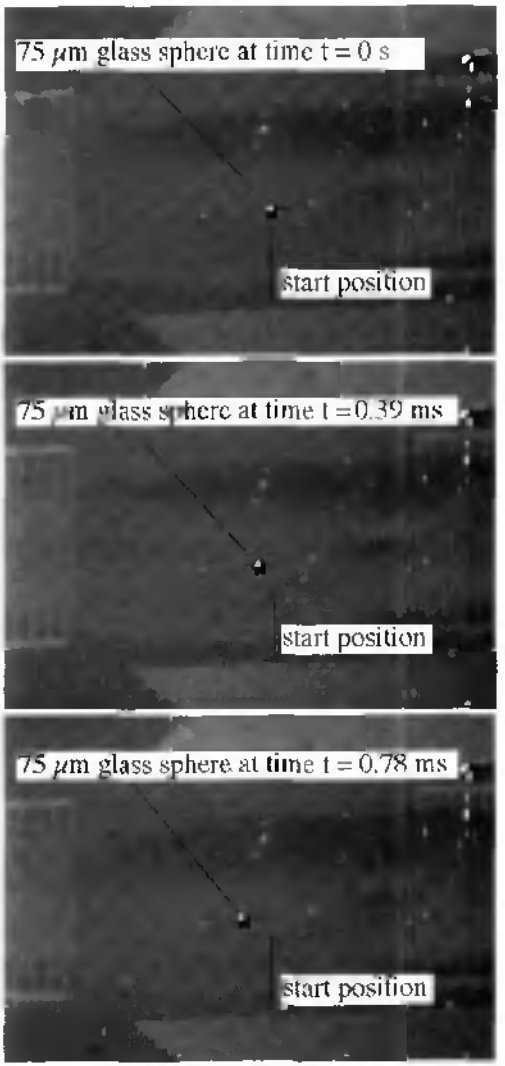

Figure 7.72: Optical views of the mechanical microtransport of a single 75 μm glass sphere induced by the lowest a_0 Lamb mode in the membrane. The excited transducer is located to the right. Each view shows the displacement of the particle after a burst of 1500 shots at 3.85 MHz with 7 V_{bias} and 8 V_{pp} excitation. A measuring displacement of 100 μm after one burst indicates that the velocity of the sphere is 25 cm/s.

In this case, if we neglect inertial effects due to the mass, the average displacement after one burst is 100 μm, indicating that the velocity of the sphere is 25 cm/s. By varying the burst rate and the burst length, it was possible to move the single particle in both directions and to achieve controlled small displacements with high accuracy and short time response.

This kind of device provides a very useful method to manipulate and characterize single small particles of only a few microns size and should also be suitable for biological purposes like living cell trapping and cell manipulating applications. A FPW actuator is also suitable for injecting sequentially small quantities of particles in an on-line monitored device requiring fast time response and precise mass transfer control.

7.8.4 FPW sensitive mass filter

Separation of solid particles having different sizes (50 to 250 μm wide) along the surface of the membrane was achieved by using the lowest-order flexural a_0 mode (n=1) generated motion. Figure 7.73 exhibits a sequence of three video frame captures using a high-speed shutter. Two glass microspheres of different sizes were placed on the membrane. At time t=0 s, the particles are located near the right edge of the suspended membrane. The IDT (not visible) is on the backside of the membrane, just under the two glass beads. A continuous a.c. voltage excitation of 6 V_{pp} applied to the IDT moves the particles from the right to the left. After 0.080 s, we observe that the two particles are completely separated. This occurs due to different inertia of the beads.

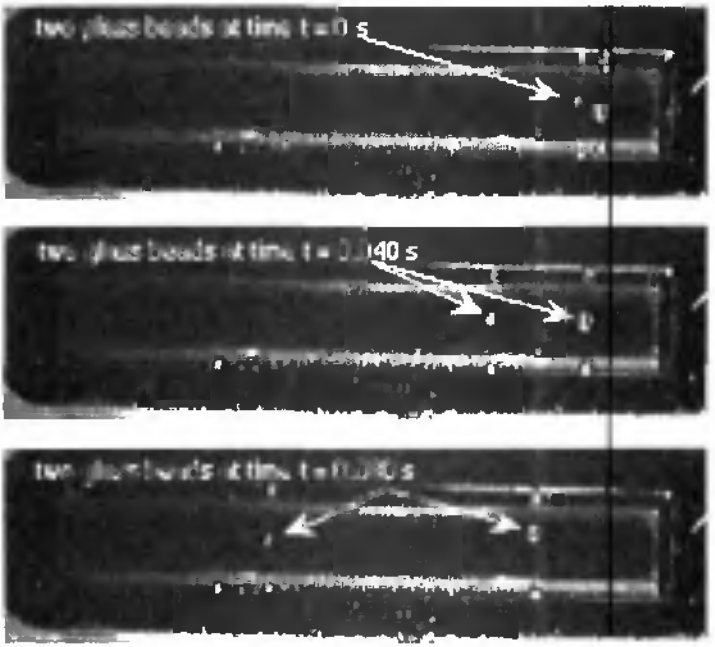

Figure 7.73: Sequence of three video frame captures, illustrating the separation of two different sized particles at the resonance frequency of 2.952 MHz. The driven IDT is on the right, on the backside of the membrane. After 0.080 s the two particles are completely separated.

Figures 7.74 and 7.75 illustrate respectively the measured displacements of two different glass microspheres as a function of the burst length and the amplitude of the burst excitation at the resonance frequency. This points to the possibility of using Lamb-wave devices as a sensitive mass filter.

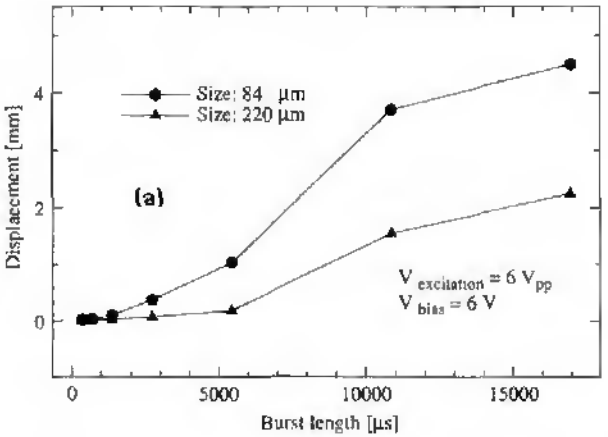

Figure 7.74: Displacement of two different sized glass beads actuated by a FPW actuator for several burst lengths at the resonance frequency of 2.952 MHz.

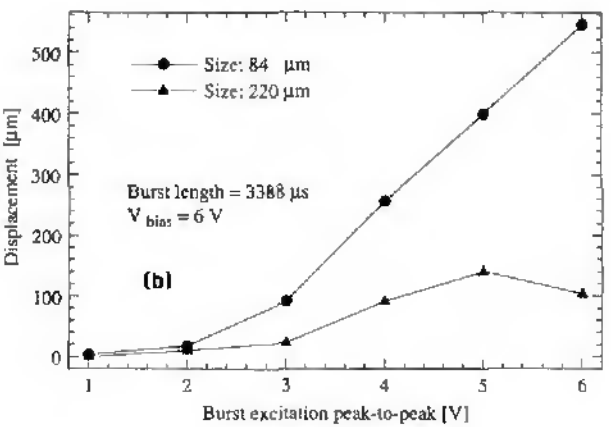

Figure 7.75: Displacement of two different sized glass beads actuated by a FPW actuator for several burst amplitudes at the resonance frequency of 2.952 MHz.

7.8.5 Liquid loading and pumping

Fluidic transport of suspensions is a universal and extremely important part of fluidic control. Liquid suspensions of solid particles are used in chemical (bio)reactors, colloidal chemistry, drug delivery and microfluidic applications.

In order to study the flow profiles and the liquid flow rates achieved with our FPW actuators, three configurations of the liquid in contact with the vibrating membrane were tested. First, the 380 μm deep silicon flow channel was filled with deionized water that contained 3 μm polystyrene microspheres, and 10 and 75 μm glass spheres, without covering the liquid with a glass slide. Secondly, the liquid was confined near the membrane by using a transparent cover piece that filled the silicon well, except for the 40 μm over the activated membrane. Finally, a cover piece was placed with an inlet and an outlet connected to silicone tubes.

In the first case, a global rotatory movement is created in the moving liquid with a flow velocity depending on the depth in the channel. For 10 μm spheres moving close to the membrane, the average velocity is 250 μm/s. In this configuration, the creation of two or three narrow channels along the membrane length (see Figure 7.76) was also observed. For 10 μm glass particles moving along these channels, a velocity higher than 1.6 cm/s was measured, which is much more than the predicted value of 600 μm/s for the liquid only [7.40].

These intriguing narrow channels emphasize the fact that the flow profile across the FPW-driven plate is not uniform but suffers strong irregularities. On the other hand, for solid particles having a density higher than the moving liquid, one can expect that their velocity will differ from that of the fluid.

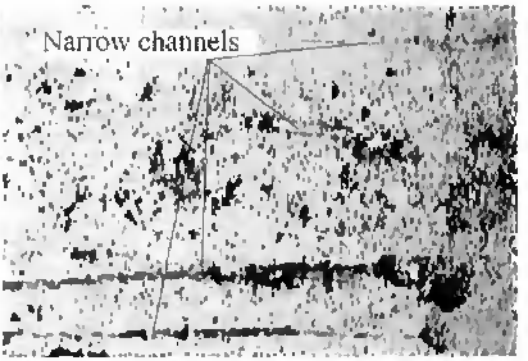

Figure 7.76: Optical view of liquid loading with solid particles. The driven transducer (not visible on the picture) is located to the left end of the membrane. Liquid moves from the left to the right. Four narrow channels are created where the measured velocity for 10 µm glass spheres is higher than 1.6 cm/s.

In the two last cases, silicon wells having the same profiles as the FPW actuators but with 340 µm depth instead of 380 µm, were fabricated, and filled with UV cured epoxy with or without the two inlet and outlet apertures, depending on the use. After polymerization under UV light and N_2 flow rate, these cover pieces were released from the silicon matrix and carefully deposited on FPW membranes (see Figure 7.78). In order to avoid pressure loss around the contact area, these structures were sealed with silicone glue. This method allows the fabrication of driven flow channels having a trapezoidal cross section and a well controlled thickness of only a few µm. Figure 7.77 shows a schematic view of a first FPW micropump with inlet and outlet apertures that are perpendicular to the membrane and connected to silicone tubing having a 0.508 mm internal diameter. From a practical point of view, it was necessary to prove that such a planar driven flow channel over the flexural piezoelectric membrane, can induce an observable flow rate in the silicone tubes.

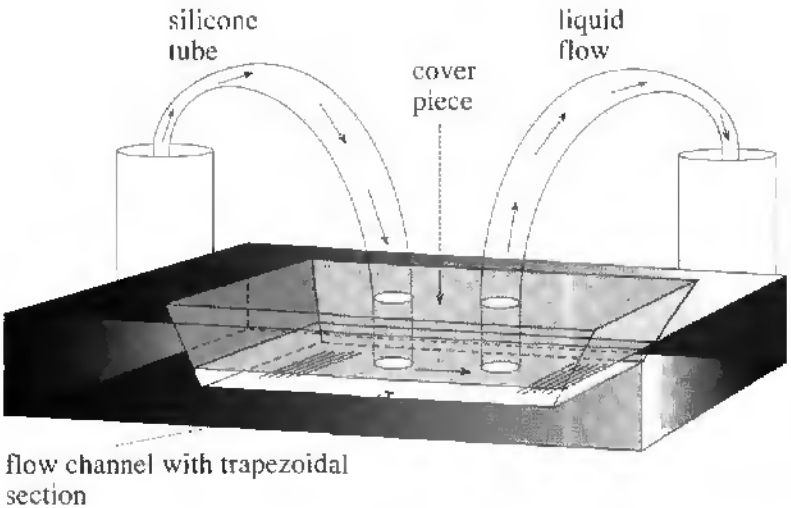

Figure 7.77: Schematic view of a FPW micropump having inlet and outlet apertures and a cover piece to confine the liquid close to the driven membrane. The flow channel has a well-controlled thickness of only a few micrometers in order to induce a flow rate in the silicone tubes. A flow rate of 0.25 µl min^{-1} was achieved with such a micropump prototype.

Figure 7.78: Micrograph of the micromachined cover piece which confines the liquid close to the membrane in the FPW micropump. The inlet and outlet tubes allow connection to small bottles filled with water.

The silicone tubes having a length of 9 cm were entirely filled with a colored solution of water containing polymer microspheres of 3.2 μm size, and their ends were then attached into small filled bottles. In this way, the liquid could flow into the tubes without being stopped by the surface tension that would appear between air and liquid, in the case of partially filled tubes. Both liquid levels in the two storage bottles were carefully adjusted to be equal. With this configuration, we have recorded fluid motion in the silicone tubes, that was only produced by the flexural wave, at a distance of 4 cm away from the driven membrane.

The measured fluid flow velocity was 21 μm/s giving an average flow rate of 0.25 μl/min. By elevating a few mm one storage bottle, the flow rate was totally inverted in the tubes but not in the driven flow channel. Close to the membrane, the driven transducer was able to force the liquid to move in the initial direction, although an additional flow was created near the cover piece in the opposite direction due to gravity, at a distance of 40 μm above the membrane.

This superposition of two flow rates in opposite directions close to the membrane, confirms the fact that a flexural plate wave propagating in the membrane produces an evanescent disturbance in the fluid that will extend to a distance of only a few μm.

Therefore, it seems possible to obtain a better flow rate in the silicone tube with an useful pressure difference between inlet and outlet for practical applications, by using a liquid confinement closer to the membrane, that is at a maximal distance in the order of the evanescent decay length.

7.9 References:

[7.1] Ph. Luginbuhl, S. D. Collins, G.-A. Racine, M.-A. Grétillat, N. F. de Rooij, K. G. Brooks, and N. Setter, "Microfabricated Lamb Wave Device Based on PZT Sol-Gel Thin Film for Mechanical Transport of Solid Particles and Liquids", *Journal of Microelectromechanical Systems*, Vol. 6, N0. 4, December 1997, pp. 337-346.

[7.2] Ph. Luginbuhl, S. D. Collins, G.-A. Racine, M.-A. Grétillat, N. F. de Rooij, K. G. Brooks, and N. Setter, "Flexural-Plate-Wave Actuators Based on PZT Thin Film", *Proceedings IEEE Micro Electro Mechanical Systems*, MEMS 1997, Nagoya, Japan, January 26-30, 1997, pp. 327-332.

[7.3] Ph. Luginbuhl, S. D. Collins, G.-A. Racine, M.-A. Grétillat, N. F. de Rooij, K. G. Brooks, and N. Setter, "Ultrasonic flexural Lamb-wave actuators based on PZT thin film", *Sensors and Actuators* A 64, 1998, pp. 41-49.

[7.4] Y. Xu, "Ferroelectric Materials and Their Applications", Amsterdam: North-Holland, 1991.

[7.5] R. Inaba, Y. Kasahara and K. Wasa, "An electrostatic voltage sensor using surface acoustic waves", *IEEE 1982 Ultrasonics Symp.*, San Diego, CA, Dct. 27-29, 1982, pp.312-316.

[7.6] S. G. Joshi, and B.B. Dasgupta, "Electronically variable surface acoustic wave time delay using a biasing electric field", *IEEE 1981 Ultrasonic Symp.*, Chicago, IL, USA, Oct. 14-16, 1981, pp.319-323.

[7.7] *E.* Gatti, A. Palma, and *E.* Verona, "A surface acoustic wave voltage sensor", *Sensors and Actuator*, 4, 1983, pp. 45-54.

[7.8] A. Fransen, G. W. Lubking, and M. J. Vellekoop, "High-resolution high-voltage sensor based on SAW", *Sensors and actuators* A 60, 1997, pp.49-53.

[7.9] M. Ishido, "Acoustic-wave-based voltage sensors", *Sensors and actuators* A 44, 1994, pp.183-189.

[7.10] M. J. Vellekoop, "An integrated SAW voltage sensor", *IEEE 1988 Ultrasonic Symp.*, Chicago, IL, USA, Oct. 2-5, 1988, pp. 575-578.

[7.11] K. Toda, and K. Mizutani, "A Lamb wave voltage sensor", *J. Acoust. Soc. Am.* 74 (3), September 1983, pp. 677-679.

[7.12] S. W. Wenzel, and R. M. White, "Silicon-Based Ultrasonic Lamb-Wave Multisensors", *IEEE 1988 Ultrasonic Symp.*, Chicago, IL, USA, Oct. 2-5, 1988, pp. 27-30.

[7.13] B. Wild, F. Wolf, and R. Wagner, "Der Zeitverlauf der Polarisation von polykristallinem Bariumtitanat", *Phys. Blätter* 16, 1960, pp. 164-168.

[7.14] A. Kholkin, E. Colla, K. Brooks, P. Muralt, M. Kohli, T. Maeder, D. Taylor, and N. Setter, "Interferometric study of piezoelectric degradation in ferroelectric thin films", *Microelectron. Eng.*, vol. 29, 1995, pp. 261-264.

[7.15] W. L. Warren, D. Dimos, and R. M. Waser, "Degradation mechanisms in ferroelcetric and high-permittivity perovskites", MRS (Material Research Soc.) Bull., vol 21, no. 7, July 1996, pp. 40-45.

[7.16] G. Teowee, C. D. Baertlein, E. A. Kneer, J. M. Boulton, and D. R. Uhlmann, "Effect of top metallization on the fatigue and retention properties of sol-gel PZT thin films", *Integrated Ferroelectrics*, vol. 7, 1995, pp. 149-160.

[7.17] W. P. Mason, J. Acoustic. Soc. Am. 27 (1955) 73.

[7.18] Y. Xu, "Ferroelectric Materials and Their Applications", North-Holland, Amsterdam, 1991.

[7.19] Technical Information, Nikon Corporation, 1995

[7.20] A. A. Nassar, and E. L. Adler, "Propagation and electromechanical coupling to plate modes in piezoelcetric composite membranes", *Proc. IEEE Ultrasonics Symp.* Atlanta, G.A., 1983, pp. 369-372.

[7.21] S. W. Wenzel, "Application of ultrasonic Lamb waves", Philosophical Dissertation, University of California, Berkeley, 1992.

[7.22] O. Tabata. K. Kawabata, S. Sugiyama, and I. Igarashi, "Mechanical Property Measurements of Thin Films Using Load-Deflection of Composite Rectangular Membranes", *Sensors and Actuators*, 20, (1989) pp. 135-141.

[7.23] V.Z. Kresin, and S. A. Wolf, "Fundamental of Superconductivity", Plenum Press, New York, 1990, ch. 3.

[7.24] M. Akinaga, H. Fukuda, H. Ohkubo, T. Fukami, and T. Aomine, "Surface Acoustic Waves in High-T_c Superconducting Thin Films on Piezoelectric $PbTiO_3$ Films", *Jpn. J. Appl. Phys.* Vol. 31 (1992) pp. 2978-2981.

[7.25] H.-P. Baum, B. K. Sarma, M. Levy, J. Gavaler, and A. Hohler, SAW measurements on a Nb film and an $YBa_2Cu_3O_7$ film", *IEEE Transactions on Magnetics*, Vol. 27, NO. 2, March 1991, pp. 1280-1283.

[7.26] S. M. Sze, "Semiconductor devices, Physics and Technology", John Wiley & Sons, New York, 1985.

[7.27] S. W. Wenzel, and R. M. White, "Flexural Plate-wave Gravimetric Chemical Sensor", *Sensors and Actuators*, A21-A23, 1990, pp. 700-703.

[7.28] J. Rossel, "Précis de physique expérimentale et théorique", Edition du Griffon, Neuchâtel, Suisse, 1974, pp.185-186.

[7.29] R. D. Watkins, W. H. B. Cooper, A. B. Gillespie, and R. B. Pike, "The attenuation of Lamb waves in the presence of a fluid", *Ultrasonics*, Vol 20, November 1982, pp. 257-264.

[7.30] R. M. White, and S. W. Wenzel, "Fluid loading of a Lamb-wave sensor", *Appl. Phys. Lett.* **52** (20), 16 May 1988, pp. 1653-1655.

[7.31] B. A. Martin, S. W. Wenzel, and R. M. White, "Viscosity and density Sensing with Ultrasonic Plate Waves", *Sensors and Actuators*, A21-A23 (1990) pp.704-708.

[7.32] V. Rajendran, M. Koike, and K. Hashimoto, "Mass density sensor for liquids using ZnO-Film/Al-foil Lamb wave device", *Ultrasonics Symposium*, Tucson, AZ, USA,1992, pp. 263-268.

[7.33] M. J. Vellekoop, G. W. Lubking, P. M. Sarro, and A. Venema, "Evaluation of liquid properties using a silicon Lamb wave sensor", *Sensors and actuators* A, 43, 1994, pp. 175-180.

[7.34] Z. Zhu, J. Wu, J. Li, and W. Zhou, "A general dispersion relation for Lamb-wave sensors with liquid-layer loading", *Sensors and Actuators* A 49, 1995, pp. 79-84.

[7.35] B. J. Costello, S. W. Wenzel, and R. M. White, "Density and viscosity sensing with ultrasonic flexural plate waves", *The 7th International Conference on Solid-State Sensors and Actuators*, pp. 704-707.

[7.36] J. Wu, and Z. Zhu, "sensitivity of Lamb Wave Sensors in Liquid Sensing", *IEEE Transactions on Ultrasonics, Ferroelectrics, and Frequency Control*, Vol. 43, N0.1, January 1996, pp. 71-72.

[7.37] S. M. Sze, "Semiconductor Sensors", Wiley, New York, 1994, ch. 3, pp.97-151.

[7.38] B. J.Costello, B. A. Martin, and R. M. White, "Ultrasonic plate wave for biochemical measurements", *Proc. IEEE Ultrasonics Symp.*, Montreal, Canada, Oct. 1989, pp. 977-981.

[7.39] H. Dabirikhah, and C. W. Turner, "Anomalous Behaviour of flexural waves in very thin immersed plates", *Proc. Ultrasonics Symp.*, Tucson, AZ, USA, 1992, pp. 313-317.

[7.40] C. E. Bradley, and R. M. White, "Acoustically driven flow in flexural plate wave devices: Theory and experiment", *Proc. IEEE Ultrasonics Symp.*, 1994, pp. 593-597.

1436

8. Conclusion

In this work, studies of cantilever beams and ultrasonic Lamb-wave devices based on PZT thin films have been presented. The most important part concerns Flexural-Plate-Wave (FPW) devices, with related acoustic theory, their design, fabrication, characterization, and finally the experimental results.

Concerning piezoelectric beams, interferometric displacement measurements, electrical measurements and finite element simulations have been done to determine some piezoelectric properties of these beams actuated by PZT sol-gel thin films.

In the linear domain of the piezoelectric film, experimental results yield a transverse coefficient d_{31}= -24.72·10^{-12} C/N for interferometric measurement and d_{31} = -22.34 10^{-12} C/N for electrical measurement which are close to the value d_{31} = -21.4·10^{-12} C/N obtained from the finite element calculations. In the saturation domain the d_{31}^{sat} value obtained is about 35 % of the reported value for bulk ceramics.

From experimental data the initial stress of the beam induced an apparent poling voltage of 2.8 V. However simulations based on a thermal mismatch effect leads to a higher shifting value of 5.6 V, indicating that this virgin permanent polarization of the PZT film is due to another process dependent effect.

Finally, the measured and calculated frequencies for different modes of the beam are in very good agreement.

Concerning ultrasonic Lamb waves, demonstration of the feasibility of fabricating Flexural-Plate-Wave acoustic transducers using PZT sol-gel thin film as the piezoelectric layer has been presented. The use of PZT provides a stronger piezoelectric coupling and generally produces higher acoustic powers than zinc oxide (ZnO) or aluminium nitride (AlN). However, for the PZT films, a d.c. bias is required to obtain maximum efficiency, and fatigue occurs with extended use. Further improvements of the PZT film are thus required.

The acoustic delay line of air-loaded devices resulted in phase velocity between 286-312 m/s with a group velocity 1.31 to 1.54 times the phase velocity. A theoretical gravimetric sensitivity $(Sm)_{fluid}$ = -179 cm^2/g was calculated for the device loaded with water, suggesting that the minimum measurable mass change Δm_{fluid} on the membrane is of the order of 1 ng/cm^2.

Various measurements (e.g. polarization, voltage sensor, optical wave pattern visualization, edge reflections, acoustic attenuation...) have been performed to emphasize the diversity of use of such acoustic waves. Comparison between theoretical predictions and measured values shows a good agreement.

A method to determine the residual in-plane tension of composite suspended membranes by measuring only the frequency of propagating harmonic Lamb modes was presented and offers many interesting potential applications (e.g. to study the frequency shift related to the phase transition between normal and superconducting states of thin films deposited on the membrane).

Mechanical transport of small quantities of granular solids with velocities greater than 20 cm/s has been observed. The microtransport and micropositioning of a single 75 μm particle size having velocity up to 25 cm/s

was demonstrated, providing a very useful method to manipulate small particles of only a few microns size. The possibility of using Lamb waves to separate particles of different mass has been achieved and indicates the use of FPW devices as sensitive mass filters.

Liquid loading with solid microspheres was achieved with an average velocity of 250 μm/s. A velocity higher than 1.6 cm/s was also observed for 10 μm glass spheres in the liquid along narrow channels.

The possibility of using a FPW actuator for pumping liquid in silicone tubes with a flow rate up to 0.255 μl/min at a distance of 4 cm from the driven membrane has been demonstrated. Increase of this flow rate and of the pressure difference between inlet and outlet apertures, should be possible by confining the liquid closer to the membrane.

These very promising results emphasize the great potential of Flexural-Plate-Wave devices based on PZT sol-gel thin film in sensor, mass transport and fluid delivery systems.

1436

List of Publications

Ph. Luginbuhl, G.-A. Racine, Ph. Lerch, B. Romanowicz, K.G. Brooks, N. F. de Rooij, Ph. Renaud, and N. Setter, "Piezoelectric cantilever beams actuated by PZT sol-gel thin film", *Sensors and Actuators* **A 1-3**, 530-35 (1996).

Ph. Luginbuhl, S. D. Collins, G.-A. Racine, M.-A. Grétillat, N. F. de Rooij, K. G. Brooks, and N. Setter, "Microfabricated Lamb Wave Device Based on PZT Sol-Gel Thin Film for Mechanical Transport of Solid Particles and Liquids", *Journal of Microelectromechanical Systems*, Vol. 6, N0. 4, December 1997, pp. 337-346.

Ph. Luginbuhl, S. D. Collins, G.-A. Racine, M.-A. Grétillat, N. F. de Rooij, K. G. Brooks, and N. Setter, "Ultrasonic flexural Lamb-wave actuators based on PZT thin film", *Sensors and Actuators* A 64, 1998, pp. 41-49.

G.-A. Racine, R. Luthier, Ph. Luginbuhl, K. G. Brooks, N. Setter, and N. F. de Rooij, "Hybrid ultrasonic elastic force motor micromachined in silicon", *Integrated Ferroelectrics* **8**, 25-34 (1995).

K. G. Brooks, D. Damjanovic, N. Setter, Ph. Luginbuhl, G.-A. Racine, and N. F. de Rooij, "Piezoelectric response of PZT thin film actuated micromachined silicon cantilever beams", Proc. IEEE ISAF'94, pp. 520-22.

K. Brooks, D. Damjanovic, A. Kholkin, I. Reaney, N. Setter, Ph. Luginbuhl, G.-A. Racine, N. F. de Rooij, and A. Saaman, "PZT films for micro-pumps", *Integrated Ferroelectrics* **8**, 13-23 (1995).

P.-A. Clerc, L. Dellmann, F. Grétillat, M.-A. Grétillat, P.-F. Indermühle, S. Jeanneret, M. Koudelka, Ph. Luginbuhl, C. Marxer, T. Pfeffer, G.-A. Racine, S. Roth, P.Thiébaud, and N. F. de Rooij, "Advanced Deep Reactive Ion Etching a Versatile Tool for Micro-Electromechanical Systems", *MME'98, Micromechanics Europe*, June 3-5, 1998, Ulvik in Hardanger, Norway

Conference Proceedings

Ph. Luginbuhl, G.-A. Racine, Ph. Lerch, B. Romanowicz, K.G. Brooks, N. F. de Rooij, Ph. Renaud, and N. Setter, "Piezoelectric cantilever beams actuated by PZT sol-gel thin film", *Transducers'95, Eurosensors IX, Digest of Technical Papers*, Stockholm, Sweden, June 25-29. 1995, pp. 413-416.

Ph. Luginbuhl, S. D. Collins, G.-A. Racine, M.-A. Grétillat, N. F. de Rooij, K. G. Brooks, and N. Setter, "Flexural-Plate-Wave Actuators Based on PZT Thin Film", *Proceedings IEEE Micro Electro Mechanical Systems*, MEMS 1997, Nagoya, Japan, January 26-30, 1997, pp. 327-332.

Ph. Luginbuhl, S. D. Collins, G.-A. Racine, K.G. Brooks, N. Setter and N. de Rooij, "Acoustic-Wave Devices Employing Sol Derived PZT as the Piezoelectric Transducer", *Microfabricated Sensors, Instruments and Systems for Biological and Medical Applications*, May 6-8, 1996, UC Davis Alumni Center, California, USA, 1996, pp. 46-51.

Acknowledgments

I would like to thank Professor Dr. Nico de Rooij who gave me the opportunity of working in his group, for his enthusiastic support and intuitive nature during all the time of this project, and for his many encouragements to do this research and to present this work at different international congresses. Special thanks for his activities, engagements and contributions for the continuous development of the MEMS field of research.

Dr. Georges-André Racine for having introduced me in the clean-room laboratory, for his many explanations and contributions concerning the functioning of various apparatus and the development of processing steps, his help when the Macintosh was "on strike !", our work together and for his helpful suggestions and discussions.

Prof. Dr. Scott Collins from the University of California, Davis, for kindly agreeing to be an examiner of this Ph.D. thesis, for his perceptive comments, suggestions and work during the time he spent in our group. I really appreciated this profitable collaboration and our many discussions about the way to generate accurately the lowest acoustic flexural mode in thin piezoelectric membranes.

P. D. Dr. Damian Twerenbold from the Physics Institute, for kindly agreeing to be an examiner of this Ph.D. thesis and for his comments.

Prof. Dr. Nava Setter at the Swiss Federal Institute of Technology, EPFL, Laboratoire de Céramiques, and her group for having given to me the possibility of using sol-gel deposited PZT thin films.

Dr. Keith Brooks and Dr. Andreas Seifert from EPFL Lausanne, for their valuable collaboration during all the project, their research activities

about the deposition techniques of PZT thin films. Special thanks to K. Brooks for having read the final manuscript, and for his comments and corrections.

Prof. Dr. Philippe Renaud, Dr. Philippe Lerch, and Dr. Bart Romanowicz from EPFL Lausanne, for their collaboration and their FE simulations.

Dr. Marc-Alexis Grétillat, for his generosity in spending a lot of time to explain me many things and specially the art of "Sun's use", to design with me different sets of masks, his valuable suggestions concerning various aspects of the technology and his comments about Lamb waves.

Cynthia Beuret for all her help (e.g. correction of texts, SEM pictures) anf for having supported in the same office "Aladdin's parrot" (!)

Pierre Thiébaud which helped me in the design of mask levels.

Florence Grétillat for our many interesting discussions.

Dr. Lionnel Paratte, always ready to participate and to solve problems.

Dr. Jean-Charles Fiaccabrino for his contribution in the lift-off technique.

Gilles Beljakovic who made a very nice work during his semester project.

Our technical team Pierre-André Clerc, Sylvain Jeanneret, Silviane Pochon, Sabina Jenny and Bastien Droz for their precious assitance.

Dr. Victor Plesski, Dr. Serguei Kondratiev and Dr. Thor Thorvaldsson from Micronas S.A. for helpful discussions about the group velocity of Lamb waves.

Dr. Pierre-François Indermühle (PFI !) for his generosity of making many AFM measures.

Laurent Dellmann and Sylvain Roth ("tovaritch" !) for their help in the use of the hot plate and the realization of nice SEM pictures.

Prof. Dr. Milena Koudelka-Hep for having supported my "agacements !" and Dr. Peter van der Wal who kindly contributed to explain me some mysteries of the chemistry, and both of them for having answered to many of my qestions.

A special thanks to Dr. David Strike which always kindly accepted to correct my "perfect englisch" and for his engagement in the file management.

Mathias Schulze and Christophe Kottelat for their precious assistance in the computer maintenance.

Dr. Cornel Marxer for his help in the use of Math Lab.

Benedikt Guldimann for his assistance in the use of Lab View.

Dr. Nicolas Blanc, Dr. Philippe Arquint (Phiiiliiippe !), Dr. Jürgen Brugger, Dr. Christian Linder, Dr. Volker Gass, Dr. Ben Kloeck, Marc Boillat, Olivier Guenat, Marco Meijerink, Grégor Schürmann, and Dr. Urs Staufer for interesting comments.

Dr. Louis Guérin and Dr. Hubert Lorenz from EPFL for helpul discussions.

Dr. Paul Muralt from EPFL Lausanne for valuables discussions about the properties of PZT ferroelectric thin films.

Ary Saaman from Debiotech S.A. for interesting discussions.

Our secretaries Antoinette Goumaz-Rebetez and Margrit Rüegg who helped me in the hard way of the administration.

Gianni Mondin and Jean Daniel Cretin from Microsens for their excellent technical contribution.

Christophe Meier and Stefan Gempeler from the High Technical School in Biel-Bienne, which provided excellent contribution in the realization of a phase lock box for feedback controls.

Michel Perdrix from CSEM for having done very nice optical photographies.

Dr. Daniel Gerber, Dr. Gervasio and Dr. Chris Leemann from the Physics Institute, University of Neuchâtel, for many useful discussions.

And finaly my wife, Christine, for her love, her patience, her inspirations, her many judicious advices, for having not danced enough during many years and for her way of enjoying life !

1436

Biography

Philippe Luginbuhl obtained his M.Sc. Degree in physics from the University of Neuchâtel, Switzerland, in October 1992. His master thesis dealt with the development of an apparatus for the measurement of the conductance of high T_c superconducting thin films. In february 1993, he joined the group of Prof. N. F. de Rooij at the Institute of Microtechnology (IMT) of the University of Neuchâtel, as a research assistant. His primary research interests include piezoelectric cantilever beams and ultrasonic Lamb-wave sensors and actuators based on sol-gel deposited *PZT* thin films for micro fluidic delivery systems. In 1996 he collaborated with Micronas S.A. in the field of high frequency SAW filter packaging for mobile phone applications. Since 1997 he has been involved in the realization of a micro DNA liquid injector for mass spectrometry, (μ-DIMS), in collaboration with the Physics Institute of the University of Neuchâtel. Simultaneously with his Ph.D. research activities, he has been involved in the teaching of physics at the High Technical School (ETS) in Biel-Bienne since 1992.